Multi-phase Starter-Generator for 48 V Mild-Hybrid Powertrains

ScuDo
Scuola di Dottorato ~ Doctoral School
WHAT YOU ARE, TAKES YOU FAR

Doctoral Dissertation
Doctoral Program in Electronics Engineering - 29th Cycle

Multi-phase Starter-Generator for 48 V Mild-Hybrid Powertrains

By

Marco Cossale

Supervisor:
Prof. Andrea Cavagnino

Politecnico di Torino
2017

Declaration

I hereby declare that, the contents and organization of this dissertation constitute my own original work and does not compromise in any way the rights of third parties, including those relating to the security of personal data.

Marco Cossale

2017

* This dissertation is presented in partial fulfillment of the requirements for **Ph.D. degree** in the Graduate School of Politecnico di Torino (ScuDo).

Abstract

Transportation electrification has experienced a significant growth in recent years, and the electrification of the powertrain – namely hybridization – is considered the most viable solution seen by car manufacturers to achieve the challenging emission targets. Among the hybrid electrical powertrain topologies, the mild-hybrid configuration with the 48 V battery system offers the best ratio cost versus CO_2 improvements. In particular, the 48 V technology does not require electrical shock protection whilst allows to leverage a variety of fuel saving functions such as electrical boost and regenerative braking.

The thesis is focused on the electromagnetic and thermal design of a Belt-driven Starter Generator, BSG, for 48 V mild-hybrid powertrains. In the BSG layout, the starter-generator replaces the conventional alternator with a low impact on the engine compartment layout, even if a redesign of the belt tensioner is required.

It is noteworthy to keep in mind that the electrical machine shall provide high starting torque and wide constant power speed range, both in motor and generator mode. Furthermore, the application imposes the adoption of low cost materials and the electrical machine is located in a harsh environment. As a consequence, the design is challenging from the electromagnetic, thermal and mechanical point of view.

The novelties of the research lie in the 48 V automotive applications, by describing the practical difficulties to fulfill the design specifications through a suitable material selection, the identification of the cooling system and the available technological solutions.

The first section of the thesis reports results from a literature review on electrical machine for mild-hybrid application aiming to highlight different criteria for the selection of the electrical machine. In this context the advantages in terms of fault tolerance and stator current splitting of multiphase drives are investigated. Furthermore, in this section the required performances and the constraints imposed by the specific application are analyzed.

Among the different motor technologies, a dual three-phase induction machine having two stator winding sets shifted by 60 electrical degrees is selected as a suitable candidate.

The second part of the thesis reports electromagnetic and mechanical issues addressed during the design stage, with special focus on stator winding layout, pole number and rotor slot. The adopted six-phase machine uses a four-layer bar stator winding that has been demonstrated as a good solution to improve the slot fill factor and thermal behavior. In addition, the thesis reports a comparison supported by experimental tests between open and closed rotor slots solutions; the focus is to maximize the machine electromagnetic performance according to the mechanical limits imposed by the rotating speed.

Finally, predicted and measured performance of the prototypes are reported and discussed for validation purposes.

The third part of the thesis deals with the thermal assessment of the BSG with particular emphasis on accurate winding temperature prediction as well as the cooling system selection. Since the stator-winding region is very sensitive to thermal issues and is usually attributed as being the main heat source within the machine body, its thermal modeling is of major importance. In these regards, a simplified stator winding thermal model was developed for the temperature prediction during transient condition. Moreover, considering that the driving cycle is characterized by time variable loss distribution, an effective cooling system must be mandatorily adopted together with high temperature class insulation material. In this context, the development of heat extraction through forced convection is experimentally investigated on the BSG prototype.

As a main outcome of this research activity, it has been demonstrated the feasibility of the proposed design solution with respect to electromagnetic and thermal requirements.

Sommario

Recentemente, l'elettrificazione dei trasporti ha mostrato un notevole progresso, in particolare i costruttori di automobili ritengono che l'elettrificazione del sistema di propulsione, la cosiddetta ibridizzazione, sia la soluzione più praticabile per raggiungere gli ambiziosi obiettivi di emissioni allo scarico. Tra tutte le tipologie di sistemi di propulsione ibrida elettrica, la configurazione *mild-hybrid* con il sistema di accumulo a 48 V offre il miglior rapporto tra costo e riduzione delle emissioni di CO_2. In particolare, la tecnologia a 48 V non richiede costosi sistemi di protezione dell'impianto elettrico e permette di sfruttare una varietà di funzioni volte al risparmio di carburante quali ad esempio l'assistenza elettrica in accelerazione e la frenata rigenerativa.

La tesi è focalizzata sulla progettazione elettromagnetica e termica di un moto-generatore azionato tramite cinghia, BSG, per sistema di propulsione *mild-hybrid* a 48 V. Nella configurazione considerata il moto-generatore è alloggiato in luogo dell'alternatore convenzionale in modo tale da avere un impatto minimale nella disposizione dei componenti nel vano motore. Tuttavia è necessaria la riprogettazione del tendicinghia per far fronte alla maggiore potenza installata.

La macchina elettrica deve fornire un'elevata coppia di spunto e un'ampia gamma di velocità a potenza costante, sia in funzionamento da motore sia da generatore. Tenendo in considerazione che l'applicazione impone l'adozione di materiali a basso costo e che la macchina elettrica si trova in ambiente di lavoro ostile, la sua progettazione è impegnativa dal punto di vista elettromagnetico, termico e meccanico.

L'innovatività della ricerca consiste nell'applicazione automobilistica a 48 V, la descrizione delle difficoltà pratiche per il soddisfacimento delle specifiche di progetto attraverso la selezione di materiali adatti, la definizione del sistema di raffreddamento e le soluzioni tecnologiche disponibili.

La prima parte della tesi tratta le motivazioni per la selezione della macchina elettrica basata sulla ricerca bibliografica dei moto-generatori per applicazioni *mild-hybrid*, l'analisi delle prestazioni richieste e dei vincoli di progetto. Inoltre sono analizzati i vantaggi in termini di tolleranza ai guasti e suddivisione della corrente statorica degli azionamenti multifase.

La macchina a induzione a doppio trifase, le cui terne sono sfasate di 60° elettrici, è stata ritenuta la più idonea tra tutte le tipologie di macchine considerate.

La seconda parte della tesi riporta le problematiche elettromagnetiche e meccaniche affrontate durante la fase di progetto focalizzando l'attenzione sulla configurazione dell'avvolgimento statorico, il numero di coppie polari e le cave di rotore. In particolare, la macchina esafase progettata utilizza un avvolgimento a piattina a quattro strati; tale soluzione permette di aumentare il riempimento della cava e migliorare il comportamento termico. Inoltre, la tesi riporta un confronto, supportato da prove sperimentali, fra le soluzioni di rotore a cava aperta e chiusa; l'obiettivo è di massimizzare le prestazioni elettromagnetiche della macchina in accordo con i limiti meccanici imposti dalla velocità di rotazione.

La terza parte della tesi tratta gli aspetti termici del moto-generatore con particolare attenzione verso la stima della temperatura dell'avvolgimento e la selezione del sistema di raffreddamento. La modellistica termica dell'avvolgimento è di particolare importanza poiché la regione dell'avvolgimento statorico è molto sensibile ai problemi termici e di solito è considerata come la fonte principale di calore nella macchina elettrica. A tal proposito è stato sviluppato un modello termico semplificato dell'avvolgimento per la stima della temperatura durante i sovraccarichi transitori. Inoltre, considerando che il ciclo guida è caratterizzato da una distribuzione delle perdite molto variabile nel tempo, il motogeneratore deve essere equipaggiato con un sistema di raffreddamento efficace e con materiali isolanti adatti alle alte temperature. A questo riguardo, sono state analizzate sperimentalmente le potenzialità di estrazione del calore attraverso tipologie di raffreddamento a convezione forzata.

Table of Content

1. Introduction

1.1. Scope of the thesis

The scope of my PhD project is to design a cost effective electrical machine for 48 V mild hybrid powertrains. In particular, a double three-phase induction machine has been designed and developed. The focus of the thesis is on the design challenges mainly subordinated to electromechanical and thermal issues imposed by the considered hybridization solution.

1.2. Thesis Outline

This thesis is the result of the research activity carried out during my PhD at the Department of Energy of Politecnico di Torino and it is based on a number of scientific publications produced during the course of study. The manuscript is organized in seven main chapters as reported in the following:

Chapter 1

The chapter gives an overview of the thesis with the research motivation, the scope of the thesis, the contribution and the list of publications.

Chapter 2

This chapter introduces the transportation electrification concepts related to the electrification of the powertrain. The review of hybrid electric vehicles topologies is presented with the focus on mild-hybrid configuration.

Chapter 3

The chapter introduces the belt-starter generator project describing the system functionalities, the requirements and challenges. A comprehensive literature review on electrical machine for starter generator application and on multiphase machines configuration are also reported.

Chapter 4

This chapter focuses on the design of the starter-generator. A methodology to design the induction machine is described and the used equations are reported.

The details of the machine are presented with the focus on multilayer bar stator winding, pole count and on rotor slot design.

Chapter 5

This chapter describes the analytical model adopted for the evaluation of the performance and then the comparison of predicted and measured performances of the prototypes are reported and discussed for validation purposes.

Chapter 6

The chapter investigates the thermal issue of electrical machines operating with duty cycle. The focus of this chapter is on the thermal modeling of the stator winding for short-time transients and on the analysis of different forced convection cooling systems.

Chapter 7

The chapter provides a summary of the main results of the manuscript including suggestion and recommendation on further prospective research.

1.3. Scientific Contributions

The scientific contributions resulting from the research activity are summarized in the following:

- A comprehensive literature review of hybrid electric vehicles with the focus on mild-hybrid configuration and electrical machines adopted for belt starter-generators.
- Main differences among the solutions of starter generators presented in this thesis and the benchmark solution available in the literature are mainly from the machine type, the phase configuration and rated voltage. Therefore, the novelties of the research lie in the 48 V automotive applications, by describing the practical difficulties in fulfilling the design specifications through a suitable material selection, the definition of the cooling system, and the available technological solutions.
- A simplified thermal model of the stator-winding region for short-time thermal transient as well as the experimental procedure to assess its thermal parameters have been proposed and developed. The short-time transient thermal model allows determining the maximum over-current value when the transient duration is known or imposed, or vice versa.

- The performed research activities led to the issuance of a number of papers published in international journals or presented at international conferences. Three papers were awarded of internationally recognized prizes, furthermore, my PhD activity was recognized by means of “Premio Qualità 2015” prize of doctoral school of Politecnico di Torino.

1.4. List of Publications

The following IEEE Transaction articles and Conference papers are the results of the research activity during the PhD studies. Part of the scientific dissemination has been conducted in collaboration with universities and research centers, both national and international. In particular, Università di Padova (Italy), Royal Institute of Technology (Sweden), Motor Design Ltd. (UK), Federal University of Santa Caterina (Brazil), University of Bristol (UK). The publications listed below obtained the following awards:
[XIX] IEEE IES Electrical Machine Committee Paper Award, First Prize
[XX] ICEM 2014 Best Poster Presentation Award
[XXI] ICEM 2014 Brian J. Chalmers Best Paper Award

Published Journal papers

[I] A. Krings, **M. Cossale**, A. Tenconi, J. Soulard, A. Cavagnino, A. Boglietti, "Characteristics Comparison and Selection Guide for Selected Magnetic Materials used in Electrical Machines", IEEE Trans. on Ind. Appl. Magazine, to appear Nov/Dec 2017.

[II] R. Bojoi, A. Cavagnino, **M. Cossale**, A. Tenconi, "Multiphase starter generator for 48V Mini-hybrid Powertrain: Design and Testing", IEEE Trans. on Ind. Appl., Vol.52, No. 2, pp1750-1758, 2016.

[III] A. Boglietti, E. Carpaneto, **M. Cossale,** S. Vaschetto , "Stator Thermal Models for Short-Time Thermal Transients", IEEE Trans. on Ind. Elect. Vol. 63. No.5, pp. 2713-2721, 2016.

[IV] A. Boglietti, E. Carpaneto, **M. Cossale**, S. Vaschetto, M. Popescu, D. A. Staton, "Stator winding Conductivity Evaluation: An Industrial Production Assessment", IEEE Trans. on Ind. Appl. Vol. 52. No.5, pp. 3893-3900, 2016

[V] **M. Cossale**, A. Krings, J. Soulard, A. Boglietti, A. Cavagnino, "Practical Investigations on Cobalt-Iron Laminations for Electrical Machines", IEEE Tran. on Ind. Appl., vol. 51, n. 4, pp. 2933-2939, 2015.

Published conference papers:

[VI] A. Boglietti, **M. Cossale**, S. Vaschetto, T. Dutra, "Thermal Parameter Evaluation for Stator Fractional Slot Concentrated Winding Machine", IEEE International Symposium on Industrial Electronics, Santa Clara, USA pp. 228-233, 2016.

[VII] F. Tinazzi, M. Zigliotto, A. Boglietti, A. Cavagnino, **M. Cossale**, "Energy Efficiency Assessment for Inverter-fed Induction Motors", IET International Conference on Power Electronics, Machines and Drives PEMD'16, Glasgow, UK, pp. 1-6, 2016.

[VIII] A. Cavagnino, **M. Cossale**, A. Tenconi, S. Vaschetto, "Prototyping Experience on 48V Starter Alternators", International conference on Electrical Machine ICEM'16, Lausanne, CH, pp. 2009-2014, 2016.

[IX] A. Boglietti, **M. Cossale**, S. Vaschetto, T. Dutra, "Thermal Parameters Evaluation of Fractional-Slot Concentrated Winding Machine for Home Appliance Application", International conference on Electrical Machine ICEM'16, Lausanne, CH, pp. 2106-2111, 2016.

[X] A. Boglietti, **M. Cossale**, S. Vaschetto, T. Dutra, "Experimental Validation in Operative Conditions of Winding Thermal Model for Short-Time Transient", IEEE Energy Conversion Congress and Exposition, Milwaukee, USA 2016.

[XI] A. Boglietti, **M. Cossale**, S. Vaschetto, T. Dutra, "Thermal Conductivity Evaluation of Fractional-Slot Concentrated Winding Machines", IEEE Energy Conversion Congress and Exposition, Milwaukee, USA, 2016.

[XII] A. Krings, **M Cossale**, A. Tenconi, J. Soulard, A. Cavagnino, A. Boglietti," Characteristics Comparison and Selection Guide for Magnetic Materials used in Electrical Machines", IEMDC, Coeur d'Alene, USA, 2015.

[XIII] A. Boglietti, E. Carpaneto, **M. Cossale**, M. Popescu, D. Staton, S. Vaschetto," Equivalent Thermal Conductivity Determination of Winding Insulation System by Fast Experimental Approach", IEMDC, Coeur d'Alene, USA, 2015.

[XIV] A. Boglietti, E. Carpaneto, **M. Cossale**, M. Popescu, D. Staton, S. Vaschetto" Stator Winding Thermal Conductivity Evaluation: an Industrial Production Assessment", ECCE, Montreal, Canada, 2015.

[XV] E. Armando, A. Boglietti, E. Carpaneto, **M. Cossale**, S. Vaschetto "Winding Thermal Model for Short-Time Thermal Transient: Validation in Motor Operative Conditions", IEEE IECON, Yokohama, Japan, 2015.

[XVI] A. Boglietti, R. Bojoi, A. Cavagnino, **M. Cossale**, A. Tenconi "Analysis of Different Forced Convection Cooling Systems for Belt-Driven Starter-Generator", IEEE IECON, Yokohama, Japan, 2015.

[XVII] R. Bojoi, A. Cavagnino, **M. Cossale**, A. Tenconi, S. Vaschetto, «Design Trade-off and Experimental Validation of Multiphase Starter Generators for 48V Mini-Hybrid Powertrain", IEVC, Florence, Italy, 2014.

[XVIII] R. Bojoi, A. Cavagnino, **M. Cossale**, S. Vaschetto, "Methodology for the IPM Motor Magnetic Model Computation based on Finite Element Analysis", IEEE IECON, Dallas, USA, 2014.

[XIX] A. Boglietti, E. Carpaneto, **M. Cossale,** A. Lucco Borlera, D. Staton, M. Popescu," Electrical Machine First Order Short-Time Thermal Transients Model: Measurements and Parameters Evaluation", IEEE IECON, Dallas, USA, November 2014.

[XX] A. Boglietti, E. Carpaneto, **M. Cossale**, A. Lucco Borlera, "Stator Thermal Model for Short-Time Thermal Transients", ICEM, Berlin, Germany, September 2014.

[XXI] **M. Cossale**, A. Krings, J. Soulard, A. Boglietti, A. Cavagnino, "Practical Investigations on Cobalt-Iron Laminations for Electrical Machines", ICEM, Berlin, Germany, 2014.

[XXII] A. Krings, **M Cossale**, J Soulard, A. Boglietti, A. Cavagnino, "Manufacturing Influence on the Magnetic Properties and Iron Losses in Cobalt-Iron Stator Cores for Electrical Machines", ECCE, Pittsburg, USA, 2014.

[XXIII] R.Bojoi, A. Cavagnino, **M. Cossale**, A. Tenconi, "Multiphase starter generator for 48V Mini-hybrid Powertrain: Design and Testing", SPEEDAM, Ischia, Italy, 2014.

1.5. Background–Emission requirements and regulation

The United Nations Framework Convention on Climate Change, requires all parties to formulate and implement national and regional programs containing measures to mitigate climate change. In this regard, European Parliament and the Council adopted the goal of a reduction of greenhouse gas emissions of 30% (compared to 1990 levels) by industrialized countries by 2020. In addition, the European Union, EU, itself will take the firm independent commitment to reduce greenhouse gas emissions by at least 20% greenhouse by 2020 (compared to 1990 levels), irrespective of reductions achieved the other industrialized countries [1]. It is noteworthy to keep in mind that, the primary greenhouses gases in earth atmosphere are water vapor (H_2O), carbon dioxide (CO_2), nitrous oxide (N_2O), methane (CH_4) and sulfur hexafluoride (SF_6).

Considering that road transport is the second largest sector source of greenhouse gas emissions in the EU and its emissions continue to rise, one of the implications of the required measures is, for all Member States, to reduce significantly emissions from passenger cars. In this regard, the regulation [1] establishes performance standards for new passenger cars CO_2 emissions. In particular, it sets the average CO_2 emissions from new passenger cars at 130 g CO_2 / km, measured in accordance with New European Driving Cycle, NEDC, to be achieved through technological improvements to vehicle engines [2]. From 2021 onwards, the regulation sets a target of 95 g CO_2/km as average emissions for the new car fleet. In addition to EU, the worldwide trend of CO_2 emission equivalent for NEDC test in g CO_2/km is reported in Fig. 1.3.1.

In this context, carmakers have concentrated a huge amount of investments in order to meet these regulations taking also into account the penalty to exceed the CO_2 emission limit (for which the additional cost in 2021 in EU will be about 95 € per vehicle for each grams of CO_2 above the 95 grams' limit)

Focusing on the internal combustion engine, the ideal combustion process of a hydrocarbon fuel C_xH_y (as gasoline or diesel) should lead to non-toxic combustion products (CO_2, H_2O, N_2 plus O_2 for lean mixtures) [3]. On the contrary, the real combustion reaction produces pollutant emissions (about 1% of all combustion products), mainly represented by CO, unburned hydrocarbons (HC), nitrogen oxides (NO_x) and particulate matter (PM). In order to keep the pollutant emission within the limits prescribed by international regulations, operations before the combustion process as well as the after treatment of the exhaust gases are necessary.

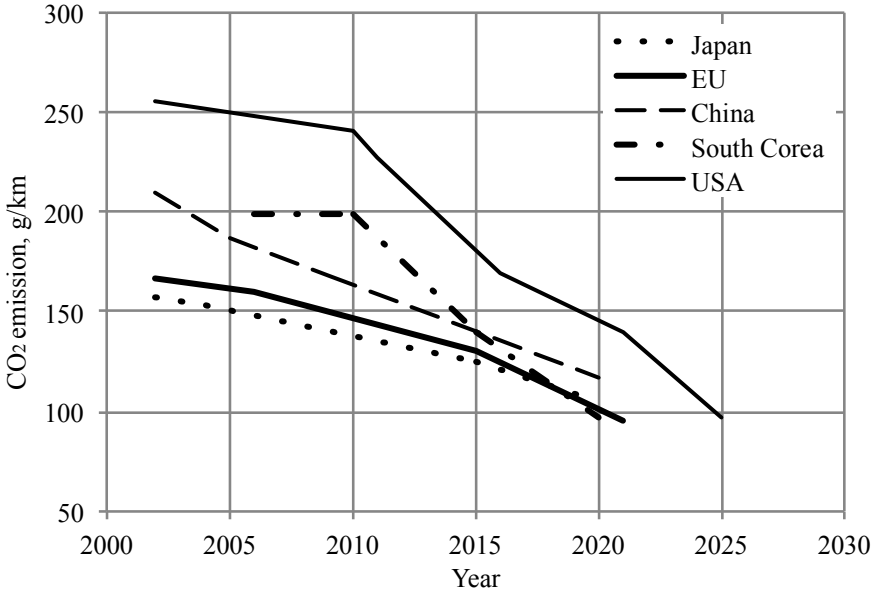

Fig. 1.3.1. Worldwide CO_2 target emission normalized to NEDC.

For example, three way catalysts are used in gasoline engine to promote the CO and HC oxidation and NOx reduction in the exhaust gas stream. For diesel engines, more complex after-treatment systems such as specific NOx catalyst and PM filters are necessary. Both NOx and PM traps need however to be periodically "regenerated" by eliminating the NOx and PM captured during the system operation.

For what it concerns the greenhouse gas CO_2, considering that it is the result of an ideal combustion process, the only way to reduce its quantity is to reduce the amount of burned fuel, hence improving the powertrain efficiency [3].

Neglecting the possible benefits coming from reduction in rolling resistance due to "green" tires, aerodynamics improvements and vehicle body lightening, the research community agree that the challenging CO_2 target emission seems to be achieved only through the hybridization of the powertrain, hence combining the internal combustion engine with one or more electrical machines.

2. Transportation electrification

The electrification of road transport started in the early years of the 1900s where the electrical systems were limited to ignition, headlight and cranking of the engine. As timeline of the principal milestones of electrification should be highlighted that in the 1950s the car radio was introduced, in the 1960s the electronic fuel injection was adopted and in the 1970s the first on board controllers and computers appeared [4]. Subsequently were introduced Antilock Braking Systems, ABS, airbags and gradually several mechanical-hydraulic systems have been replaced by electrical ones. These progresses highlight the main reasons behind electrification and in particular the starter motors were adopted for convenience, radios for entertainment, ABS and airbags for safety, fuel injectors and controllers for improving the engine performance, efficiency and lower emissions. Regarding the powertrain electrification, throttle control, valvetrain actuation and water and oil pumps have been electrified with the aim to increase reliability and efficiency while reducing the costs. The adoption of electrical drive in supercharger and turbo systems allow both, to improve the driving performance and to recover the exhaust energy.

The powertrain electrification is also called hybridization when the electrical drive is integrated with the powertrain in order to contribute at the propulsion of the vehicle. The two propulsion systems are suitable to co-exist as they have complementary characteristics. In particular, the electrical machines operate from the standstill and it can work in traction and in generation allowing obtaining the following efficiency improvements:

- To restore energy during deceleration using regenerative braking instead of dissipating it as heat in a conventional braking system
- To eliminate or to mitigate the idling losses by turning the engine on and off, following the so called Start&Stop strategy
- Operating the internal combustion engine nearer its best efficiency, trying to avoid its use under highly inefficient operating conditions such as low loads, thanks to the additional degree of freedom provided by the electrical power source and energy storage devices (load point shift);
- Enabling downsizing of the internal combustion engine while still maintaining acceptable vehicle performance thanks to the additional boosting which can be provided by the electric power source during take-off and tip-in maneuvers

2.1. Hybrid electric vehicles

The hybrid electrical vehicles can be categorized according to their configuration or to degree of hybridization [5]. Traditionally there are two basic categories of hybrid electric vehicles, HEV: series hybrid and parallel hybrid [6]. Recently, in order to improve the power performance and fuel economy, series-parallel HEVs have been developed [7]. Considering the degree of hybridization, the possible solutions are micro-hybrid, mild-hybrid and full hybrid electrical vehicles. Each of them has its own pro and cons, and the choice of a particular configuration/degree of hybridization depends on many aspects, including the mission assigned to the vehicle. Fig. 2.1.1 shows the simplified classification of the HEVs in relation to the electric storage system and drive train power source.

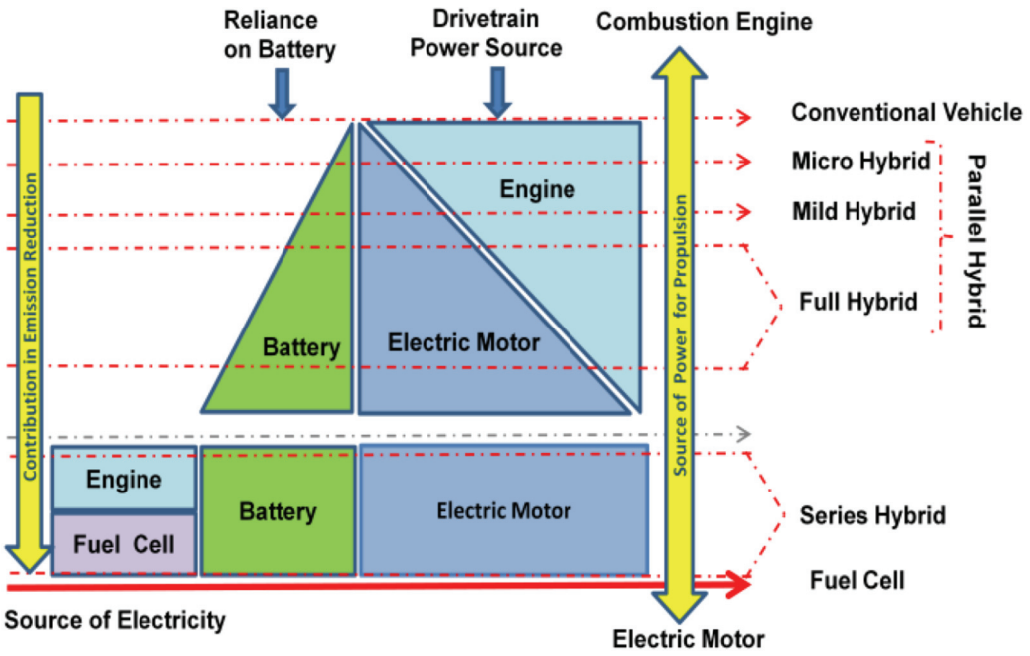

Fig. 2.1.1. Simplified classification of the HEV in relation to the electric storage system [8].

2.1.1. Series HEV

In series-HEV, the ICE drives an electrical machine, EM, which produces power for charging the batteries. The converted electricity feeds the electric drive that delivers the propulsion power to the wheels. In this architecture, represented in Fig. 2.1.2, the ICE and the driving wheels are mechanically decoupled with the advantage of flexibility for locating the ICE generator set.

Since the drivetrain needs three devices, the ICE, the generator and the electric motor, the overall efficiency of series HEV is generally low. A variant of this configuration, namely range extender, is also used to increase the autonomy of electric vehicle recharging the battery while driving.

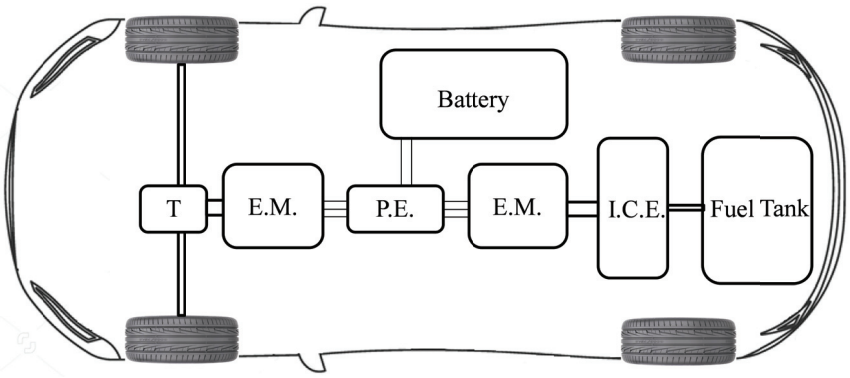

Fig. 2.1.2. Representation of series HEV driveline.

2.1.2. Parallel HEV

In parallel-HEV configuration, both the ICE and the electric machine are coupled via clutches to drive the wheels. In such a way, the propulsion power may be supplied to the driving wheels by ICE alone, by electric machine, or by both. The electrical machine can be used as generator to charge the batteries by absorbing power from the ICE or by regenerative braking. Since the electrical machine can be used for both motoring and generating mode, this architecture, represented in Fig. 2.1.3, requires only two propulsion devices. This system is highly scalable: from modest electric drives power to drives capable of plug-in hybrid operation.

2.1.3. Series–Parallel HEV

The series-parallel HEV configuration encloses the features of both, parallel and series architecture as shown in Fig. 2.1.4. The architecture is composed of one ICE and two electrical machines, which are used to provide both parallel and series path for the power. Despite the configuration has the advantages of both series and parallel, it is relatively more complicated and costly. Nevertheless, some HEV adopt this system. It is the most sophisticated of all the currently available hybrid systems and excels in optimizing engine efficiency during city driving. The downside is the cost associated with the requirement for two large electric motors and their associated power electronics.

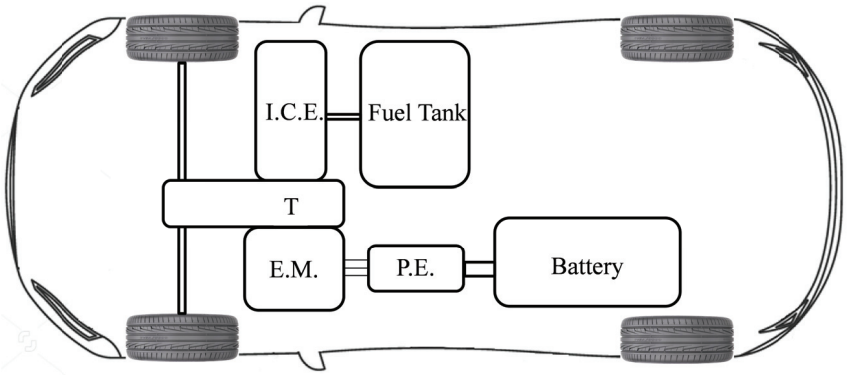

Fig. 2.1.3. Representation of parallel HEV driveline.

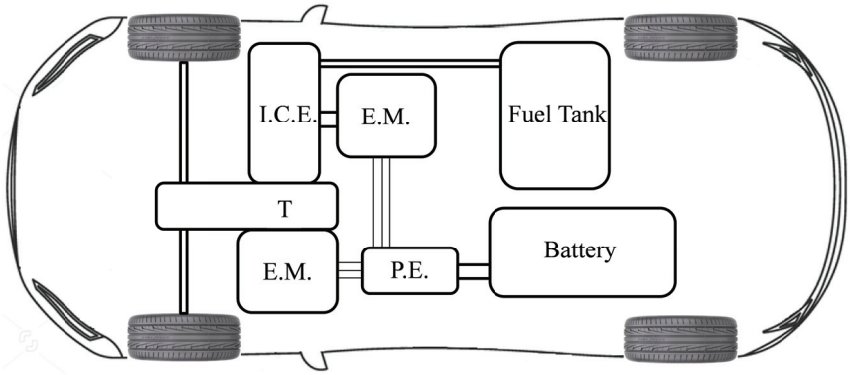

Fig. 2.1.4. Representation of series-parallel HEV driveline.

2.2. Hybridization level

2.2.1. Micro–hybrid

Micro-hybrid has a hybridization factor of 5-10%, in this configuration the starter and alternator are integrated in one device, with a typical power of approximately 3 kW. Typically, the system is adopted with 12 V or 24 V lead acid batteries assisted by small ultra-capacitors or Li-ion batteries. The main functionalities are start and stop of the engine with fast response and less vibration, on board energy generation and a limited amount of regenerative braking. This strategy allows obtaining efficiency improvement in city driving

mitigating the idling losses by turning the engine on and off. The cost of the system is only few percent higher than that of conventional vehicle while, in city driving with frequent starts and stops, the fuel consumption may be reduced by approximately 5-10%. The first production micro-hybrid system is Mazda's i-ELOOP, which was introduced in 2014 on the Mazda3 and Mazda6 [9].

2.2.2. Mild–hybrid

Mild-hybrid has a hybridization factor of 10-25% and the electrical machine power is typically around 10-25 kW. Since mini-hybrid systems already push the 12 V technology to its limits, higher voltage architectures are adopted in mild-hybrid (48-200 V). In addition to the functionalities of mini-hybrid, this configuration provides torque assistance, improved regenerative braking and sailing. In urban driving cycle the fuel consumption can be reduced up to 20%, but the cost will also increase 20-30%. As an example, a current production vehicle equipped with a mild-hybrid system (115 V battery) is the Buick LaCrosse eAssist [10]. This parallel hybrid solution represents nowadays an interesting tradeoff in terms of complexity, cost, performance enhancement and fuel consumption reduction.

2.2.3. Full–hybrid

Full-hybrid typically has energy storage system from 200 to 600 V in order to manage power about 50-100 kW. The most common configuration adopts series-parallel architecture with an engine, a generator and a motor. The propulsion can be executed by the engine only, by electrical motor only or by a combination of both with the aim to achieve optimum drive performance at maximum energy efficiency and minimum emission. The fuel saving in city driving cycle is about 20-30% while the cost can increase about 30-40%. The full hybrid can be further subdivided into Synergy-hybrid and Power-hybrid. The former compromises the drive performance, fuel consumption and emission reduction. The latter favor the driving performance; thus the electrical motor supports the engine that is not downsized.

2.3. Focus on mild–hybrid configurations

The mild-hybrid configuration, as previously mentioned, represents nowadays an interesting compromise with respect to other hybrid solutions for its easy

implementation on conventional vehicles, limited cost and weight and good fuel economy improvement.

In this configuration, a single electrical machine instead of two separated devices (starter and alternator) is used to fulfill the engine start up and on-board generation of electric energy. The electrical machine that performs these functions is called integrated starter generator (ISG). The preliminary concept of ISG dates back to 1930s [11] but its implementation was complicated by the lack of suitable power electronics and control techniques. With the recent improvement in power devices, battery technology and motor control, this system became feasible to be implemented in the drivetrain.

The possible architectures that can be implemented for a ISG mild hybrid drive train are depending on the location of the electric machine in the powertrain and its connection to the crankshaft as showed in Fig. 2.3.1. There are four packaging options with three different drives: belt drive or chain drive, P0, direct coupled drive, P1 and gear drive, P2 and P3 [11].

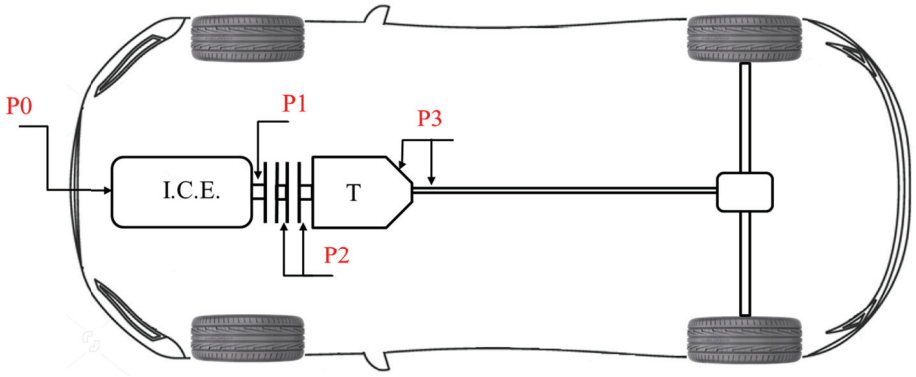

Fig. 2.3.1. Hybrid-electrical drive configurations

2.3.1. Direct coupled drive

In direct drive solution, the electric machine is inserted between the engine and the gearbox in the location of the flywheel, (position P1 in Fig. 2.3.1). The available volume allows the accommodation of large diameter machine; hence larger torque and larger hybridization factor can be achieved; typically, the on-board electric power can be scaled up to hundred kW. This system can provide good torque smoothing capabilities and including the motor on the crankshaft may also enable the replacement of the flywheel by the machine rotor.

However, the solution requires an increased powertrain axial length to accommodate the starter-generator, which can be a critical issue in vehicles with transverse engine arrangement. [12], [13]. An example of direct-coupled drive available on the market is shown in Fig. 2.3.2.

Fig. 2.3.2. Porsche Panamera E-Hybrid [34]

Fig. 2.3.3. Electrical machine and converter integrated in the gearbox [14]

2.3.2. Gear drive

In gear drive solution the electrical machine is coupled on the transmission side requiring a modification of the transmission housing. The electrical machine can be located on the gear input, position P2 in Fig. 2.3.1, or on the gear output, position P3 in Fig. 2.3.1. Depending on the design this configuration can also be scaled up in output power level to provide a good hybridization level. The major issue related to this coupling is that at high speeds and low loads the gear teeth risk to be damaged. In Fig. 2.3.3 an example of a multiphase drive integrated in a gearbox is presented.

2.3.3. Chain drive

This coupling involves the use of a chain to run over the pulleys. The most suitable position for the electrical machine is in the transmission case, in the location of the conventional starter, position P1 in Fig. 2.3.1. The major advantage of using a chain drive is given by a higher material tensile strength of chain with respect to the belt that leads to smaller encumbrance of package for the same fatigue life [15]. The disadvantages are related to the limited space in the transmission case, for the accommodation of the electrical machine and intrinsic noise issues.

2.3.4. Belt drive

In belt-driven starter generator solution, also referred to BSG, the electrical machine replaces the conventional alternator and the connection to the crankshaft is realized on the accessory side using a revised belt drive, position P0 in Fig. 2.3.1. The modification of the belt drive is necessary in order to fulfill the increased load capacity introduced by the starter-generator. In this configuration the impact on the engine compartment layout is low and requires minimal modification in existing powertrain design. In addition, this configuration has the advantages of more flexibility in packaging, no lubrication required and very low noise. The main drawback is the limitation of the torque transmission through the belt drive. However, it is possible to manage mechanical power in the order of 10-15 kW, [16]-[18]. Fig. 2.3.4 shows the BSG solution adopted for a commercial powertrain.

Fig. 2.3.4. GM Belt-Alternator Starter mild-hybrid drivetrain [19].

2.4. 48 V system

The progressive replacement of the belt driven load (such as power steering pump, oil and water pumps, suspension control or braking, etc.) into electric high power devices increases the electrical energy consumption in vehicles. All those high power loads combined with Start&Stop, pushed the 14 V system to its limits. Additional comfort functionalities such as electric-driven air conditioning or autonomous driving features as well as fuel saving functionalities like energy recovery for deceleration or boost for acceleration require a higher voltage supply system. For these reasons, some German premier carmakers propose to increase the system voltage level from 14 V to 48 V.

The concept of a higher voltage for electric and electronic systems in the vehicles was introduced in the beginning of this millennium with regard to 42 V systems with the aim to increase the comfort functions [20], [21]. Despite the potential benefits, the 42 V system did not penetrate into the market since the high cost of components and the lack of a real need.

Nowadays, the technology has significantly improved, the components are cheaper and the driving force is to provide an inexpensive alternative to hybrid vehicles, which allows a significant reduction of CO_2.

The 48 V system is a compromise concerning safety and functionality in fact electrical shock protection is not required for *dc* voltage lower than 60 V and in addition, 48 V is considered as the minimum voltage level for efficient energy recuperation in Li-ion battery technology. However, a critical effect that requires additional system protection measures is arching. In fact, due to the high temperature of the plasma, the surrounding materials might be set to fire. The degree of damage is linked to the arc energy. The voltage levels for 48 V systems, Fig. 2.4.1 are specified in LV 148 which is the only official document issued by German OEMs [22]. The operating range is between 36 V and 52 V while there are functional restrictions between under voltage and upper voltage areas. The under voltage range is set between 20 V and 24 V while the over voltage range is between 54 V and 60 V; 60 V must not be reached.

A typical 48 V system configuration, Fig. 2.4.2, consists of 48 V Li-ion battery which provide on one side energy to the 14 V load via a *dc/dc* converter and on the other side energy to the high power function mentioned above. In some application, the battery can be supported by super capacitors.

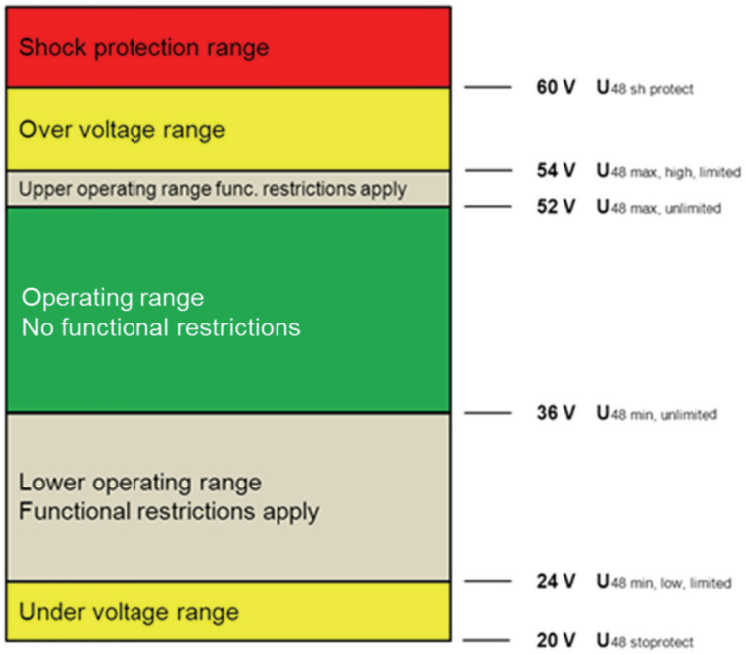

Fig. 2.4.1. Voltage level for 48 V system [22]

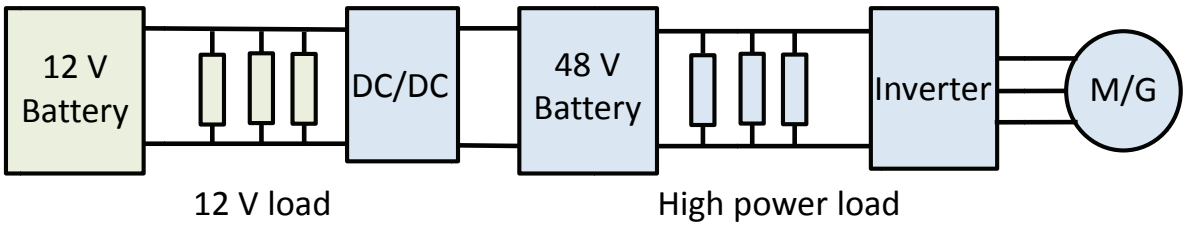

Fig. 2.4.2. 48V system configuration

2.5. Conclusion

The hybridization of the internal combustion engine is considered the most viable solution to meet the objective of reducing pollutant gases emission. The trend concerning hybrid-electric vehicles is going in two directions: one direction is the full-hybrid aiming for high-energy efficiency and low emission. This approach implies non-negligible additional costs and complexity compared to conventional powertrains. Another direction is represented by micro-hybrid and mild-hybrid systems that are characterized by simple structure, effective fuel saving and low cost. In this context, the 48 V systems offer best ratio cost versus CO_2 improvements and it is considered as effective transitory solution.

3. Belt starter–generator project

3.1. System functionalities

This section presents a structured description of the main functionalities of a belt starter-generator system. In particular, the most important functions performed by a BSG are:

- Engine Start&Stop
- Electric power assist-torque boost
- Regenerative braking

The secondary functions can be summarized in:

- Engine torque smoothing;
- Opportunity battery charging and discharging;

The most important contribution to fuel saving is represented by Start&Stop functionality and regenerative braking. Electric assist helps to reduce the fuel consumption but its effect is usually lower compared to the other functions.

Engine start/stop

One of the fuel saving functions of BSG is Start&Stop; this strategy consists in switching off the ICE when it is not used to propel the vehicle and crank the engine when the driver wants to move the vehicle. For the comfort of the passengers these operations must be performed quietly and quickly. However, there are many conditions that have to be checked by the management system before to enable this strategy such as the state-of-charge of the battery or the temperature of the exhaust after-treatment. The electrical machine in starter mode has to crank the ICE to the minimum engine speed for start the ignition (60-100 rpm for gasoline and 80-200 rpm for diesel engine). Higher speed during start-up would help to reduce noxious emission significantly. Typically, the starting time is in the range of 250-400 ms depending on the application.

Electric power assist – torque boost

The electric power assist is a fuel saving function that can be performed with BSG solution. In this strategy the starter-generator provides torque in order to aid

the ICE to improve the throttle response during vehicle starts and acceleration request. The slow dynamic of the engine can be partially mitigated by the quick transient of the electrical machine improving the vehicle drivability and acceleration performance. In addition, during sudden pedal request by the driver, it can happen that in the available gear the engine is not capable of meeting the desired torque, so a downshift is necessary. The electric power assist function of the BSG can compensate the transient extra torque request avoiding the downshift. The amount and duration of electric assist depends on the motor power rating as well as on the battery capability of providing energy to the drive (maximum discharge power and state of charge).

In Fig. 3.1.1 the desired motoring torque characteristics is shown. The cranking torque to overcome the engine static friction defines the value of the peak motoring torque. The torque value and speed range for performing the electric power assist, usually determined from the customer requirements, defines the constant power region.

In this regard, the pulley ratio is an important design parameter because torque and speed ranges depend on it. The reduction ratio is usually chosen in order to avoid that the machine runs at speeds above the maximum speed limits. Typical reduction ratios, for a gasoline engine with 6000 rpm maximum speed, are in the range of 1:2.3-1:3.2 depending on the maximum allowed speed of the electrical machine. A lower reduction ratio means lower torque available at the crankshaft, therefore the ratio must be chosen considering maximum torque and speed specifications.

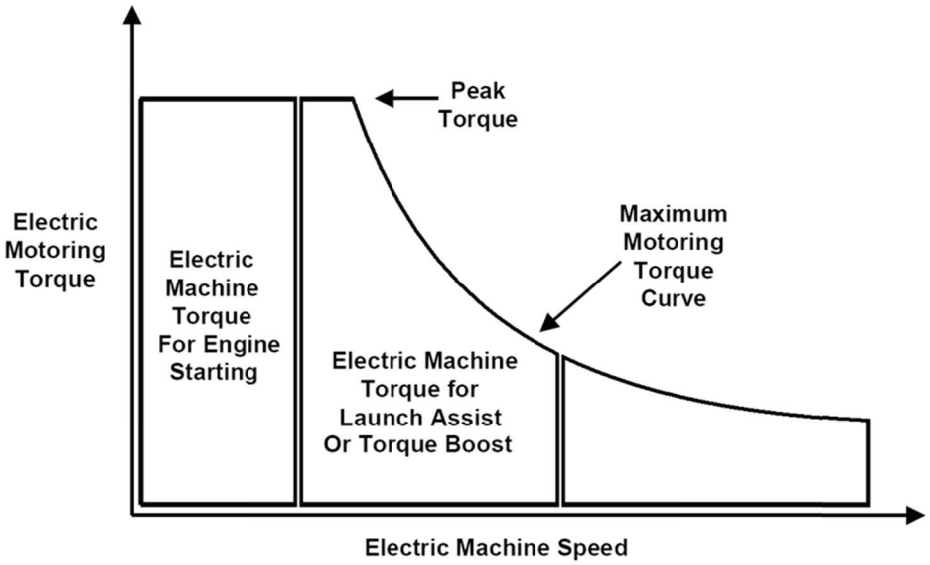

Fig. 3.1.1. Motoring torque requirements [23].

Regenerative braking

The regenerative braking is an important function of BSG system that allows to decelerate the vehicle recovering portion of the kinetic energy (which otherwise would be dissipated as heat in the friction brakes) into electrical energy to recharge the battery. The stored energy is then used to carry out all the functions that require electric energy, including electric power assist or to feed the electric loads during idle stop.

In order to improve the kinetic energy recovery, the regenerative braking control acts on the engine to reduce the losses in the powertrain and on the brake system to prevent the friction brake.

For low deceleration requests, the brake power is completely realized by the BSG until the limit of regenerative braking is reached. This logic, however, requires that the traditional brake systems have to be replaced by a dedicated electrical actuator with increased costs and safety issues.

The electrical machine operates in generating mode from idle speed up to the top speed of the engine. However, three principal areas are more common, as illustrated in Fig. 3.1.2.

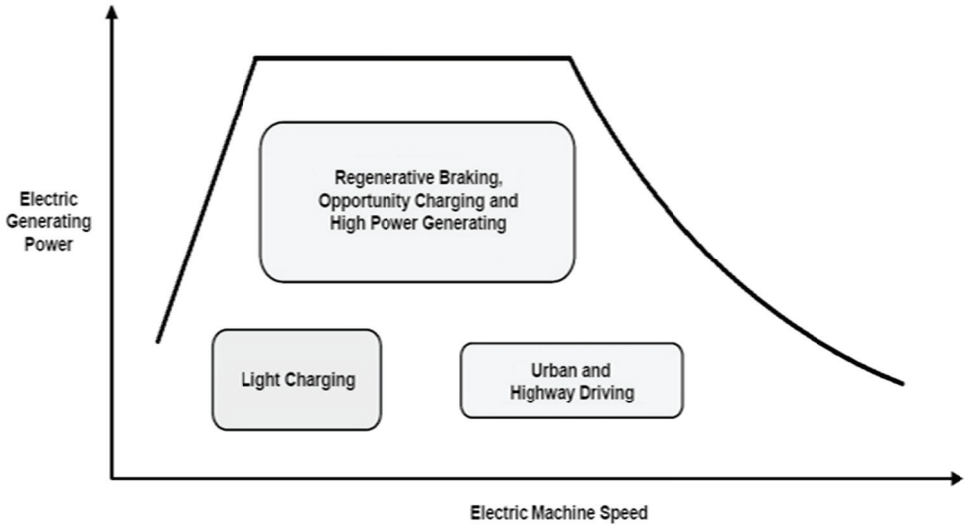

Fig. 3.1.2. Generating power requirements.

Fig. 3.1.2 highlights the speed and power ranges of the main operating mode. The areas at very low and very high speed are usually not extensively used because of technical limits. The maximum power in generating mode is required during regenerative braking in a wide speed range.

Secondary functions

Secondary functions can be implemented in the BSG system in order to improve fuel consumption comfort and drivability.

The motor-generator can be used to smooth the torque irregularities originated by the engine compression pulse especially during cranking. This strategy improves the comfort feeling of the passengers during Start&Stop.

Opportunity battery charging and discharging refers to the practice of using the BSG in particular situations to produce electric energy or consume it in order to modify the battery SOC and keep it within the safety limits. As an example, if the SOC is low, the engine is extra fueled to drive the electric machine and charge the battery. Similarly, if SOC is high, the control system selects the engine operating condition so that part of the requested power is provided by the motor which discharge the battery.

3.2. Requirement and challenges

In the BSG layout, sketched in Fig. 3.2.1, the electrical machine is mechanically coupled to the engine and auxiliaries through a poly V-belt whose transmission ratio is fixed to 1:2.7. This configuration requires a modification of the conventional belt drive system in order to cope with the increased load capacity. It can be remarked that the conventional alternator uses the force of the belt to transfer the power in only one direction; conversely BSG has bidirectional forces on the belt to speed up the ICE during cranking and boosting. Therefore, in order to avoid slip between belt and pulley, as well as minimize the belt losses during operation, is necessary to regulate the strain of the belt through an active tensioner.

The engine compartment, where the electrical machine is located, is characterized by severe ambient condition; in particular, the temperature can range from -40°C up to 125°C, while the engine coolant average temperature is in the range of 90-100°C. In addition, the electrical machine is exposed to dust and highly corrosive substances such as oil and grease.

System requirements

The maximum performances for the BSG are reported in Fig. 3.2.2, both for the motoring and generating modes. In the same figure, the typical speed-torque operating points during a real urban driving cycle are reported too. This cycle has been provided by the carmaker involved in this research activity

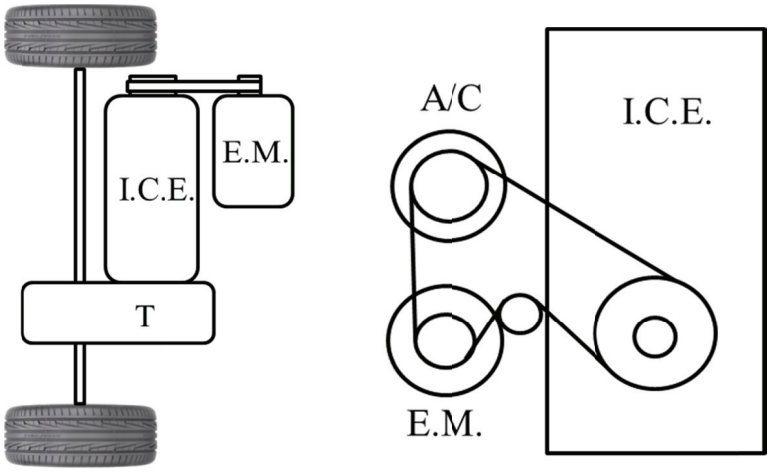

Fig. 3.2.1. System configuration for BSG solution (T-Transmission, ICE-Internal combustion engine, EM-Electrical machine, A/C-Air conditioning)

As an example of the urban driving cycle as function of the time, a portion of the torque and speed profiles are shown in Fig. 3.2.3 and in Fig. 3.2.4, respectively. With respect to the motoring mode (see Fig. 3.2.2), the electrical machine is required to develop a cold engine cranking torque of 44 Nm for a duration time up to 1 s.

During urban driving cycle, where the engine is warmed up, the required cranking torque is reduced down to 30 Nm (Fig. 3.2.3). A maximum motoring power of 9 kW for launch-assistance is available for speed up to 9000 rpm. During the typical urban driving cycle, the electrical machine is operated as generator from 2000 rpm up to 9000 rpm, providing energy to the electrical loads and performing the energy recovery during braking.

In the generating mode the peak power is 10 kW (at the shaft) from 2000 up to 18000 rpm. On the basis of the typical urban driving cycle and the maximum performance of the starter-generator, the carmaker specifies a reference duty cycle of 5 seconds ON and 30 seconds OFF for the electromagnetic and thermal design of the BSG prototype

Additional application constraints related to the overall dimensions and materials must be considered too. The maximum allowable volume for the active parts, including the room for the housing, is a cylinder having an outer diameter of approximately 150 mm and an axial length of 170 mm. In addition, the power electronics is integrated in the motor housing, and the cooling system is shared between them.

TABLE I.
TARGET SPECIFICATION AND CONSTRAINTS

Target weight	8	kg
Target rotor inertia	48	$kgcm^2$
Peak torque at low speed (<1800 rpm)	44	Nm
Peak generation torque	30	Nm
Maximum mechanical power (Motor)	9	kW
Maximum mechanical power (Generator)	10	kW
Mechanical over-speed	20000	rpm
Typical ambient temperature	105	°C
dc voltage ISO 6469 Class A, 48 V		

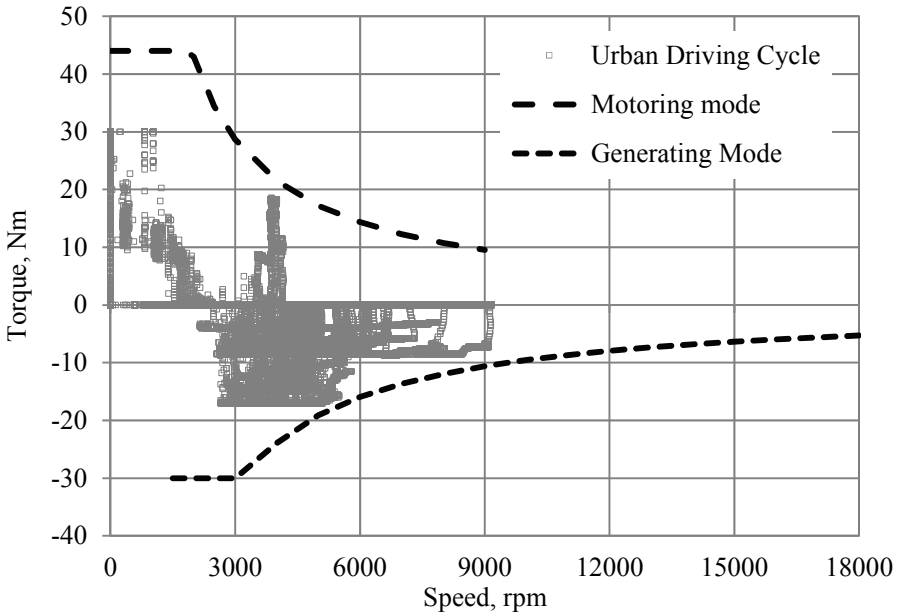

Fig. 3.2.2. Torque target characteristics.

Moving from the system requirements and target specifications, summarized in Table I, it can be deduced the main challenges in the electrical machine design:

- High power and torque density
- 10 kW peak power at low voltage (high current)
- Constant Power Speed Range (CPSR) equal to 6
- Temperature of the engine compartment around 105 °C
- Thermomechanical integration of the power electronics
- Low cost materials

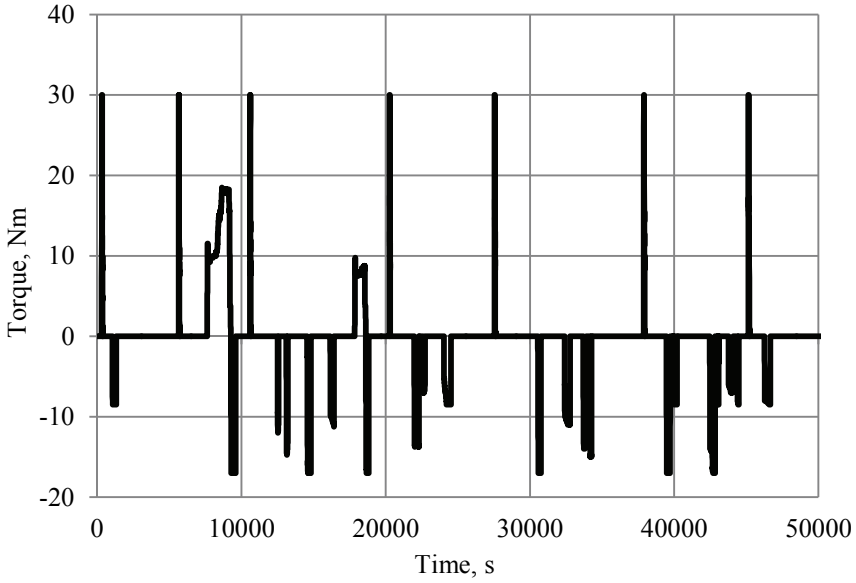

Fig. 3.2.3. Torque profile during urban driving cycle.

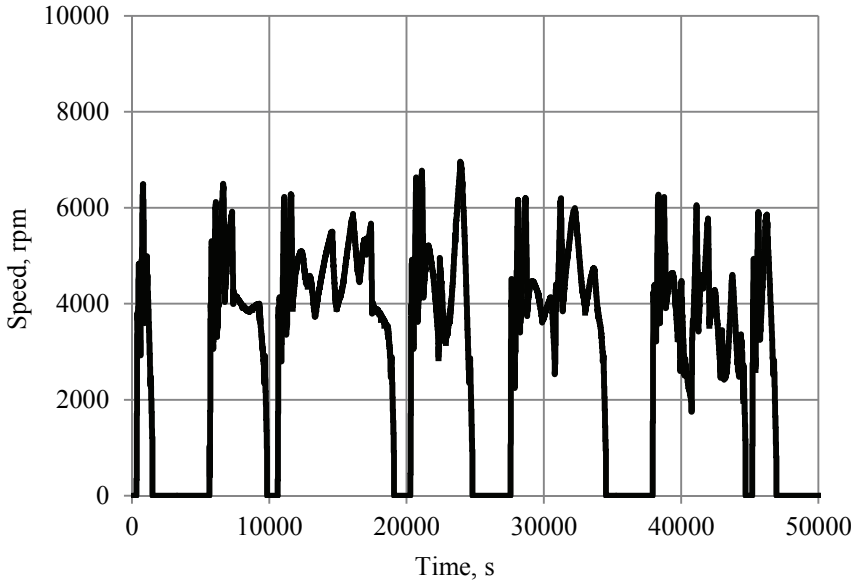

Fig. 3.2.4. Speed profile during urban driving cycle.

3.3. Electrical machine topology for starter generator application

The most commonly addressed machines for belt-driven starter-generator applications that can be found in literature are synchronous as well as asynchronous ac machines. In particular, the investigated topologies are the wound rotor synchronous machines, WRS, the interior permanent magnet synchronous machines, IPM, and the induction machines, IM [11] [24]. Hereafters are presented and discussed in detail their main features.

3.3.1. Synchronous machines

Wound rotor synchronous machines

Among the synchronous machines, WRS machines in claw-pole (or Lundell) configuration are widely used as alternator in vehicles because of its low cost production.

The stator configuration is the same as the other ac machines while the rotor consists of a field coil encapsulated between claw pole segments. The rotor coil terminals are connected to the external circuit by means of slip ring and brushes. In this way, the rotor magnetic field is regulated by the excitation current allowing simple field weakening operation and a wide constant power speed range. The main drawback of this machine topology concerns the difficulty to scale it up due to the high rotor leakage flux between claw poles with increased axial lamination length [11]. In this regards, in order to improve the torque density necessary for cranking the engine, the manufacturers have proposed different solutions, such as dual-field coils [11], magnets inserted between the claws of the rotor [12], [25], Fig. 3.3.1, poly-phase winding configuration and rectangular conductor winding as shown in Fig. 3.3.2 [12]. An additional drawback of claw-pole machines concerns the eddy-current losses in the solid-iron claw-pole, which results in lower overall efficiency.

Permanent magnet machines

Based on the rotor structure, PM machines can be categorized as surface mounted PM type, SMPM, and interior PM type, IPM.

The former type uses magnets attached to the rotor surface to create the rotor flux. The SMPM topology has the highest torque density and efficiency. However, the narrow constant power speed range make this machine topology not suitable for starter generator application.

Fig. 3.3.1 Claw-pole machine: magnets inserted between the pole [11]

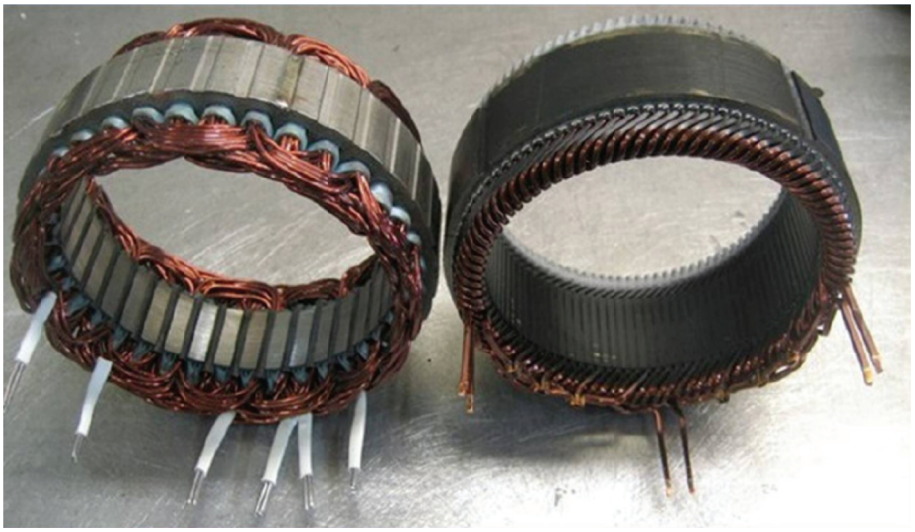

Fig. 3.3.2. Stator winding solutions:
stranded wire (left) and rectangular conductor (right).

The rotor configuration of latter type allows combining the electromagnetic torque coming from the magnet with the reluctance torque due to the saliency [26]. In particular, the rotor is created by adding a small amount of magnets inside the barriers of a synchronous reluctance machine.

On the one hand this configuration is widely accepted for hybrid electrical vehicle applications since it ensures a high torque density, high efficiency and a wide flux weakening range [27] [28] [29]. On the other hand, the non-eliminable presence of the back EMF induced by the permanent magnets implies problems in fault management; furthermore, the variable cost of the rare earth magnets discourages the use of PM machines for mass production applications. In addition, multiple flux barriers might arise mechanical problem at high rotational speeds.

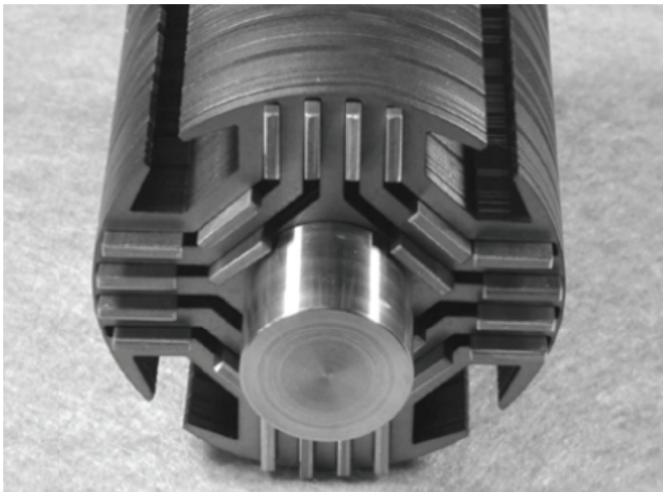

(a)

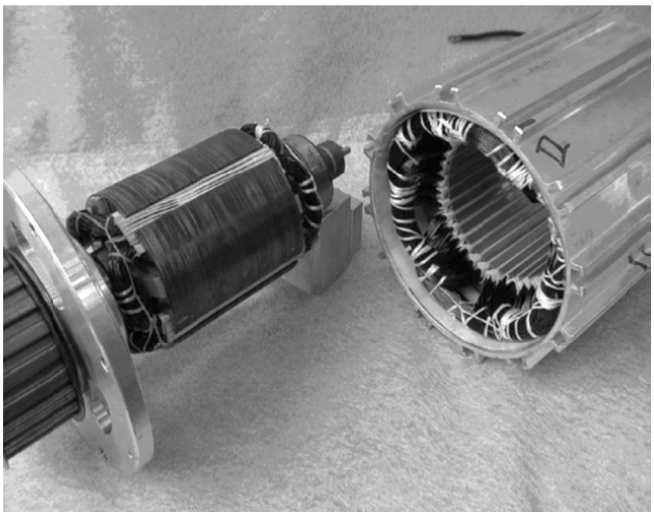

(b)

Fig. 3.3.3. Biaxial excitation generator for automotive, BEGA, prototype [28].
(a) four-poles rotor of BEGA prototype (without field coil)
(b) details of the prototype

An example of biaxial excited generator, BEGA, is reported in Fig. 3.3.3, this machine combines the IPM wide CPSR ability with the claw-pole lower peak stator current for the cranking torque [28]. BEGA has a conventional stator with uniform slots and a three-phase distributed winding. While the rotor cross section (Fig. 3.3.3a) is characterized by the following: (i) salient laminated rotor poles, (ii) hetero-polar dc excitation winding (in the d-axis), (iii) multiple flux barriers in the rotor poles and (iii) lower cost PMs located in the flux barriers (in the q-axis).

3.3.2. Asynchronous machines

The induction machine has a conventional ac stator and a wound-winding or cage rotor. The former rotor structure is rarely used in automotive application since it requires additional axial length for slip rings and brushes for the three-phase excitation field winding. The latter rotor solution is very promising as starter-generator since it allows a reliable, robust and inexpensive mechanical design [30], [31] and [32]. Despite the lower torque density and power factor with respect to IPM, this topology has high overload capability as well as good "intrinsic" flux-weakening characteristics. In addition, the absence of permanent magnet on the one side allows avoiding the costs of rare earth materials and on the other side the handling of fault conditions is relatively simple and effective.

With the aim to improve both torque density and efficiency, especially at low speed, the stator winding is produced with rectangular bar conductors instead of conventional stranded wire [32]. Similarly, to reduce the rotor losses, the copper is used as a substitute of aluminum for the squirrel cage manufacturing [33]. In Fig. 3.3.4 the cost-effective IM proposed by GM for belt starter-alternator applications is shown.

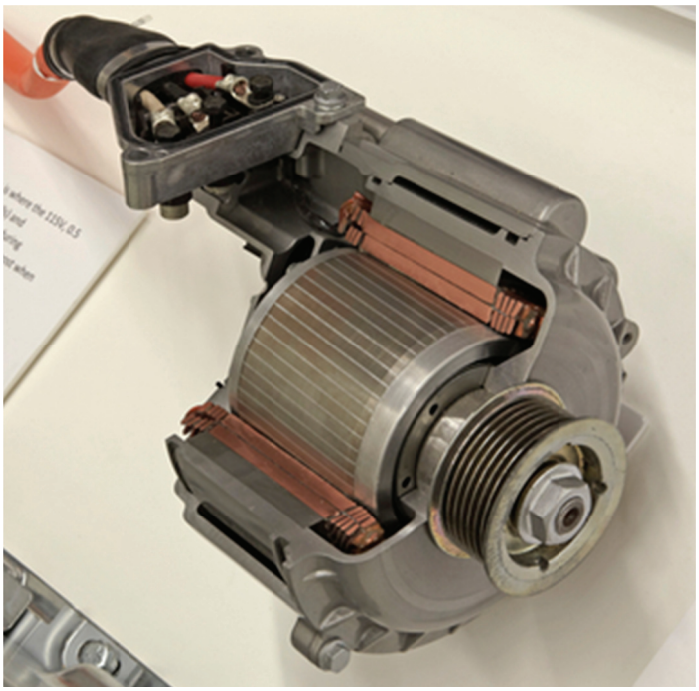

Fig. 3.3.4. GM e-assist belt alternator starter, BAS [32].

The comparison of the characteristics for the three machine topologies above described is summarized by qualitative analysis in Table II. From this table is possible to notice that the induction machine topology represents a good trade off in terms performances and costs.

TABLE II
ELECTRICAL MACHINES TOPOLOGIES FOR BELT-STARTER GENERATOR APPLICATION

	WRS	**IPM**	**IM**
Efficiency	Low	High	Medium
Speed range	Wide	Wide	Wide
Overload	Low	High	High
Power density	Low	Very high	High
Robustness	High	Low	High
Cost	Low	High	Low

3.3.3. Multiphase electrical machines

As described in the previous section, electrical machines for automotive application have to satisfy several challenging requirements from which it can be summarized the following key points:

- Reduced weight and volume
- High efficiency
- Low vibration and acoustic noise
- Robustness
- Fault-tolerance
- Low production cost

An interesting solution to fulfill all the aforementioned requirements is represented by multiphase winding configuration. In the literature it has been already referenced that multiphase drive (with number of phase higher than 3) present several advantages compared to their three-phase counterpart [35]-[37].

The electromagnetic structure of multiphase machine is substantially the same as of conventional three-phase ones and the winding topology can be distributed type as well as fractional-slot concentrated type.

Depending on the electrical displacement between two adjacent phases, the multiphase winding can be categorized as symmetrical or asymmetrical. The former topology is characterized by a displacement equal to $2\pi/N_{ph}$ between the

magnetic axes of two consequent phases with N_{ph} an odd prime number. In the latter solution the displacement between the two phases is equal to π/N_{ph} with N_{ph} an even number or an odd non-prime number [38].

The selection of the most suitable number of phase depends on many aspects, in particular the system reliability increase as the phase number increases. If one or more phases are missing the multiphase machine can still operate and the healthy phase, if thermally admissible, should be overloaded to maintain the same performance.

Moreover, the number of phases has an impact on the time-harmonic components in the excitation waveform. Such supply components produce pulsating torque at frequencies that are even multiples of the fundamental excitation frequency. Thus, increasing the number of phases increases also the frequency of the lowest torque ripple component resulting in reduced vibration and acoustic noise.

With the increase of number of phase and comparable dimensions, it becomes difficult to adopt a number of slot per pole per phase higher than one; despite this, it can be achieved a lower space-harmonics content in the air-gap magneto-motive force with respect to three-phase counterpart.

Finally, increasing the number of phase and considering a fixed voltage and power allows to split the overall current in more than three-phases, the so-called power splitting concept. This strategy allows to increase the torque per *rms* ampere for the same machine volume as well as the size reduction of the conductor and the reduction of voltage and current rating of the power device. Among the key features of multiphase drive solution, it can be highlighted the potential size reduction of the overall drive system with the possibility to integrate the machine and converter in one device.

With reference to the literature, the multiphase drives topologies can be classified as:

- Conventional multiphase with single machine neutral point, Fig. 3.4.1
- Multiple of independent single-phase units, Fig. 3.4.2
- Multiple of independent three-phase units, Fig. 3.4.3

The last two configurations fully satisfy the requirements of fault-tolerant operation for safety critical applications. In particular, the multiple of independent single-phase unit configuration allows the best fault tolerant operation since each converter can be disconnected from dc source. In addition, this configuration has the highest voltage utilization of the *dc* link since the maximum peak phase voltage is the dc-link voltage.

The topology with multiple independent three-phase units is usable when the phase number is a multiple of three and the stator consists of independent three-phase winding with isolated neutral points. This configuration is less attractive with respect to the single-phase unit configuration from the fault-tolerant point of view. However, the converter can use the well-established three-phase power electronics modules, reducing the design time and cost. Furthermore, the multiple three-phase approach usually leads to simpler control schemes due to lower number of independent currents with respect to single-phase approach.

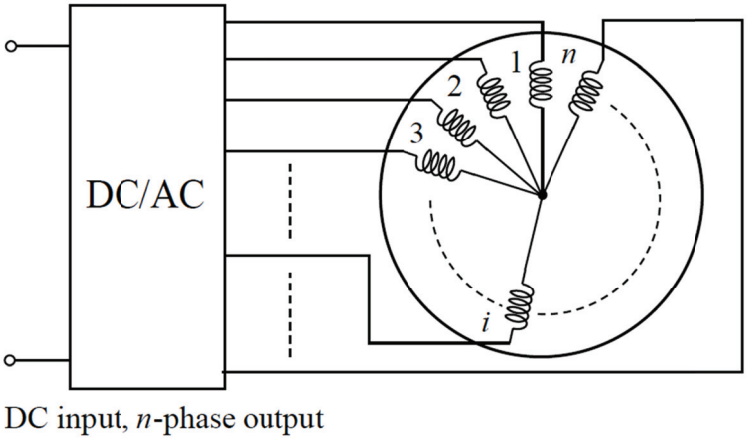

Fig 3.4.1. Conventional multiphase topology with single neutral point [35].

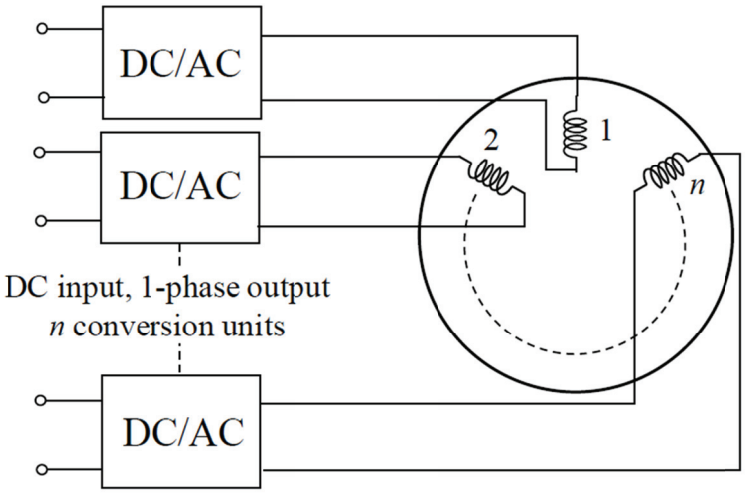

Fig. 3.4.2. Multiphase topology with multiple single-phase units [35].

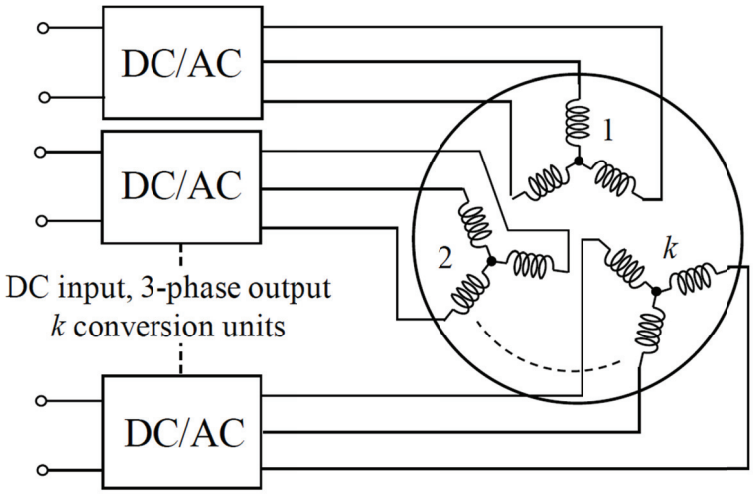

Fig. 3.4.3. Multiple topology with multiple three-phase units [35].

In recent years the use of multiphase machines in transportation applications has experienced a significant growth despite this technology has aroused interest since 1920s when it was used to satisfy the demand for high power generators [38]. In particular, a three-phase machine was converted into a six-phase one to overcome the current limit imposed by the circuit breakers of that period [23]. In the 1960s, when inverter-fed ac drives were in the initial development stage, multi-phase windings appeared as the best solution to minimize the low frequency torque ripple due to six-step modulation [39]. The interest on multiphase technology was renewed in the 90s when the advantages of power segmentation and fault tolerance attract significant attention for electric ship propulsion which remains nowadays one of the main application areas for multiphase variable-speed drives [40].

Currently, the relevance of multiphase solutions is widespread both in academia and industry in the whole transport sector. In the rail vehicles multi three-phase solutions are sporadically used to withstand the different level of catenary voltage [41]. In aeronautical application, in the frame of the concept of More Electric Aircraft, multiphase technology is very promising due to its fault tolerance capability [42] [43].

The use of multiphase technology in automotive application is still limited since the power level can be managed with three-phase drives so the multiphase solution is perceived as complicate solution in terms of component and control scheme. However, in literature several examples of multiphase machines and converters can be found [14], [12] and [44]. This topology is particularly appealing in safety critical components such as the power steering [45].

In addition, in this application the torque ripple can be an issue since the driver can feel it. Therefore, multiphase solutions may become a key requirement both for safety and comfort purpose.

Multiphase drives are very popular even in low voltage-high power automotive applications such as starter-alternator; in this case the application exploits the advantage in terms of power segmentation for reducing the per-phase current of both, machine and power converter. Among the multiphase solution of starter-generator presented in literature, the five-phase and six-phase options are certainly the most reported solutions [38]. Therefore, the seven-phase and the nine-phase solutions are also selected for this application.

3.4. Conclusion

Since the application requires high torque density and wide constant power speed range, only IPM and IM can be considered as viable candidates. Although IPM machines have high efficiency and the highest power density, the rising cost of rare earth materials discourage the use of PM machines for mass production application. Despite the lower torque density and power factor, the IM has been considered the best candidate for the application under consideration for its low cost, high overload capabilities, and good "intrinsic" flux-weakening characteristics. In addition, a reliable and robust mechanical design can be guaranteed. In the absence of a permanent-rotor magnetization, for this machine type, the handling of fault conditions is relatively simple and effective.

For what it concerns the winding topology, the multiphase configuration seems to be essential to fully satisfy the required performance within the imposed constrains. Considering that, the multi-single phase configuration has higher fault tolerance and better exploitation of the dc link voltage but, for automotive application, it is considered as too much complicated in terms of component count and also as control scheme. Thus, the multi-three phase configuration with two independent three-phase sets represent a good solution in term of current splitting and system complexity.

3.5. Magnetic materials for high performance electrical machines

A reliable design of an electrical machine able to satisfy the target specifications requires an accurate understanding of the magnetic material characteristics. Therefore, this section summarizes a characteristic comparison and selection guide for selected magnetic material used in high performance rotating electrical machine presented as described in [XII].

The most used magnetic material for electrical machines cores are based on three pure components: iron (Fe), cobalt (Co) and nickel (Ni), which are alloyed with other materials in order to improve their physical properties (permeability, mechanical strength, electric conductivity, etc.). Therefore, the typical magnetic material alloy, which are produced in thin lamination sheets (0.1-1 mm) are Silicon–Iron (SiFe), Cobalt–Iron (CoFe) and Nickel–Iron (NiFe).

3.5.1. Silicon-iron – SiFe

Non-oriented silicon-iron is undoubtedly the most used magnetic material in rotational electrical machines. It can be ordered from the producers as semi-processed or fully-processed material. The former does not go through a final annealing process and is delivered without any coating while the letter is provided fully annealed and with the desired coating.

Its chemical composition varies according to the desired physical properties; the main component is iron (93% up to 99%) while the remaining content is shared between silicon, Si, (up to 6.5%), aluminum, Al, (up to 1%) and manganese, Mn, (up to 0.5%). The silicon makes the iron alloy mechanically harder and increases the electrical resistivity. The drawback is a lower saturation magnetization and smaller permeability [XII]. Aluminum has a similar effect on the electrical resistivity and on the permeability of the material. The content of manganese leads to larger grains and thus a higher permeability, though it increases the losses as well [XII].

SiFe with a high silicon-content (up to 6.5%) are typically used for high-speed machines due to their large electrical resistivity and thus low eddy current losses. However, the silicon content not only reduces the maximum flux density and permeability, it also makes the alloy more brittle, leading to more complicated and expensive manufacturing processes.

The most of industrial machines are manufactured with standard non-oriented SiFe laminations, having silicon contents of 0.5% to 3%. Sheet thicknesses of

0.5 mm or thicker keep the manufacturing costs low and it is, in most cases, a good tradeoff between efficiency and costs for general industrial machines. Other SiFe lamination is represented by the so-called thin SiFe alloys (0.1 mm to 0.27 mm thickness). They have around 3% silicon content and thus a lower electrical resistivity. However, the small lamination thickness still keeps the eddy current losses low at the cost of larger core assembly efforts and thus production costs, compared to thicker non-oriented SiFe laminations. Non-oriented SiFe is usually not finally annealed for industrial electrical machines due to the low performance increase with respect to the annealing costs and increased manufacturing time

3.5.2. Cobalt iron – CoFe

CoFe alloy is generally the most expensive with respect to SiFe and NiFe. If alloyed with iron, cobalt reaches the highest maximum saturation magnetization of all materials at room temperature (2.43 T for a 35% Co and 65% Fe alloy [XII]). A typical CoFe alloy for electrical machines has 48- 50% cobalt, around 48% iron, and 2% vanadium. However, it should be mentioned that even for this typical composition there are different grades available, which differ in terms of other alloy additions and annealing behavior.

With the increase of maximum saturation magnetization, it is possible to design electrical machines which are significantly reduced in size and in weight, respectively, which can in turn lead to electrical machines with very high power densities.

CoFe alloys are mainly used in machine for aviation and space applications, where a reduction in weight pays of the higher price. A similar use is observed for electric and hybrid systems in motor sport applications. The mechanical strength of the material versus lower iron losses and a larger magnetic permeability can be controlled by either varying the ratio between the cobalt and iron content in the material [XII], by additional alloying the material with Niobium, or by changing the temperature cycle during the annealing process.

3.5.3. Nickel-iron – NiFe

NiFe laminations are a good choice if iron losses are a key aspect, e.g. for small high-speed machines. From the cost point of view, NiFe alloys lie generally in between CoFe and SiFe lamination sheets. The main advantage is their very low magnetic coercivity, which leads to a superior relative permeability μr compared to CoFe and SiFe materials. However, a drawback is the low saturation

and small maximum flux density. Typical NiFe laminations for electrical machines have a nickel content of 40-50%, where a higher nickel content typically leads to a larger permeability. However, the electric conductivity and thus eddy current losses are also increasing with nickel content [XII].

3.5.4. Manufacturing influence on the magnetic properties

The treatment of the magnetic material during the manufacturing process significantly influences the magnetic properties; cutting and punching the lamination sheets introduce stress and reduce the material permeability especially close to the cut edge. In addition, the stacking technology of the lamination sheets (gluing, welding, interlocking, etc.) and further mechanical treatment introduce stress and short circuits between lamination layers a well as leading to increased eddy current losses [V].

A thermal treatment process (annealing) can largely restore this deterioration of the magnetic properties, as reported in [V]-[XXII]. Therefore, it is mainly a question of the cost if annealing should be applied [XII]. Typically, fully processed SiFe, amorphous materials, and soft magnetic composite materials may be used without a post-manufacturing annealing process, in order to keep the manufacturing costs low. However, for materials such as CoFe and NiFe, the annealing process is indispensable in order to obtain the desired magnetic properties at all. For these materials, a trade-off has to be made between the magnetic and mechanical properties of the material. Higher annealing temperatures support the grain size growth, leading to better magnetic properties and higher saturation magnetization. [V], [XXII].

Despite this, larger grain sizes improve the hysteresis losses and reduce the mechanical strength of the material and its hardness. Thus, the annealing process should be adapted to the needs of the machine design requirements.

3.5.5. Conclusion

Since the application requires cost-effective high torque density machines, the use of CoFe and NiFe for the lamination is discouraged because of their cost. Despite SiFe has low saturation level with respect to CoFe, it represents a good tradeoff between magnetization saturation, losses, mechanical strength and cost.

4. Design of induction starter-generator

4.1. Design procedure

The method used for the preliminary sizing of a double-three phase induction machine is based on classical electromagnetic equations included in an iterative process for convectional three-phase machine. It is worth to notice that the selected stator-winding configuration consists of two independent three-phase systems having 60 electrical degree of shift between the sets, as depicted in Fig. 4.1a. Thus, in each slot there are two different phases in which it flows the same current having opposite sign (see Fig. 4.1b). Hence, the magneto-motive force distribution waveform of a double three-phase configuration is the same like a conventional three-phase system. Under this assumption it is possible to adopt the conventional analytical representation of three-phase electrical machine being aware that the only difference among the stator unit is given by the number of turns. Therefore, the rated voltage adopted during the design procedure, V_r, has to be set twice with respect to the desired rated voltage in double three-phase configuration, $V_{r\_double3ph}$.

The adopted algorithm for the preliminary sizing, presented in [46], is based on a progressive increase of the rotor diameter until the specified rated torque is obtained. For sake of completeness the procedure and the used equations are summarized hereafter.

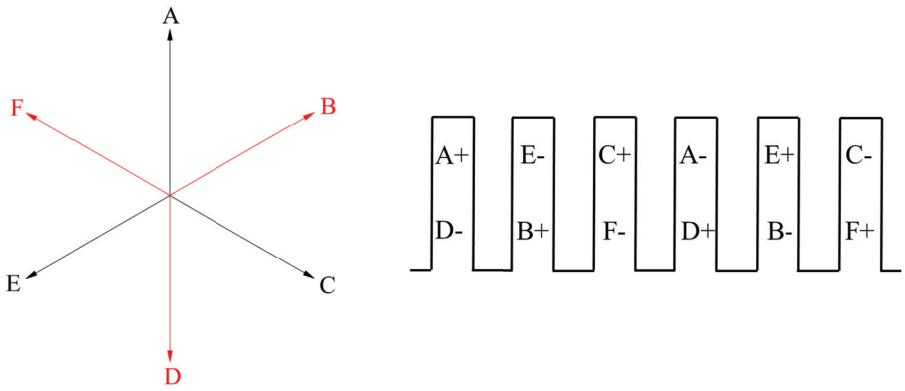

Fig. 4.1(a) MMF diagram of the adopted double three-phase configuration (b) Position in the stator slots of a double three-phase winding (p=2, q=1).

TABLE III.
LIST OF THE REQUESTED DESIGN SPECIFICATIONS

Induction machine rated data		
Parameter	Unit	Name
V_r	V	Phase rated voltage
f	Hz	Rated frequency
Ph	-	Number of phases
N_{pole}	-	Number of poles
T_r	Nm	Torque
Permissible active material stresses		
B_{ag}	T	Maximum air-gap flux density
B_{ts}, B_{ys}	T	Maximum flux density (stator teeth and stator yoke)
B_{tr}, B_{yr}	T	Maximum flux density (rotor teeth and yoke)
J_s, J_r	A/mm^2	rms current density (stator and rotor)
Geometric specifications		
$\lambda=L_{core}/D_r$	-	Rotor aspect ratio
D_{sh}	mm	Shaft diameter
h_{11s}, h_{12s}, w_{0s}	mm	Stator slot enclosure dimensions
h_{11r}, h_{12r}, w_{0r}	mm	Rotor slot enclosure dimensions
h_{ah}	mm	Thickness of the airgap
Pack and filling coefficient		
K_{ir}	-	Lamination pack coefficient
K_{cs}, K_{cr}	-	Filling coefficient of the stator and rotor slots
Stator winding specifications		
q	-	Number of slot per pole per phase
N_r	-	Winding pitch reduction (in slot number)
Rotor winding specifications		
N_{sr}	-	Rotor slot number
$R_i=\tau_i/\tau_p$	-	Rotor skewing ratio
First approximation quantities		
cos φ	-	Rated power factor
ΔV	V	Stator voltage drop at rated load
K_{tor}	-	Corrective coefficient for the torque computation

The requested input data to define the design process are listed in the Table III and they can be categorized as (*i)* design target with the machine rated data and (*ii)* design constrain according to the machine aspect ratio and the acceptable material stresses. Many of these values are well known from the designer, however guidelines for the first choice of the values (e.g. flux densities and current densities) can be found in several handbooks [47]. High values of current density can lead to excessive Joule losses and to consequent motor overheating while high flux density values can lead to high no-load current, low power factor and high iron losses. The shape of the motor is defined by the ratio between the rotor axial length and the rotor diameter. When the machine has to be sized in a defined volume (e.g. when the outer diameter or axial core length are imposed) the λ parameter can be changed in an iterative way until the constraint is respected. The shaft diameter and the airgap thickness can be defined "a priori" or on the basis of the mechanical requirement.

4.1.1. Rotor lamination design

The rotor diameter can be defined, as a first attempt, slightly higher than the shaft diameter ($D_r > D_{sh}$) while the rotor lamination length is defined according to the rotor aspect ratio $L_{core}=\lambda D_r$.

The preliminary problem to be solved is the computation of the rotor slot dimensions according to the defined magnetic and geometrical constraints.

The rotor geometry can have slots with parallel edges (rectangular slots) Fig. 4.2a or tooth with parallel edges (trapezoidal slots) Fig. 4.2b.

The former topology is usually chosen when the rotor cage is produced by using copper bars, while, the latter solution allows a better exploitation of the rotor tooth and it is mostly used in case of die cast rotor cage. However, these two cases are the simplified shape of the rotor slots typically used in induction motors. As known the rotor slot shape is a decisive factor during starting operation therefore they are designed with narrowing or enlarging shape along the radial height for obtaining the desired skin effect.

As a first attempt, the rotor design with complex slot shape can be carried out using the simplified slot shape (rectangular or trapezoidal) and lower the natural filling coefficient K_{cr}. In this way is possible to take into account the incomplete use of the slot area as depicted in Fig. 4.3 where A_3 is the area of the shaped slot and A_2 in the area of the simplified one.

Fig. 4.2. Rectangular slot (a) and trapezoidal slot(b)

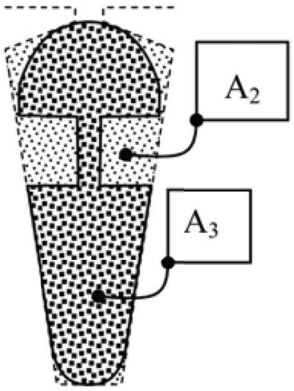

Fig. 4.3 Complex rotor slot shape

Trapezoidal slot

In case of trapezoidal slot, the geometrical computation can be summarized as follows. The fundamental harmonic of the flux for each pole can be evaluated using the equation (4.1)

$$\Phi_{pole} = B_{ag} \frac{2D_r L_{core}}{N_{pole}} \tag{4.1}$$

The maximum flux in the rotor yoke and in the rotor teeth can be determined using the following relations (4.2), (4.3).

$$\Phi_{rotor\ yoke} = \frac{\Phi_{pole}}{2} = B_{ag} \frac{D_r L_{core}}{N_{pole}} \tag{4.2}$$

$$\Phi_{rotor\ tooth} = B_{ag} \frac{\pi D_r L_{core}}{N_{sr}} \tag{4.3}$$

By the rotor yoke and rotor tooth flux values and on the basis of the imposed yoke and tooth flux density (B_{yr} and B_{tr}), the thickness of the rotor yoke and tooth can be obtained by

$$h_{rotor\ yoke} = \frac{\Phi_{rotor\ yoke}}{K_{ir} B_{yr} L_{core}} \tag{4.4}$$

$$w_{rotor\ yoke} = \frac{\Phi_{rotor\ tooth}}{K_{ir} B_{tr} L_{core}} \tag{4.5}$$

At this stage, the rotor lamination drawing can be defined as shown in Fig. 4.4a. Defining the following equation

$$\alpha_{rs} = 2\pi/N_{sr}$$ rotor slot angular pitch

$$D_{ext\_yr} = D_{sh} + 2h_{rotor\ yoke}$$ rotor yoke external diameter

According to Fig. 4.4a the following geometrical dimensions of the rotor slot can be obtained.

$$h_{rg} = \frac{D_r - D_{ext\ yr}}{2} - h_1$$ slot useful height (4.6)

$$w_{br} = \left(D_{ext\ yr} - \frac{w_{rotor\ tooth}}{\sin(\alpha_{sr}/2)}\right) tan\frac{\alpha_{sr}}{2}$$ slot bottom width (4.7)

$$w_{tr} = w_{br} + 2h_{ur}\tan\frac{\alpha_{sr}}{2}$$ slot top width (4.8)

It has to be remarked that these dimensions must be verified in terms of geometrical compatibility, in particular in the following two cases:

Case 1: h_{ur}<0. In this case, the design attempt is aborted and the computation procedure start again with a new increased rotor diameter ($D_r = D_{r\,old} + \Delta D_r$)

Case 2: The bottom width of the trapezoidal slot must be greater than zero

$$w_{br} > 0 \Rightarrow D_{ext\ yr} > \frac{w_{rotor\ tooth}}{\sin(\alpha_{sr}/2)}$$ (4.9)

If this condition is not verified the rotor slot shape will be triangular, but the design it can be considered acceptable, as shown in Fig. 4.4b.

This condition occurs if the rotor tooth width is very large or if the rotor yoke width is very narrow. In this case it is necessary to redesign the slot and to determine the rotor yoke starting from the condition of degenerated slot (triangular). As a consequence, the yoke width, the slot height and the slot width on the top have to be computed following the procedure hereafter

$$w_{br} \equiv 0 \Rightarrow D_{ext\ yr} > \frac{w_{rotor\ tooth}}{\sin(\alpha_{sr}/2)}$$ (4.10)

$$h_{rotor\ yoke} = \frac{D_{ext\ yr} - D_{sh}}{2}$$ (4.11)

$$h_{ur} = \frac{D_r - D_{ext\ yr} - 2h_1}{2}$$ (4.12)

$$w_{tr} = 2h_{ur}\tan\frac{\alpha_{sr}}{2}$$ (4.13)

In this case, the rotor yoke flux density is lower than the imposed one.

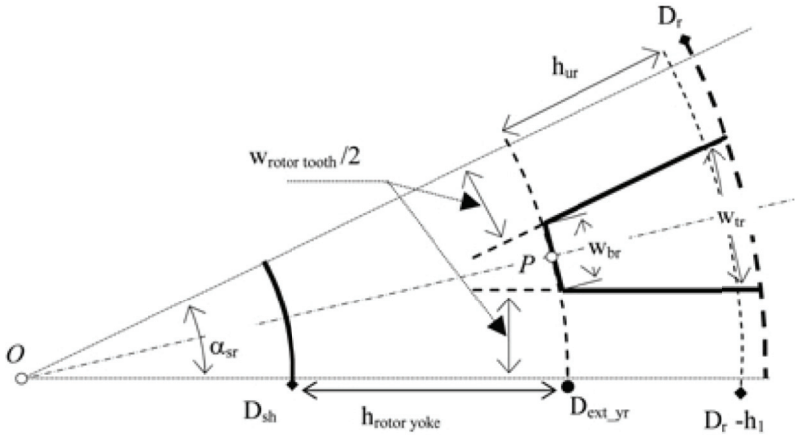

Fig. 4.4a rotor lamination design for trapezoidal rotor slot

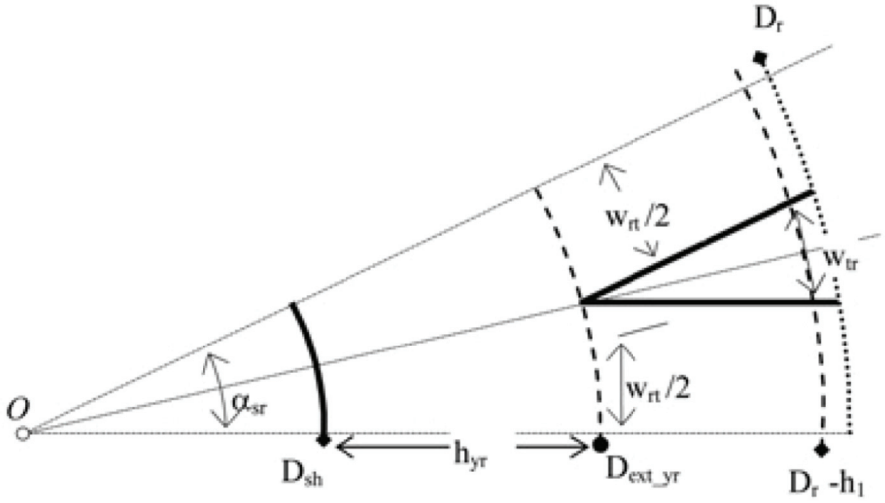

Fig. 4.4b Rotor lamination design for triangular rotor slot

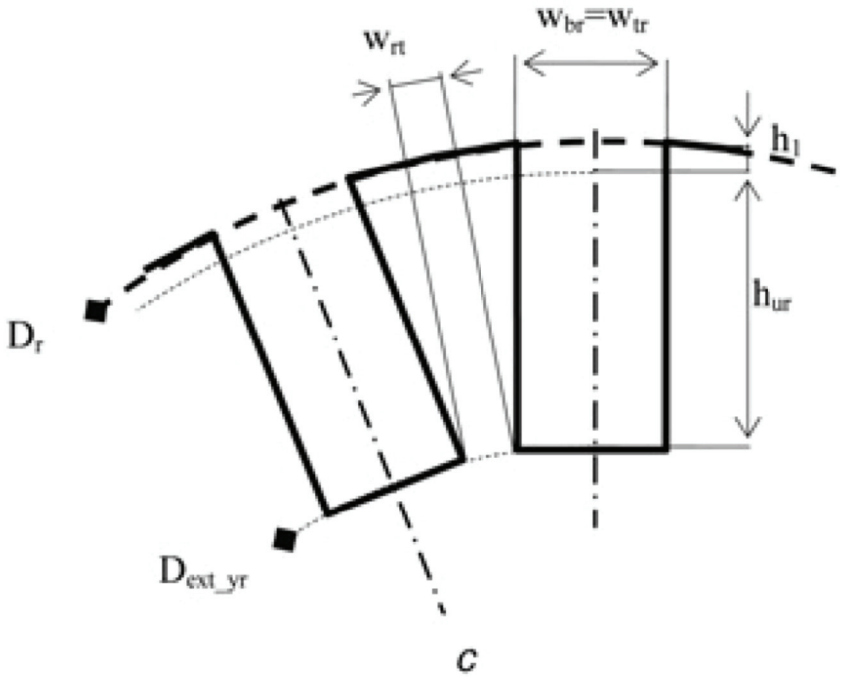

Fig. 4.4c Rectangular slot design

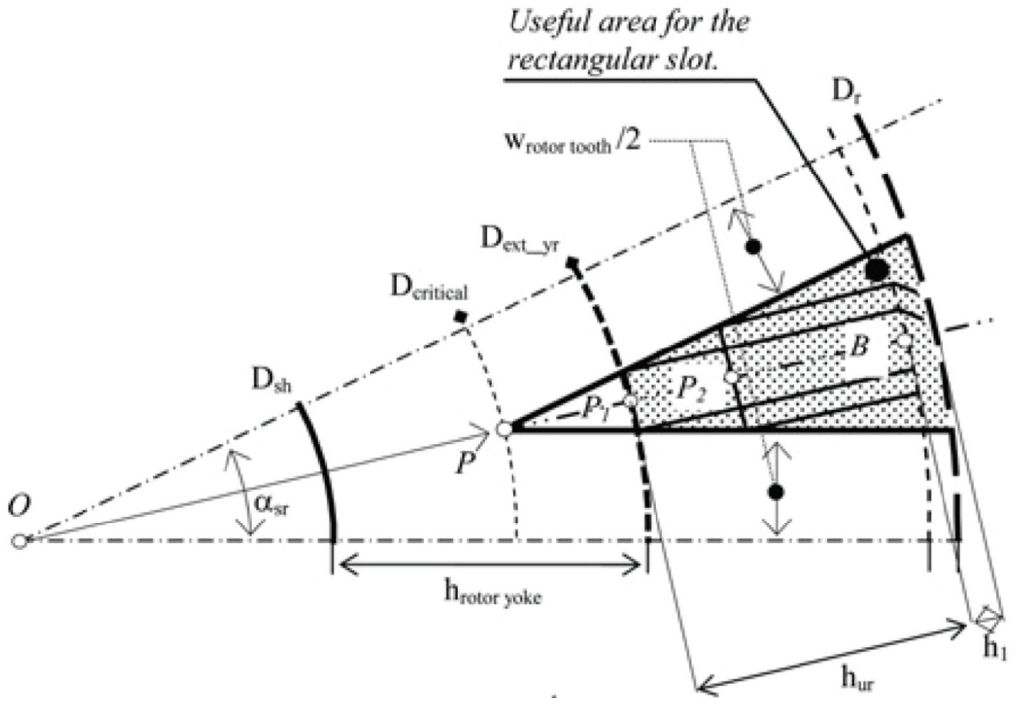

Fig. 4.4d Rotor lamination design for rectangular rotor slot

Rectangular slot

Rectangular slot implies variable tooth width as shown in Fig. 4.4c. Since the flux density B_{tr} has been defined as the maximum value reached in the tooth, this

value will be verified in the bottom of the tooth. Consequently, in the other tooth sections the magnetic stress will be lower than the imposed one. Even in this case, the yoke height and the tooth width will be computed from the flux in the yoke and in the tooth according to (4.2) and (4.3).

The external diameter of the rotor yoke $D_{ext\,yr}$ and the slot useful height h_{ur} are defined by (4.14) and (4.15)

$$D_{ext\_yr} = D_{sh} + 2h_{rotor\ yoke} \tag{4.14}$$

$$h_{ur} = \frac{D_r - D_{ext\,yr}}{2} - h_1 \tag{4.15}$$

These preliminary geometrical computations must be verified taking into account the possibility to obtain the rectangular slot. In particular, the useful height of the slot, h_{ur}, must be positive, if this condition is not verified the procedure for trapezoidal slot design can be applied.

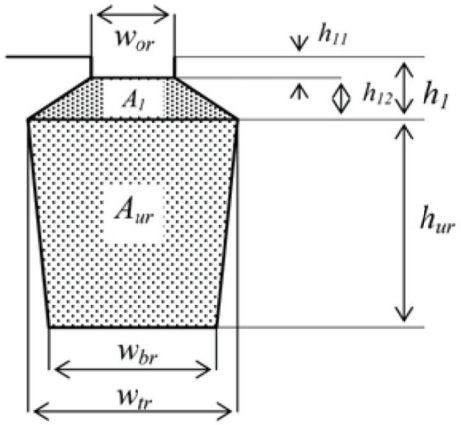

Fig. 4.5 Rotor slot geometrical parameters

The previous relations allow defining an area where the rectangular slot can be included, see Fig. 4.4d. Nevertheless, in this area several possible rectangular slot shapes can be obtained. The most suitable solution is not definable "a priori" but it is conditioned by the necessity of deep slot (deep bar: P1 in Fig. 4.4d) or by the necessity of a maximum area slot (minimum resistance: P2 in Fig. 4.4d). In particular, the maximum rectangular slot area can be obtained when the slot height is equal to half of the segment PB, see Fig 4.4d.

$$h_{ur\ opt} = \frac{1}{2}\ PB = \frac{1}{2}\left(\frac{D_r}{2} - h_1 - \frac{w_{rotor\ tooth}}{2\sin(\alpha_{sr}/2)}\right) \quad (4.16)$$

Consequently, the external rotor yoke diameter results equal to

$$D_{ext\ yr\ opt} = \frac{w_{rotor\ tooth}}{2\sin(\alpha_{sr}/2)} + \frac{D_r}{2} - h_1 \quad (4.17)$$

This condition is possible only if the rotor yoke external diameter computed by (4.14) is lower than the one computed by (4.17).

Finally, the rectangular slot geometry can be computed by (4.18) and (4.19)

$$h_{ur} = \frac{D_r - 2h_1 - D_{ext\ yr}}{2} \quad (4.18)$$

$$w_{br} = w_{tr} = \left(D_{ext\ yr} - \frac{w_{rotor\ tooth}}{\sin(\alpha_{sr}/2)}\right) tan\frac{\alpha_{sr}}{2} \quad (4.19)$$

4.1.2. Torque Computation

Once the first attempt of rotor lamination dimensions have been computed, it is possible to compute the deliverable torque. The rotor dimensions (length and diameter) will have to increase step by step until the obtained torque will be equal or greater than the requested one. The procedure for the electromagnetic torque computation is hereafter reported.

Rotor useful area

From the rotor slot dimensions is possible to obtain the useful slot area that represents the available slot portion for the winding conductors.

Generally, the useful rotor slot area A_{ur} can be defined (both for trapezoidal and rectangular slot) by the following relation

$$A_{sr} = A_{ur} + A_1 = (w_{br} + w_{tr})\frac{h_{ur}}{2} + A_1 \quad (4.20)$$

Where A_1 represent the slot-closing region as shown in Fig. 4.5. It is important to highlight that the dimensions of the closing region can be defined "a priori" during the initial design stage. Finally, the extended equation can be obtained

$$A_{sr} = (w_{br} + w_{tr})\frac{h_{ur}}{2} + (w_{or} + w_{tr})\frac{h_{12}}{2_{\,1}} \tag{4.21}$$

In case of skewing of the rotor, the available area is reduced according to (4.22)

$$A'_{sr} = K_{gi}A_{sr} \tag{4.22}$$

Where K_{gi} is the geometrical skewing coefficient

$$K_{gi} = \frac{L_{core}}{\sqrt{L_{core}^2 + \tau_i^2}} \tag{4.23}$$

The skew pitch τ_i is a fraction of R_i of motor pole pitch

$$\tau_i = R_i\tau_p = R_i\frac{2\pi D_r}{N_{pole}} \tag{4.24}$$

Finally, it is possible to define the net area of the conductive material and, as a consequence, from the imposed current density it can be computed the *rms* current in the rotor bar (4.25)

$$I_{r,rms} = J_r K_{cr} K_{gi} A_{sr} \tag{4.25}$$

Flux density distribution along the air-gap

Considering a progressive index k for the number of the rotor slot (k from 1 to N_{cr}), the active air-gap flux density in correspondence to the rotor slot k, in a generic time instant, can be written as follow

$$B_k = B_{ag}\sin\left(\frac{N_{pole}}{2}\alpha_k\right) \tag{4.26}$$

Where $\alpha_k = k\frac{2\pi}{N_{sr}}$

In case of skewed rotor, the flux density to take into account for the electromechanical interaction is the average one along the bars (23)

$$B_{m,k} = \chi_i B_{ag}\sin\left(\frac{N_{pole}}{2}\alpha_k\right) \tag{4.27}$$

where

$\chi_i = \frac{2}{R_i\pi}\sin\left(\frac{R_i\pi}{2}\right)$ is the electric skewing coefficient and $R_i\pi$ is the electric skewing angle

Current distribution in the rotor slots

The fundamental distribution of the current induced in the rotor conductors by the fundamental flux density can be defined as follows

$$I_{r,k} = \sqrt{2} I_{r,rms} \sin\left(\frac{N_{pole}}{2}\alpha_k - \psi\right) \tag{4.28}$$

Where ψ is the angle between current and voltage induced in the bar. This angle is a function of the slip frequency and it can be determined by means (4.29)

$$\tan\psi = slip\omega \frac{L_{\sigma,bar}}{R_{bar}} \tag{4.29}$$

Where L_{bar} and R_{bar} are the leakage inductance and resistance of the conductive cage, respectively. Assuming that the slip is very small at rated load condition, the angle ψ can be considered equal to zero.

Torque determination

The motor torque can be evaluated by the interaction between the air-gap flux density distribution (sinusoidal), B_{ag}, and the rotor bar currents, I_r. The torque can be computed as the sum of the contributions of each bar.

$$T = \sum_{k=1}^{N_{sr}} B_k I_{r,k} \frac{L_{core} D_r}{2} \tag{4.30}$$

The addition of the contributions can be written as follow.

$$\begin{aligned} T &= \frac{\sqrt{2}}{2}\chi_i B_{ag} I_{r,rms} L_{core} D_r \sum_{k=0}^{N_{sr}-1} \sin\left(\frac{N_{pole}}{2}\alpha_k\right)\sin\left(\frac{N_{pole}}{2}\alpha_k - \psi\right) \\ &= \frac{\sqrt{2}}{4}\chi_i N_{sr} B_{ag} I_{r,rms} L_{core} D_r \cos\psi \end{aligned} \tag{4.31}$$

Highlighting the stress indexes and geometrical coefficients, the torque can be expressed

$$T_{design} = K_{tor}\frac{\sqrt{2}}{4}\chi_i N_{sr} B_{ag} J_r K_{cr} K_{gi} A_{sr} L_{core} D_r \quad (4.32)$$

The coefficient K_{tor} is lower than 1 (typically 0.9-0.95) and it accounts for:

- The phase delay ψ between rotor current and flux density
- The mechanical losses of the machine
- The additional torque due to higher spatial harmonics

4.1.3. Final design step

Once the rotor dimensions D_r and L core are defined for deliver the required torque, it is possible to design the others part of the electrical machine.

Cage ring cross-section

The cross section of the end ring can be evaluated taking into account the ring and bar currents

$$\frac{I_{ring}}{I_r} = \frac{1}{2\sin(\pi N_{pole}/N_{sr})} \quad (4.33)$$

Assuming to have the same current density both in the bars and in the end-rings, the ring cross section can be computed by

$$A_{ring} = \frac{K_{cr} K_{gi} A_{sr}}{2\sin(\pi N_{pole}/N_{sr})} \quad (4.34)$$

Stator Phase winding

Considering the specification imposed for the stator winding such as V_r, q, n_r and cosφ, it is possible to compute the number of turn of the winding. The rated E.M.F., E_r, induced in the stator phase winding by the air-gap flux density distribution of amplitude B_{ag}, can be approximated as $E_r = V_r - \Delta V$. For a typical three-phase winding structure with shortened pitch, the stator winding coefficient K_w is defined by

$$K_w = K_w(q, n_r) = \frac{\cos(n_r \pi/6q)}{2q\sin(\pi/6q)} \quad (4.35)$$

Then, the number of conductors in series per phase Z_{ph} for obtaining the air-gap flux density distribution able to produce the requested EMF are:

$$Z_{ph} = \frac{\sqrt{2} E_r N_{pole}}{2\pi f_r K_w \chi_i B_{ag} D_r L_{core}} \quad (4.36)$$

As a consequence, the number of conductors in series per slot results

$$Z_c = \frac{Z_{ph}}{qN_{pole}} \tag{4.37}$$

The number of conductors Z_c must be approximated to an integer number or to a simple fraction of the pole number if the winding will be produced connecting in series or in parallel the poles.

Stator phase current

Once the conductor is series per phase Z_{ph} and the rotor bar current I_r are known, it is possible to obtain in first approximation the stator phase rated current. In fact, from the magneto motive force production point of view, the rotor bar current I_r is equivalent to a fictitious stator current I_r' flowing in stator winding. This equivalent current I_r' can be calculated by

$$I_r' = \frac{N_{sr}}{3K_w Z_{ph}} I_r \tag{4.38}$$

The stator phase current includes both magnetizing current and rotor current referred to the stator. Since the magnetizing is still not known, it is possible to obtain the rated power factor $cos\varphi$ in order to estimate the approximated stator current.

$$I_s \simeq \frac{I_r'}{\cos\phi} \tag{4.39}$$

In terms of vector diagrams, the adopted simplification is shown in Fig. 4.6 however the committed error is negligible at this design step. Since the power factor at rated condition depends on several quantities and parameters (leakage reactance, number of poles, air-gap thickness etc.) only when the design will be completed a reliable estimation of the actual power factor is possible. At this design step a prudential power factor value of 0.7-0-85 can be used.

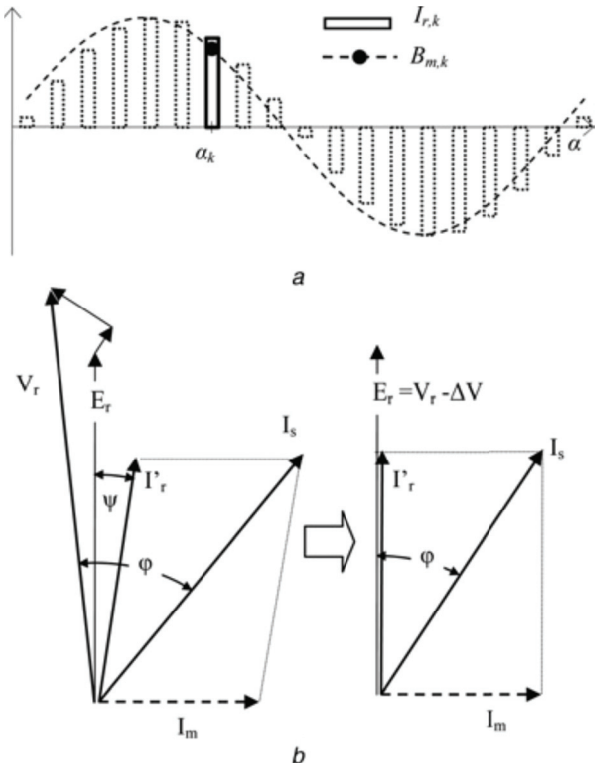

Fig. 4.6 Electromagnetic quantities: (a) Flux density and rotor bar current distributions around the airgap. (b) Vector diagram in rated condition (left side) and the adopted approximation (right side)

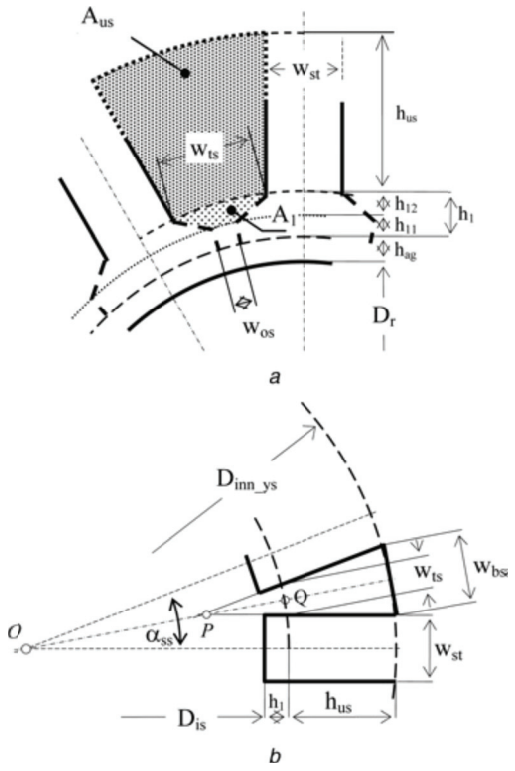

Fig. 4.7 Definition of the stator slot shape (a) General layout of the stator slot (b) Trapezoidal slot: useful height determination

Stator slot dimensions

The stator slot number is $N_{ss} = 3qN_{pole}$ and their section have to be dimensioned for supporting the requested stator current according to (4.40)

$$A_{ss} = 3\frac{Z_{ph}I_s}{N_{ss}K_{cs}J_s} \tag{4.40}$$

Where K_{cs} is the stator slot fill coefficient and J_s is the desired stator current density. The difference between the stator inner diameter and the external rotor diameter is equal to twice the air-gap thickness h_{ag}

$$D_{is} = D_r + 2h_{ag} \tag{4.41}$$

The minimum width of the stator tooth can be evaluated taking into account the maximum stator tooth flux density

$$w_{st} = \frac{B_{ag}\pi D_{is}}{K_{ir}B_{ts}N_{ss}} \tag{4.42}$$

The stator slot width at the top of the slot (close to the air-gap) can be obtained as difference

$$w_{ts} = \frac{\pi(D_{is}+2h_1)}{N_{ss}} - w_{st} \tag{4.43}$$

Where $h_1$is the stator slot closing region height, as shown in Fig.4.7a. As for the rotor lamination, rectangular and trapezoidal slot shape can also be considered for the stator lamination. However, in this case the problem to be solved is different, in fact the slot area is known and the slot height has to be determined. With reference to the trapezoidal geometry shown in Fig. 4.7a is possible to define the useful area of the slot as $A_{us}=A_{ss}-A_1$

Where A_1 is the closing zone area of the stator slot that can be calculated by (4.44)

$$A_1 = \frac{1}{2}(w_{ts} + w_{os})h_{12} \tag{4.44}$$

Independently of the slot shape, the following equation must be verified

$$A_{us} = \frac{w_{ts}+w_{bs}}{2} h_{us} \tag{4.45}$$

Trapezoidal slot

Defining the angular pitch of the stator slot as $\alpha_{ss}=2\pi/N_{ss}$, the slot bottom width w_{bs} can be computed by the following equations

$$w_{bs} = w_{ts}\left(1 + \frac{h_{us}}{QP}\right) \tag{4.46}$$

$$QP = \frac{D_{is}+2h_1}{2} - \frac{w_{st}}{2\sin(\alpha_{ss}/2)} \tag{4.47}$$

In this case, the slot useful height h_{us} has to computed by solving (4.48) rejecting the inconsistent solution

$$\begin{cases} A_{us} = w_{ts}h_{us} + \frac{1}{2}w_{ts}\frac{h_{us}^2}{QP} \\ h_{us} = \sqrt{\frac{2A_{us}QP}{w_{ts}} + QP^2} - QP \end{cases} \tag{4.48}$$

Rectangular slot

In case of rectangular slots, the bottom width is equal to the top width; as a consequence, the following relations can be defined

$$w_{bs} = w_{ts} \tag{4.49}$$

$$h_{us} = \frac{A_{us}}{w_{ts}} \tag{4.50}$$

Stator yoke

The height of the stator yoke must support the stator yoke flux respecting the imposed maximum flux density B_{ys}

$$\Phi_{stator\ yoke} = B_{ag} \frac{D_r L_{core}}{N_{pole}} \tag{4.51}$$

$$h_{stator\ yoke} = \frac{\Phi_{stator\ yoke}}{K_{ir} B_{ys} L_{core}} \tag{4.52}$$

The stator yoke inner diameter is defined by (4.53)

$$D_{inn\ ys} = D_{is} + 2(h_1 + h_{us}) \tag{4.53}$$

Finally, the external stator yoke diameter $D_{ext\ ys}$ can be computed as

$$D_{ext\ ys} = D_{inn\ ys} + 2h_{stator\ yoke} \tag{4.54}$$

Remarks

The described approach allows the preliminary electromagnetic sizing of induction machines defining the geometrical dimensions of stator and rotor lamination and the three-phase stator winding structure. Considering that for the starter-generator under study was selected a double three-phase winding configuration (60 electrical degree shift), it is necessary to refer the obtained three-phase results into the wanted winding topology. In particular, the number of conductor in series per phase of the double three-phase system, $Z_{double\text{-}3ph}$, are equal to $Z_{double\text{-}3ph} = Z_{ph}/2$.

In addition, the obtained results have to be considered as input data for the design refinement step. In particular, a revision of the initial stator and rotor lamination geometries is necessary to take into account more realistic slot shapes (fillets, chamfers, special shape etc.). Furthermore, the design has to be evaluated electrically, thermally and mechanically in order to verify the full specific compliance.

4.2. Design description

Among the six-phase induction machines, it has been selected a double three-phase solution (with insulated neutral points), where the magnetic axes of the stator phases are shifted by 60 electrical degrees. As previously mentioned, this winding configuration allows obtaining a magneto-motive force distribution equal to the one produced by a conventional three-phase winding topology. Therefore, the initial electromagnetic sizing of the prototype has been done in accordance to the methodology previously described for a three-phase machine considering the input data listed in Table IV. It should be remarked that the rated voltage adopted during the design procedure is two times the voltage required in double-three-phase configuration.

Considering that the maximum phase voltage obtainable from a 48 V *dc* power supply is 19.5 V_{rms} (4.2.1), the rated phase voltage in double-three phase configuration has been defined equal to 16.5 $V_{rms.}$ at 350 Hz (33 V_{rms} considering an equivalent three-phase winding configuration). The maximum available phase voltage value of 19.5 V_{rms}, is therefore used to reach the top speed; in this condition, the corresponding supply frequency is equal to 1300 Hz.

$$V_{phase,rms} = \frac{V_{dc} \cdot 1.15}{2 \cdot \sqrt{2}} = \frac{48 \cdot 1.15}{2 \cdot \sqrt{2}} = 19.5\ V \tag{4.2.1}$$

Since the machine is required to operate during short-term load condition, it has to be remarked that reference torque as well as the design stress indexes of the materials listed in Table IV (stator and rotor current density and flux density) are referred to a load peak.

The design procedure leads to obtain a solution with the stator outer diameter and the active axial length equal to 150 mm and 50 mm, respectively. These overall dimensions are compatible with the volume constraints previously discussed and they bring to a challenging power and torque density of 11 kW/dm^3 (11 MW/m^3) and 50 Nm/dm^3 (50 kNm/m^3, peak value/active volume) respectively. The design is then refined by means of analytical computations ([48], [49]) and 2D Finite Element Method (FEM) simulations, mainly for the shape of stator teeth and rotor slots. The preliminary assessment of the thermal capability under such high dynamic application is analyzed by means of a simplified thermal model.

Regarding the machine magnetic structure, the conventional silicon iron laminations M270-35A have been adopted for mass-production market reasons, whose magnetic property can be found in [50].

Starting from the same specifications two different prototypes have been design and produced; the only difference between two machines is the rotor, which is designed with closed slots in the first prototype and open slots in the second one. The aim is to investigate the trade-off between electromagnetic performance and mechanical issues due to the high rotating speed.

TABLE IV
THREE-PHASE EQUIVALENT DESIGN INPUT DATA

Induction machine rated data		
Parameter	Unit	Name
V_r	V	33
f	Hz	350
Ph	-	3
N_{pole}	-	8
T_r	Nm	30
Permissible active material stresses		
B_{ag}	T	0.85
B_{ts}, B_{ys}	T	1.6, 1.6
B_{tr}, B_{yr}	T	1.5, 1.5
J_s, J_r	A/mm^2	25, 24
Geometric specifications		
$\lambda=L_{core}/D_r$	-	0.5
D_{sh}	mm	30
h_{ah}	mm	0.3
Pack and filling coefficient		
K_{ir}	-	0.95
K_{cs}, K_{cr}	-	0.7, 0.95
Stator winding specifications		
q	-	1.5
N_r	-	1
Rotor winding specifications		
N_{sr}	-	58
First approximation quantities		
cos φ	-	0.8
ΔV	V	5%

4.2.1. Magnetic core

Stator lamination

In the first approximation, the pole count does not have direct consequence in the torque production [51], [52]. However, it should be borne in mind that several other machine features are depending on the pole number selection, in particular when fixed dimension are considered.

One of the most significant difference concerns the smaller flux per pole resulting from increasing the number of poles [51]. Considering the same peak flux density and spatial flux variation, the flux per pole is proportional to the pole area that decreases as the pole number increases. As an example to keep the same flux density in the stator and rotor yokes, the yoke thickness of the eight pole machine it should be half that a four-pole machine. So for the same stator diameter, the eight-pole machine has higher rotor diameter and thus it will deliver more torque.

In addition, the number of pole influences the magnetic circuit of the machine with effects on the magnetizing reactance. In particular, the magnetizing reactance decreases with the pole pair increase, resulting in a lower power factor for machines having high number of poles. At fixed rotating speed, the pole pair impacts on the fundamental supply frequency and thus on core losses and additional losses in the stator winding.

Hence, during design step a fair evaluation of the pole count has to be done considering the total losses, efficiency, power factor, and the overall torque-speed requirements.

For the case under study, the trade-off in the pole number selection, leads to the 8-pole configuration. Even if the stator diameters are relatively small, 72 stator slots have been used to accommodate the six-stator phases with a number of slots per pole per phase higher than one. The stator slots have been designed with a rectangular shape to facilitate the accommodation of the stator bar winding; the obtained preliminary dimensions have been then refined considering the tradeoff between electromagnetic performance and manufacturing issues of the winding process. The details of the stator slot are shown in Fig. 4.2.1.1

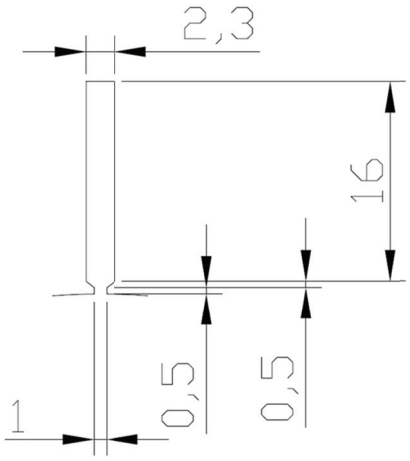

Fig. 4.2.1.1 Stator slot dimensions

Rotor lamination

Concerning the 8 pole/72 stator slots design, the literature suggests to use 58 rotor slots, this solution being a well-consolidated stator/rotor slot combination.

With respect to the rotor slot shape, open and closed design is possible, depending on the compromise between electromagnetic and mechanical aspects.

On one hand, open slots allow a substantial reduction of the rotor leakage inductance with the possibility to increase the constant power range speed regulation due to an increase of maximum torque capability [53]. At the design stage, the reduction in the rotor leakage reactance has been evaluated by 2D FEM, to be in the range of 20%. In Fig. 4.2.1.2 and in Fig. 4.2.1.3 are respectively shown the open rotor slot and closed rotor slot flux density distributions obtained by the FEM analyses as well as the rotor slot design details.

On the other hand, closed slots mean higher rotor leakage inductance allowing of better current filtering in presence of inverter supply; furthermore, this solution mitigates the mechanical stability problems due to very high peripheral speed of the rotor and it allows improving the die casting process for squirrel cage production in industrial electrical machines.

From the mechanical robustness point of view, the rotor end-rings have been sized with the aim at preventing the squirrel cage centrifugation: the axial dimensions of the rings are thinner than those of conventional industrial machines, so the section is developed radially until the shaft diameter is reached, as shown in Fig. 4.2.1.4.

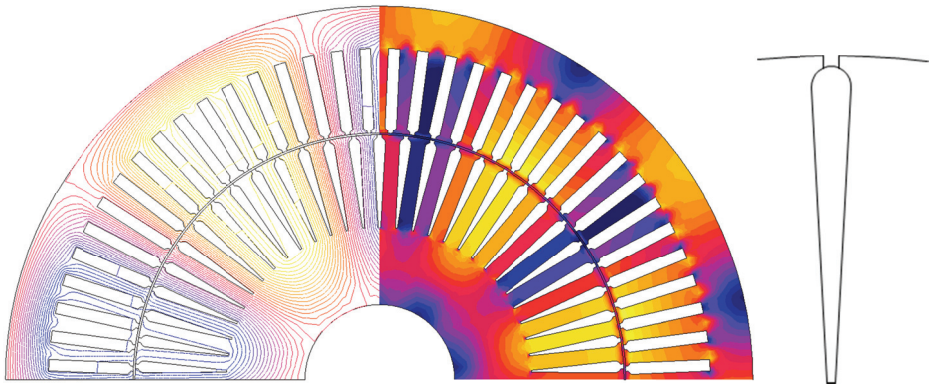

Fig. 4.2.1.2: Open rotor slot: (a) FEM no-load flux density distribution; (b) Rotor slot design detail.

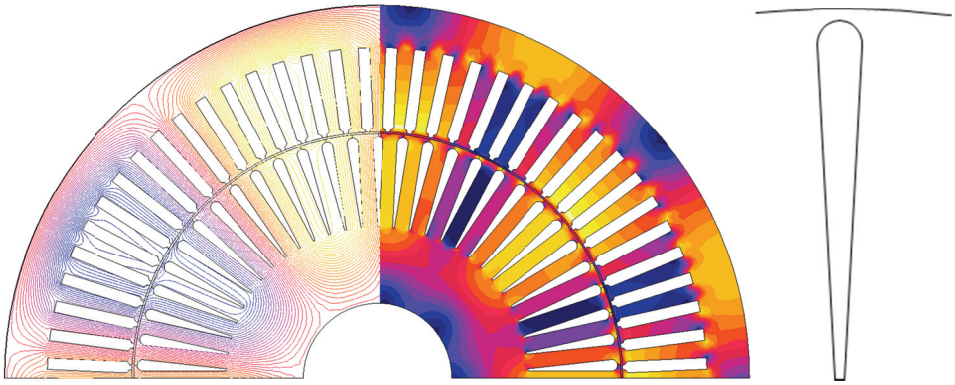

Fig. 4.2.1.3: Closed rotor slot: (a) FEM no-load flux density distribution; (b) Rotor slot design detail.

FEM spin stress analysis confirmed that the centrifugation of the cage is avoided and at the maximum rotational speed, the radial deformations of the rotor structure are compatible with the very thin airgap length.

The rotor slot shape has been designed for copper bar squirrel cage in order reduce the slip and increase the overall efficiency. Due to the small rotor diameter the rotor slots are designed thin and deep with triangular shape, leading to some manufacturing problems concerning the rotor laminations and copper bars (mechanical tolerances).

With the aim to investigate the maximization of the electromagnetic performance according to the limits imposed by the mechanical stress of the rotating parts, two prototypes having open and closed rotor slots have been designed and produced.

In Fig. 4.2.1.5 are shown the dimensions of the designed open and closed rotor slots, respectively while the two rotors during the assembly stage are shown in Fig. 4.2.1.6.

Fig. 4.2.1.4. Short circuit rings and rotor bar.

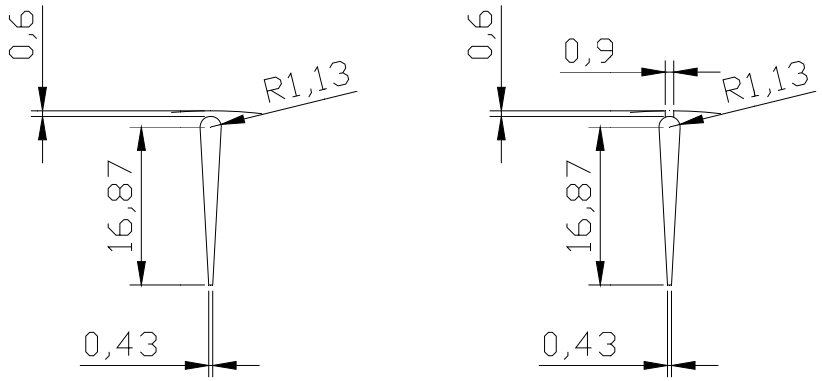

Fig. 4.2.1.5 Open and closed rotor slot shape

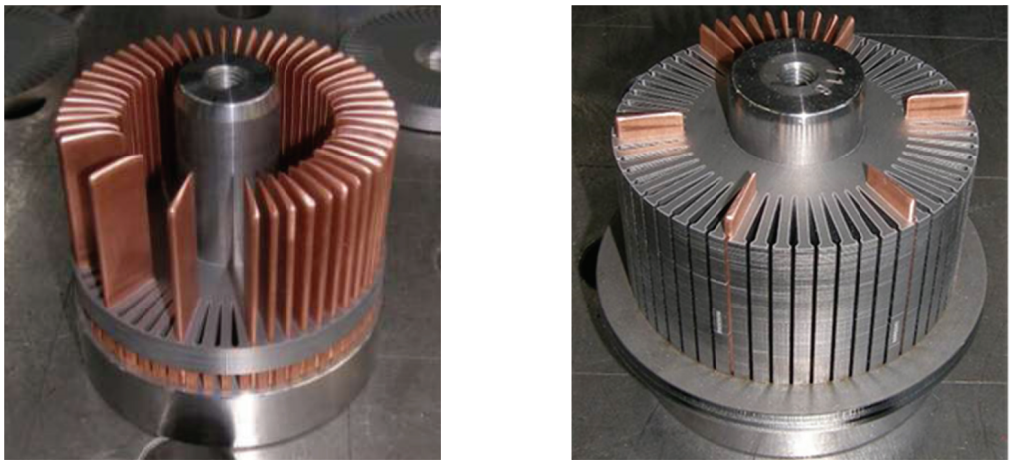

(a) (b)

Fig. 4.2.1.6. Rotors during the assembly stage: a) closed slots; b) open slots.

4.2.2. Stator winding

The design of the stator winding is considered one of the most important aspects to achieve greater level of performance while maintaining acceptable reliability. This general statement became more important when dealing with electrical machine for traction. In fact, the need to save weight and space and ever improving performance leads to drive the machine with high peak current density: it not uncommon for electrical machine for traction to be have peak stator winding current densities of 30 A/mm^2 or greater. Therefore, the proper winding configuration as well the conductor selection is essential to ensure a fully achievement of performance and reliability.

The use of stranded wires or rectangular conductors for stator winding leads to different electromagnetic and thermal behavior; in this section, the two topologies are initially discussed. Generally speaking, winding with rectangular wire section (also called bar wound, form-wound, hair pin etc.) has some advantages with respect to stranded winding type. The rectangular conductor can fill much better the volume of the slot with respect to stranded solution, in particular in the stator tooth opening. This leads to reduce the copper losses and then improving the efficiency at low speed. In addition, with a same sized machine is possible to increase the current density and deliver more peak power. Another advantage related bar winding is the larger contact surface between copper and the surrounding iron and air that allows obtaining lower winding thermal resistance. Furthermore, thanks to an increased thermal capacitance of the winding, due to high fill factor, bar windings offer benefits also from the thermal transient point of view. Exploiting the thermal capacitance of the winding it is possible to cope with the short overload operating point such as engine cranking, boosting or regenerative breaking.

Nevertheless, due to the large cross section of the conductors, bar winding topology are very sensitive to skin and proximity effect involved by the armature reaction at high supply frequency. Therefore, the additional Joule losses in the winding must be carefully taken into account during the design stage and, if needed, solutions aimed to mitigate the phenomena such as multi-layer winding must be adopted.

A. Preliminary Winding Thermal Assessment

In order to preliminarily evaluate the electrical machine thermal capability, the impact of the fill factor on the phase ohmic resistance, on the winding thermal

capacitance and on the thermal resistance between winding and iron lamination has been evaluated in accordance to the methodology presented in [XVII].

It is worth to notice that the initial winding temperature rise is linear since heat transfer is by conduction only and heat is stored in the conductor thermal mass as adiabatic process [79]. Therefore, it is possible to evaluate the winding temperature rise during overload by knowing the thermal energy dissipated and the thermal capacitance in which it is stored.

If the characteristics of the winding including the end-winding length are known, the phase ohmic resistance as well as the winding thermal capacitance can be computed with certain accuracy.

In addition, since the reference load profile (see Fig. 3.2.3) and the stator phase current necessary for deliver the required torque (equation 4.39) are also known, it is possible to estimate the energy stored in the winding.

The phase ohmic resistance has been evaluated with reference to the procedure described in section 5.1.1 of the next chapter. Concerning the winding thermal capacitance, its value includes the thermal capacitance of the conductor as well as the thermal capacitance of the insulation system [XIX] as expressed by (4.2.1)

$$C_{wind} = C_{cu} + C_{ins} \qquad (4.2.1)$$

C_{cu} can be computed by using (4.2.2)

$$C_{cu} = V_{cu} sw_{cu} c_{cu} = m c_{cu} \qquad (4.2.2)$$

Where V is the volume, sw is the specific weight, m is the weight and c is the specific heat, all referred to the copper.

The insulation system thermal capacitance, C_{ins}, can only be roughly estimated due to a complex multi-material system. Using an average specific quantity can mitigate the lack of information concerning the material characteristic and manufacturing process Thus, referring to the values presented in [XI], the insulation system equivalent specific weight has been considered equal to 1300 kg/m^3 while the equivalent specific heat equal to 1000 J/(kg K).

$$C_{ins} = V_{ins} sw_{ins} c_{ins} = m c_{ins} \qquad (4.2.3)$$

Finally, the thermal resistance has been evaluated according the procedure proposed in [61] by means the equation (4.2.4)

$$R_{cu-ir} = \frac{(1-ff)A_{slot}}{k_{cu-ir}N_s l_{slot}^2 l_{core}} \quad (4.2.4)$$

Where, *ff* is the fill factor, A_{slot} is the useful area of the slot, l_{slot} is the slot perimeter, l_{core} is the axial length and $k_{cu\text{-}ir}$ is the equivalent thermal conductivity.

In Table V are reported the computed values for both, bar and stranded conductor winding. The fill factor with bar conductor is equal to 0.6, this is obtained considering a 4-layer winding having one rectangular bar (1.6x3.55 mm) per layer, as sketched in Fig. 4.2.2.2. In the 2-layer winding stranded conductor case, the fill factor is equal to 0.3 and it is obtained accommodating 9 parallel wires/layer of 0.5 mm diameter. It must be noticed that the end-windings are included in the computations; in the case under study the end-winding thermal capacitance amounts to 60-70% of the total winding thermal capacitance.

Short-time thermal simulations of the stator winding have been performed considering adiabatic process, so the winding temperature can be expressed as $T_{wind}(t) = (P_{Joule}t)/C_{wind}$.

Fig. 4.2.2.1 shows the over-temperature comparison between the two winding topology while powered with a heat source of 4.5 kW (Joule losses in the winding during overload condition). It can be noticed that after only 5 seconds the over-temperature of the stranded winding is 10 °C higher than bar winding one. This difference can be relevant to remain within the class of insulation thermal limit during overload condition.

TABLE V
WINDING FEATURES

	Fill factor	Phase Resistance (mΩ)	Thermal capacitance (J/°C)	Thermal resistance (°C/W)
Bar	0.6	6.5	1370	0.068
Stranded	0.3	11	825	0.077

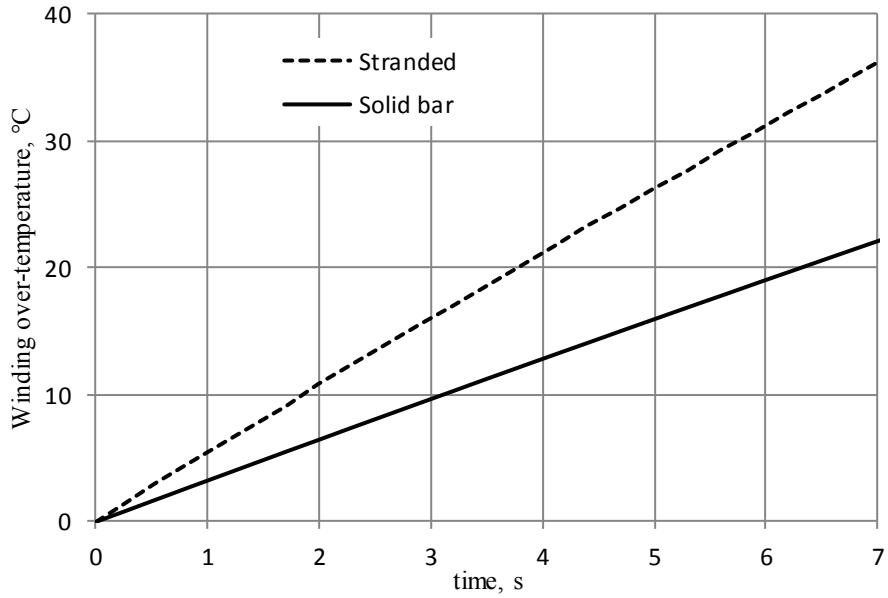

Fig. 4.2.2.1 Predicted over-temperature of solid bar and stranded stator winding during short time transient.

B. Additional Joule losses

Since the maximum supply frequency of the prototype is 1300 Hz, the additional Joule losses in the stator winding have been carefully accounted during the design stage. The adopted calculation method makes use of an *ac* resistance factor, *kr*, to evaluate the *ac* losses [47]. This factor is defined as the ratio between the *ac* and *dc* resistance values, given by (4.2.5):

$$k_r = \frac{R_{ac}}{R_{dc}} = \varphi(\xi) + \psi(\xi)\frac{(m^2-1)}{3} \tag{4.2.5}$$

where,

$$\xi = h\sqrt{\pi f \frac{\pi\mu_0}{\rho}\frac{b_c}{b}} \tag{4.2.6}$$

$$\varphi = \xi\frac{\sinh(2\xi)+\sin(2\xi)}{\cosh(\xi)-\cos(\xi)} \tag{4.2.7}$$

$$\psi = 2\xi\frac{\sinh(2\xi)-\sin(2\xi)}{\cosh(\xi)+\cos(\xi)} \tag{4.2.8}$$

and ρ is the resistivity of the winding material (copper in the case under study). As depicted in Fig. 4.2.2.2, m is the number of conductor layers, h is the height of the elementary conductor, b_c is the width of the conductor and b is the slot width.

The proximity and skin effects have been computed for the copper embedded in the stator slots only, neglecting their contribution in the end-windings.

For comparison, the analytical calculation of *ac* losses in the stator winding has been performed for both, the conventional double layer winding solution and for four layer winding solution (two bar conductor per slot-layer).

In terms of *ac* phase resistance, Fig. 4.2.2.3 shows the superiority of 4-conductor layers with respect to the 2-layer solution in terms of *ac* resistance factor for the entire frequency range.

The ratio between *ac* and *dc* resistance with respect to current and frequency at 200 °C obtained by 2D FEM analyses of the four-layer layout is shown in Fig 4.2.2.4. The results show that the ratio is decreasing when the current increases; this phenomenon is due to the progressive iron saturation of the stator and rotor teeth that reduces the leakage flux in the slots. To avoid the complexity for an accurate 3D FEM modeling of the end-winding (see Fig. 4.2.2.5), it has been preferred to directly validate the computed k_r coefficient by means of measurements, as presented in the next section.

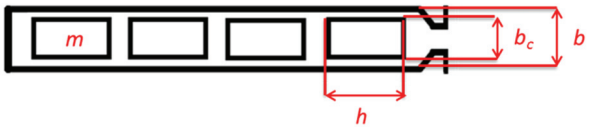

Fig. 4.2.2.2. Conductors arrangement in the stator slot.

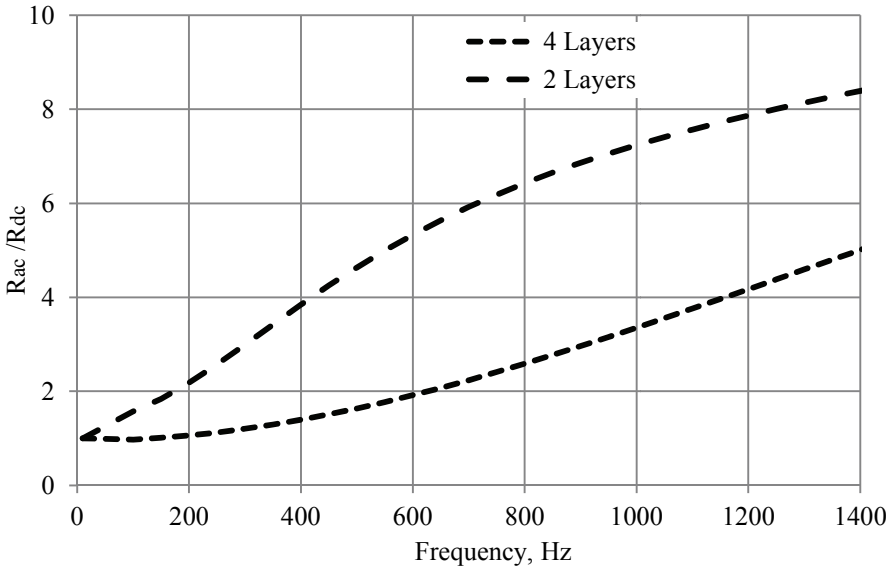

Fig. 4.2.2.3. Ratio between *ac* to *dc* resistance respect to frequency at 25 °C.

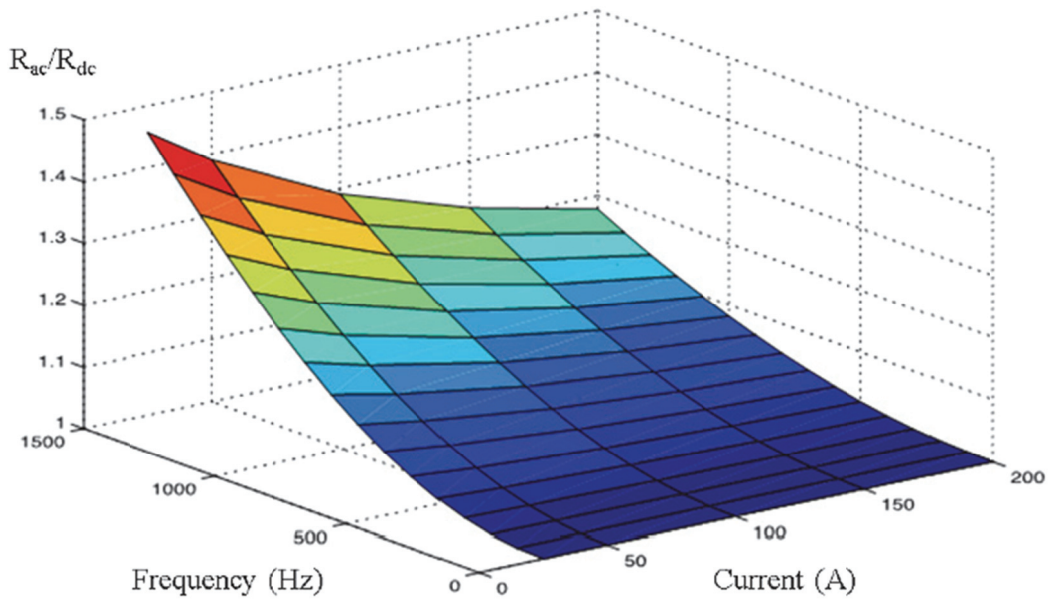

Fig. 4.2.2.4. Ratio between R_{ac} and R_{dc} of one layer as function of the frequency and current at 200 °C.

Fig. 4.2.2.5. Detail of the stator end-turn connections.

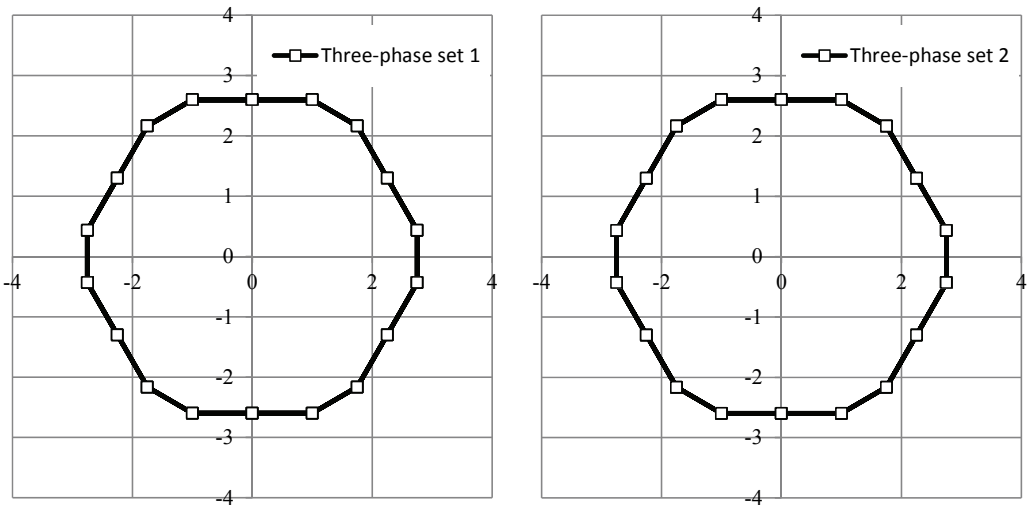

Fig. 4.2.2.6. Goerges polygon of the two three-phase set.

On the basis of these considerations, it can be stated that quadruple layer bar winding topology represents a better trade-off between electromagnetic and thermal behavior with respect to both stranded and double layer massive bar solutions. The prototype adopts a quadruple-layer double three-phase stator winding, having 72 slots, 8 poles and one slot pitch shortening; the scheme is reported in Fig. 4.2.2.7. To further mitigate the phenomenon, the semi-open stator slot shown in Fig. 4.2.1.2 has been used and the winding bars have been inserted from the hand side instead the slot opening.

Fig. 4.2.2.6 shows the Goerges diagram for unitary current value of the adopted winding configuration (see Fig 4.2.2.7). It can be noticed the correspondence between the two three-phase set; this finding confirms that the proposed double three-phase configuration can be analytically represented as a conventional three-phase system.

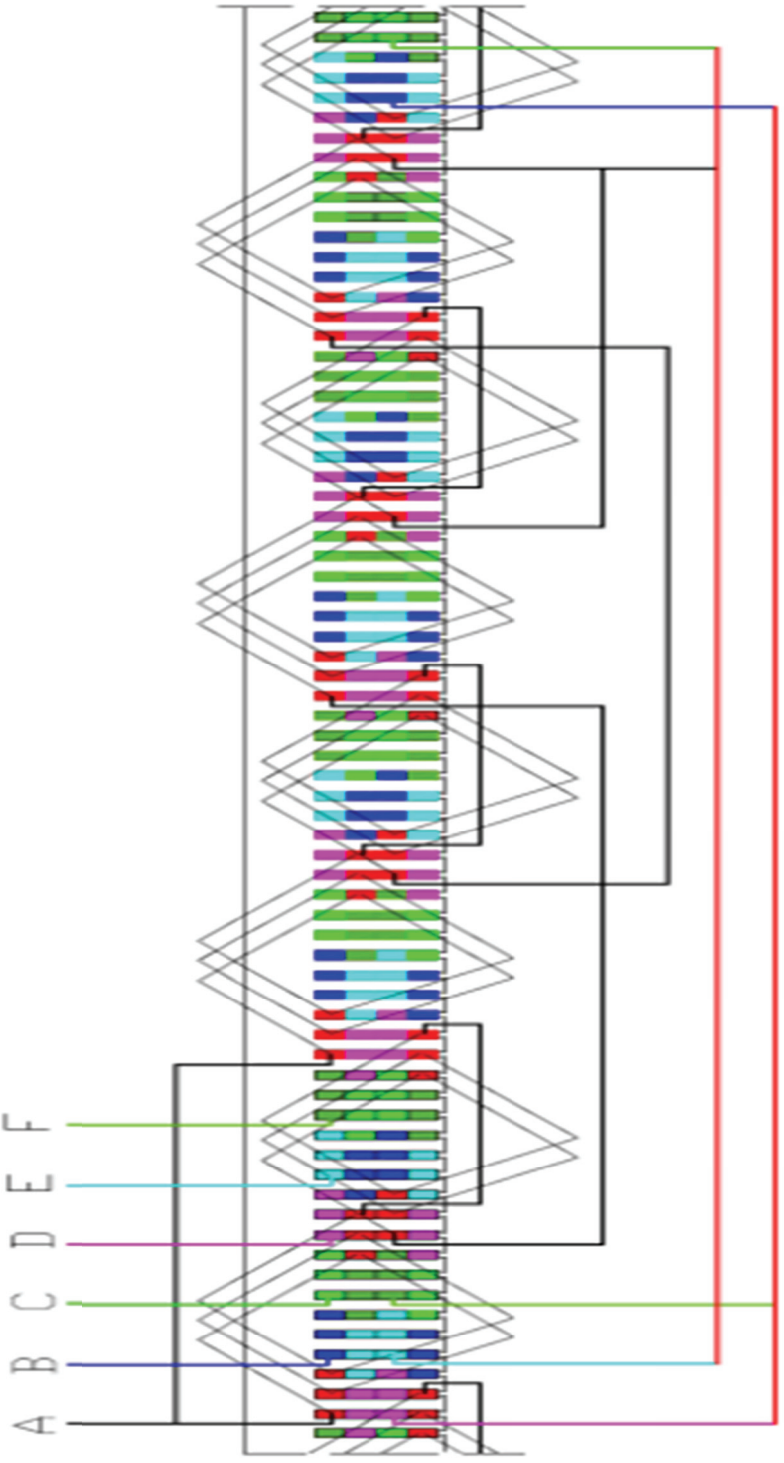

Fig. 4.2.2.7. Double three-phase stator winding layout, 4 layers, 72 slots 8 poles.

5. Simulations and Experimental Results

5.1. Single-phase Equivalent Circuit

Once the electromagnetic design has been successfully completed, the machine performance in terms of torque and current characteristics must be evaluated.

The fastest and viable approach to perform this validation of poly-phase machine is to use equivalent circuits [58]. In particular, the IEEE standard is referred to conventional three-phase machine but the application of equivalent circuit can be extended to multi-phase machine as well. In this regards, in literature can be find several examples of its application for different multi-phase winding topology, symmetrical as well as asymmetrical [85]-[87]. The performance of the investigated double-three phase machine is computed by using the single-phase equivalent circuit reported in Fig. 5.1.1. The power computation has been done considering the number of phases equal to six.

It is important to highlight that the magnetizing inductance, the rotor leakage inductance and the rotor resistance are non-linear component. In particular, the magnetizing inductance has to be determined taking into account the lamination magnetic saturation while the rotor resistance account for the skin effect of the rotor bars. The solution of the non-linear equivalent circuit allows predicting the machine performance such as torque, power, currents, losses, etc. The additional losses are not considered in the circuit however it is possible to include an equivalent resistance that accounts for additional losses in the machine power balance. The parameters of the equivalent circuit of the designed starter-generator are determined from geometrical data of the machine using magnetic circuit analysis. In [55][56] is presented the complete collection of the used equations and algorithms for the computation of the equivalent circuit parameters starting from the lamination and winding design. Hereafter are summarized the main formulation used for the parameters evaluation while the required geometrical data for the parameters computation are:

- Stator and rotor diameters (inner and outer)
- Axial core length
- Stator and rotor slot number
- Stator and rotor slot geometrical shapes

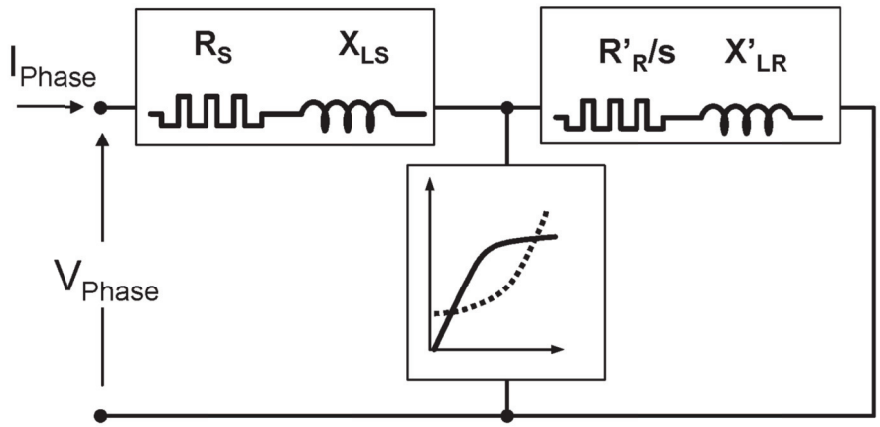

Fig. 5.1.1. Induction motor single-phase equivalent circuit.

While the needed electrical data are:

- Pole number
- Number of conductor in series per phase
- Winding pitch
- Conductor section areas
- Skewing pitch of the rotor slots

5.1.1. Stator and rotor resistance

Stator winding resistance

The stator winding resistance can be evaluated by the following equation (5.1.1):

$$R_s = \rho \frac{(Z_{ph}/2) L_{ave\_turn}}{A_{wire}} \quad (5.1.1)$$

Where ρ is the conductor material resistivity, A_{wire} is the cross section area of the equivalent wire and L_{ave_turn} is the average turn length. The latter is the addition of two contributions: the turn accommodate into the slots and the end-winding connection (5.1.2)

$$L_{ave\_turn} = 2(L_{core} + L_{ew}) \quad (5.1.2)$$

$$L_{ew} = K_{ew} \left(1 - \frac{n_r N_{pole}}{N_{ss}}\right) \frac{\pi}{N_{pole}} (D_{is} + h_s) \quad (5.1.3)$$

K_{ew} is the end winding shape coefficient and its typical value is in the range of 1.6-2.2.

Rotor winding resistance

The phase resistance of the cage is referred to one bar and two adjacent ring sectors assuming that the phase rotor number equal to the bar number, see Fig. 5.1.

The resistance of a single bar can be computed by (5.1.4)

$$R_b = K_r \rho \frac{L_{bar}}{A_{bar}} \tag{5.1.4}$$

While the resistance contribution of end-ring can be computed according to (5.1.5)

$$R_a = \rho \frac{\pi D_a}{A_a} \tag{5.1.5}$$

In the equations K_r is the coefficient that account for the skin effect; in case of computation of the *dc* value the coefficient is set to one.

According to the cage rotor Joule losses and from the equations previously described is possible to compute the equivalent rotor phase resistance (5.1.6)

$$R_r = R_b + \frac{2\,R_a}{4N_{bars} sin^2\left(\frac{\beta_r}{2}\right)} \tag{5.1.6}$$

The obtained resistance is the actual rotor cage resistance, in order to refer the value to the stator it should be moved by using (5.1.7)

$$K_{rs} = \frac{3}{N_{bars}} (Z_{ph} K_{w,1})^2 \tag{5.1.7}$$

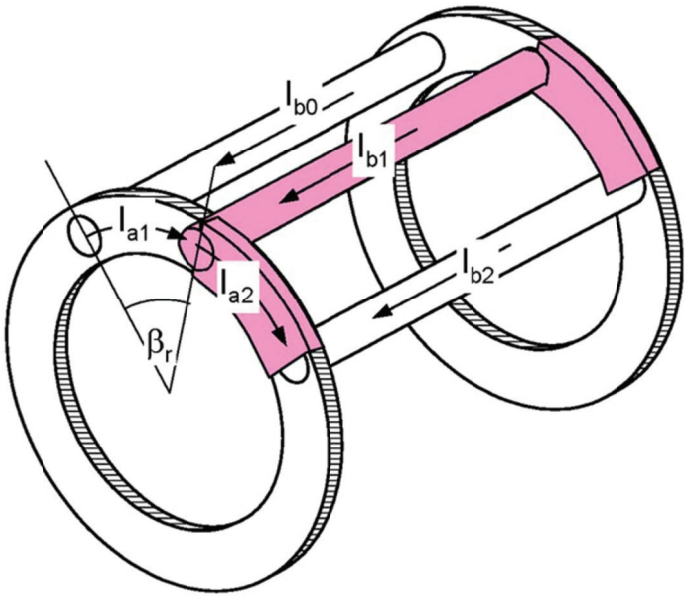

Fig. 5.1 Rotor cage and related bar and ring current

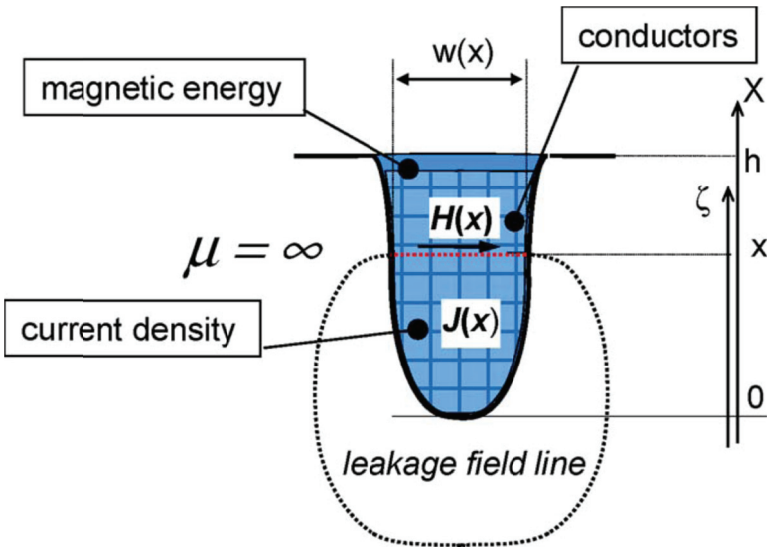

Fig. 5.2 Magnetic field distribution in the slot

5.1.2. Leakage inductances

The slot leakage inductance can be evaluated on the basis of the magnetic energy stored in the slot defined by (5.1.8)

$$E_w = \frac{1}{2}\lambda_{slot} L_{slot} I_{slot}^2 \tag{5.1.8}$$

Where λ_{slot} is the slot leakage coefficient, L_{slot} the length of the winding part inside the slot and I_{slot} is the total current in the slot.

Assuming infinite iron permeability and magnetic field lines parallel into the slot the magnetic energy stored in the slot can be calculated by

$$E_w = \frac{1}{2}\mu_0 L_{slot} \int_0^h H(x)^2 \cdot w(x) dx \tag{5.1.9}$$

With reference to Fig. 5.2, the magnetic field at the x-coordinate can be computed by

$$H(x) = \frac{\int_0^x J(\zeta) \cdot w(\zeta)}{x(x)} \tag{5.1.10}$$

While the slot current is defined by

$$I_{slot} = \int_0^h J(x) \cdot w(x) dx \tag{5.1.11}$$

Consequently, the slot leakage coefficient results

$$\lambda_{slot} = \frac{\mu_0 \int_0^h H(x)^2 \cdot w(x) \cdot dx}{I_{slot}^2} \tag{5.1.12}$$

Stator slot leakage inductance: full pitch

The phase slot leakage inductance for a full pitch winding can be obtained by (5.1.13)

$$L_{slot\_leakage} = \frac{Z_{ph}^2}{N_{pole}q}\lambda_{slot}L_{slot} \quad (5.1.13)$$

Stator slot leakage inductance: shortened pitch

In case of double layer shortened pitch winding, conductors of different phases are present in some slots. The magnetic energy stored in a slot can be computed according to the following equation

$$E_w = \frac{1}{2}\mu_0 L_{slot}\int_0^h (H_1(x) + H_2(x))^2 \cdot w(x)dx \quad (5.1.14)$$

Where $H_1(x)$ and $H_1(x)$ are the magnetic field produced by the current of layer 1 and layer 2, respectively. The magnetic energy in the slots can be written as the three contributions

$$E_{w,1} = \frac{1}{2}\lambda_{slot,1}L_{slot}I_{layer,1}^2$$

$$E_{w,2} = \frac{1}{2}\lambda_{slot,2}L_{slot}I_{layer,2}^2$$

$$E_{w,1} = \frac{1}{2}\lambda_{slot,12}L_{slot}I_{layer,1}I_{layer,2}$$

If the two layers have the same number of conductors per slot, the leakage inductance can be evaluated according to

$$L_{slot\_leakage} = \frac{Z_{ph}^2}{N_{pole}q}\frac{\lambda_{slot,1}+\lambda_{slot,2}+(2-\frac{n_r}{q})\lambda_{slot,12}}{4}L_{slot} \quad (5.1.15)$$

Rotor slot leakage inductance

The rotor leakage inductance can be easily evaluated by (5.1.16) since the rotor phase corresponds to a single bar of the squirrel cage,

$$L_{slot\_leakage} = \lambda_{slot}L_{slot} \quad (5.1.16)$$

End-winding leakage inductance

The computation of end-winding leakage inductance component is not a simple task due to their complex geometry. However, the linked flux with the end-winding of a single turn can be computed using the following approximated equation (5.1.17)

$$\phi_H \cong \mu_0 \frac{I_h}{2\pi} log\left(\frac{L_h}{p_h}\right) L_h \quad (5.1.17)$$

Where I_h is the end winding current, L_h is the end winding length and p_h is the half perimeter of the end winding cross section.

Defining the following quantities

$Z_L = \frac{Z_{ph}}{2qN_{pole}}$ number of layer conductor in series

$Z_h = qZ_L$ number of end-winding conductor in series

The total end-winding phase leakage inductance has to be computed by summing the contributions of all the phase taking into account the coupling with other phases. As a consequence, for the considered winding type the end-winding leakage inductance is

$$L_{phase\_endwinding} = \frac{\mu_0}{2\pi} \frac{{Z_{ph}}^2}{2N_{pole}} log\left(\frac{L_h}{p_h}\right) \frac{4}{3} L_h$$

Airgap leakage inductance

The airgap leakage inductance for both, stator and rotor component is presented in this section.

Stator leakage inductance

The harmonic decomposition of M.M.F. along the airgap generates by three-phase sinusoidal current is given by (5.1.18)

$$A_3(\alpha, t) = \frac{3}{2} I_{max} \sum_{h=6k+1} \frac{Z_{ph} K_{w,h}}{h\pi N_{pole}/2} \sin(hp\alpha - \omega t) \quad (5.1.18)$$

Neglecting the iron influence, the whole M.M.F. distribution drop along the airgap and the M.M.F. amplitude for the *h*th-order harmonics results in

$$A_h = \frac{3}{2} \frac{Z_{ph} K_{w,h}}{h\pi N_{pole}/2} I_{max} \quad (5.1.19)$$

Consequently, the flux density amplitude for the *h*th-order harmonics

$$B_h(\alpha, t) = \frac{3}{2} \frac{Z_{ph} K_{w,h}}{h\pi N_{pole}/2 K_{cs,h} K_{c,aveR} h_{airgap}} I_{max} \quad (5.1.20)$$

Where h_{airgap} is the airgap thickness, $k_{cs,h}$ is the harmonic Carter coefficient for the stator *h*th field harmonic, $K_{c,aveR}$ is the average Carter coefficient for the rotor.

The main flux liked to the stator winding can be computed from the sum of all the harmonic contributions.

$$\Lambda_h = \frac{3}{2}\left(\frac{Z_{ph}K_{w,h}}{h\pi N_{pole}/2}\right)^2 \frac{\mu_0 \pi R_{airgap} L_{slot}}{K_{cs,h}K_{c,aveR}h_{airgap}} I_{max} \quad (5.1.21)$$

As a consequence, the main magnetizing inductance results:

$$\mathrm{L}_{main} = \sum_h \frac{3}{2}\left(\frac{Z_{ph}K_{w,h}}{h\pi N_{pole}/2}\right)^2 \frac{\mu_0 \pi R_{airgap} L_{slot}}{K_{cs,h}K_{c,aveR}h_{airgap}}$$

Since only the fundamental flux wave rotates at the correct speed and only this component act on the electromechanical energy conversion, the higher flux component of high order is considered as leakage component.

Therefore, the airgap-leakage inductance is defined as (5.1.22)

$$L_{leakage\_airgap} = L_{m,main} - L_{m,fund} \quad (5.1.22)$$

Approximating the harmonic Carter coefficient through the average Carter coefficient $K_{cs,h}K_{c,aveR} \approx K_{c,aveSR}$ the following equations can be obtained for the main and fundamental magnetizing inductance.

$$\mathrm{L}_{main} = \mathrm{L}_{main} = \left(\frac{Z_{ph}}{N_{pole}/2}\right)^2 \frac{20q^3+2q\left(2-3n_r^2\right)+n_r(n_r^2-1)}{144q^3} \frac{\mu_0 \pi R_{airgap} L_{slot}}{K_{c,aveSR}h_{airgap}} \quad (5.1.23)$$

Rotor airgap Leakage Inductance

The rotor leakage inductance of the rotor is defined as the difference between the main and fundamental magnetizing inductances.

The former is defined as the ratio between the E.M.F induced in a bar and the time derivative of the bar current

$$L_{m,main} = \frac{E_{bar}}{dI_{bar}/dt} \quad (5.1.24)$$

While the main magnetizing cage inductance is

$$L_{m,main} = \mu_0 \frac{N_{bars}}{2\pi} \frac{R_{airgap} L_{slot}}{h_{airgap}} \sum_h \left(\frac{1}{h^2 K_{C,aveS} K_{Cr,h}}\right) \quad (5.1.25)$$

Where $h=k\,N_{bars}+N_{pole}/2$

The fundamental magnetizing cage inductance is

$$L_{m,main} = \mu_0 \frac{N_{bars}}{2\pi} \frac{R_{airgap} L_{slot}}{K_{C,ave} K_{Cr,1} h_{airgap}} \quad (5.1.26)$$

The rotor cage airgap leakage inductance can be evaluated by

$$L_{leakage\_airgap} = L_{m,main} - L_{m,fund} \quad (5.1.27)$$

Even in this case if the harmonic Carter coefficient is approximated through the average Carter coefficient $K_{cs,h}K_{c,aveR} \approx K_{c,aveSR}$ the equation results

$$L_{m,main} = \mu_0 \frac{N_{bars}}{2\pi} \frac{R_{airgap} L_{slot}}{K_{C,aveSR} h_{airgap}} \left(\frac{\pi}{N_{bars} \sin\left(\frac{N_{pole}}{2} \frac{\pi}{N_{bars}}\right)} \right)^2 \quad (5.1.28)$$

5.1.3. Skin effect

The current density in slot-bound conductors is not uniform in presence of *ac* supply. This effect depends on the actual frequency of rotor bar currents, and it leads to an increase of the equivalent bar resistance and a reduction of the equivalent leakage bar reactance. Typically, these effects are taken into account introducing the corrective coefficient to be applied at *dc* value of the resistance, K_R, and inductance, K_L.

For the computation of the corrective coefficient it has been used the algorithm proposed in [56] however, a brief description of the method is reported in the following.

The procedure is based on the following hypothesis:

- Ideal iron (infinite permeability and no losses)
- Field lines parallel in the slot
- Slot subdivided into N thin layers

When sinusoidal voltage is applied to the bar, it is equally distributed to all conductors. For a generic *k*th layer, the electromagnetic phasor equations are:

$$\bar{V} = R_k \Delta\bar{I_k} + j\omega_e \overline{\Lambda_k} \quad (5.1.29)$$

$$\overline{\Lambda_k} = \sum_{j=1}^{N} M_{kj} \Delta\bar{I_J} \quad (5.1.30)$$

In order to compute the bar layer current $\Delta\bar{I_k}$ it is necessary to determine a general formulation for the M_{jk} coefficient. The mutual inductance between *k*th and *j*th layer has the following peculiarities:

- M_{jk} is eual to M_{kj} for the physics of the problem.
- If $j<k$ the *j*th-layer linked flux due to the *k*th-layer current is invariant with the position of the *j*th-layer. This means that $M_{jk}=M_{kk}$ if $j<k$

Consequently, is possible to find the following phasor relation:

$$\Delta\bar{I_k} = \frac{\omega_k}{\omega_{k-1}} \Delta\overline{I_{k-1}} + j\delta^*(\Delta\bar{I_1} + \Delta\bar{I_2} + \cdots + \Delta\overline{I_{k-1}}) \quad (5.1.31)$$

where

$$\delta^* = \omega_e \left(\frac{\mu_0}{\rho}\right)\left(\frac{h^2}{N^2}\right) \quad (5.1.32)$$

while $\omega_e = 2\pi f$ is the electrical pulsation of the current and ρ is the conductor resistivity referred to the actual temperature.

From equation (5.1.31) is possible to note that the current in a layer depends on the total current under the layer itself. This means that, if the current in the first layer is known, as amplitude and phase, all the other layer currents can be calculated with a recursive procedure. As a consequence, with the aim to evaluate the current distribution in the bar, it is possible to consider an arbitrary current in the first layer (i.e. $\Delta\bar{I} = 1 + j0\ A$). Once the layer currents are known, the correction coefficient K_R an K_L are evaluated by means:

$$K_R(f) = \frac{R_{ac}(f)}{R_{dc}} \tag{5.1.33}$$

$$K_L(f) = \frac{L_{ac}(f)}{L_{dc}} \tag{5.1.34}$$

$$R_{ac}(f) = \frac{P_J(f)}{\bar{I}^2} = \rho \frac{N}{h} \frac{\sum_{k=1}^{N} \frac{\Delta\bar{I}_k^2}{c_k}}{\bar{I}^2} \tag{5.1.35}$$

$\bar{H}_k = \frac{1}{\omega_k} \sum_{n=1}^{k} \Delta\bar{I}_n$ magnetic field in the *k*th layer

$$L_{ac}(f) = \frac{2W_m(f)}{\bar{I}^2} = \mu_0 \frac{h}{N} \frac{\sum_{k=1}^{N} \omega_k \bar{H}_k^2}{\bar{I}^2} \tag{5.1.36}$$

5.1.4. Fundamental airgap flux density determination

The determination of the fundamental airgap flux density as a function of the fundamental MMF taking into account the magnetic material non-linearity is presented in the follow.

It can be highlighted that the fundamental airgap flux density in required in order to compute the rms winding-induced EMF.

$$E_{rms} = \frac{2\pi f K_{w,1} Z_{ph} 2R_{airgap} L_{core}}{\sqrt{2} N_{pole}} B_{max,fund} \tag{5.1.37}$$

Where $K_{w,1}$ is the fundamental stator winding coefficient, and Z_{ph} is the number of stator conductors in series per phase.

In case of magnetic saturation, the airgap flux density waveform produced by the fundamental MMF is distorted. In this condition, the flux density peak value in the teeth and in the yokes does not depend on the amplitude of the fundamental airgap flux density, $B_{max,fund}$, but it depends in the actual airgap flux density $B_{max,airgap}$.

Therefore, starting from the $B_{max,airgap}$ it is possible to correctly calculate the MMF drop along the different machine parts according to the magnetic circuital rule.

Once the $B_{max,airgap}$ versus the MMF drop characteristic is known, it is possible to determine the distorted airgap flux density waveform in the airgap using a procedure similar to the one used for the evaluation of the magnetizing current in a single–phase transformer.

Finally the fundamental airgap flux density, $B_{max,fund}$, can be easily computed by a Fourier analysis. The complete procedure is deeply presented in [56].

5.2. *ac* resistance factor

To experimentally evaluate the *ac* resistance factor of the stator winding, the rotor has been removed to avoid the losses in the cage (the rotor absence has a minor impact on the stator winding losses). The test has been performed with sinusoidal current from 50 to 1400 Hz; to mitigate the temperature variation effect during the measurements, the current amplitude has been limited to 10 A. Since the rotor is taken out of the magnetic circuit and the supply voltages used for these tests are much lower than the rated voltages, it is assumed that the stator iron losses are negligible in the measurements. The electrical quantities of each phase, acquired by a high-precision power meter, have been used to compute the *ac* resistance factor using

$$k_r = \frac{P_{ac}/I_{ac}^2}{P_{dc}/I_{dc}^2} \tag{5.2.1}$$

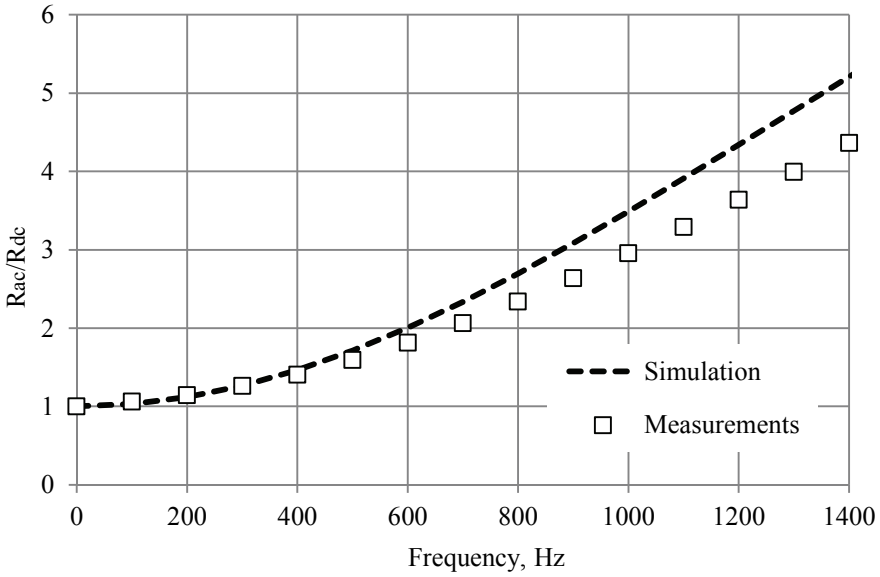

Fig. 5.2. Predicted and measured ac resistance factors.

The predicted and measured *ac* resistance factors are reported in Fig. 5.2. It can be noticed that good accuracy is achieved for a supply frequency of up to 600 Hz; for higher frequencies, the analytical computation overestimates the phenomenon.

This finding confirms what has been already presented in [57], where an improved analytical method for the estimation of *kr* in the case of high frequency is described.

5.3. Prototype parameters

The single-phase nonlinear equivalent circuit parameters have been initially computed starting from the geometrical and electrical data, following the methodologies described in the previous section for three-phase winding configuration. The nonlinear behavior of the magnetic material has been taken into account during the computation of the magnetizing reactance and the iron losses. As for the skin effect on the rotor parameters (rotor leakage inductance and rotor resistance), the recursive least squares algorithm presented in the previous section has been used. Subsequently, the computed three-phase parameters have been referred to a double-three-phase configuration by using the following relation: $R_{s\text{-}6ph} = R_{s\text{-}3ph}/2$, $R_{r\text{-}6ph} = R_{r\text{-}3ph}/2$, $R_{fe\text{-}6ph} = R_{fe\text{-}3ph}/2$, $L_{m\text{-}6ph} = L_{m\text{-}3ph}/2$, $L_{s\text{-}6ph} = L_{s\text{-}3ph}/2$, $L_{r\text{-}6ph} = L_{r\text{-}3ph}/2$. It is worth to note that also the power computation has to be scaled in order to take into account the contribution of six phases.

In addition, for each three-phase set, the electrical parameters have been measured by the well-known no-load and locked-rotor tests according to the IEEE standard procedure [58]. These tests have been performed for several supply frequencies, starting from 50 Hz up to 300 Hz. From the no-load test, the iron losses are decoupled from friction and windage losses by means power measurements at different voltage levels. Contemporary, it was also evaluated the magnetizing inductance variation as a function of the phase current.

The measured locked-rotor test resistances have been split in the stator and rotor contributions, assuming the measured stator *ac* resistance factor shown in Fig. 5.2. The computed *dc* stator resistance value has been corrected with the same measured *ac* resistance factor.

The comparison between computed and measured equivalent circuit parameters referred to a single stator unit at the supply frequency of 200 Hz is reported in Table VI. Looking at this table, it is possible to observe the satisfactory agreements between the estimations and the measurements. In addition, from the table it is possible to notice that the value of the rotor reactance of the closed rotor slot machine is higher with respect to the open rotor slot one;

TABLE VI
SINGLE PHASE EQUIVALENT CIRCUIT PARAMETERS
OF THE DOUBLE THREE-PHASE PROTOTYPES @200HZ

	unit	Open slot		Closed slot	
		computed	measured	Computed	Measured
Stator resistance	mΩ	6.5	6.5	6.5	6.2
Rotor resistance	mΩ	5.5	5.5	5.5	5.4
Stator reactance	mΩ	15.9	16.5	15.9	14.8
Rotor reactance	mΩ	12.4	16.5	28	23.6
Magnetizing reactance	mΩ	23	23.5	23	25.9
Iron resistance	Ω	11	13	11	16.4

this leads to a lower pullout torque and lower flux weakening capability of the closed rotor slot prototype.

Fig. 5.3.1 and Fig. 5.3.2 show the measured and computed no-load current versus supply voltage for closed rotor and opens rotor slot prototype, respectively; in these cases, the agreement is very good, leading to the conclusion that the saturation effects are accurately accounted for the design procedure. Still for the 200 Hz frequency values, the computed and measured locked-rotor voltage versus the phase current trends are reported in Fig. 5.3.3. To take into account the saturation phenomenon of the closing wedges of the rotor slots, the approach presented in [59] has been adopted. The saturation effect is significant in the voltage-versus-current graph of the locked-rotor test, reported in Fig. 5.3.3, where the interpolation line does not pass through the origin. Moreover, in this case, the prediction of the locked rotor test can be considered more than satisfactory.

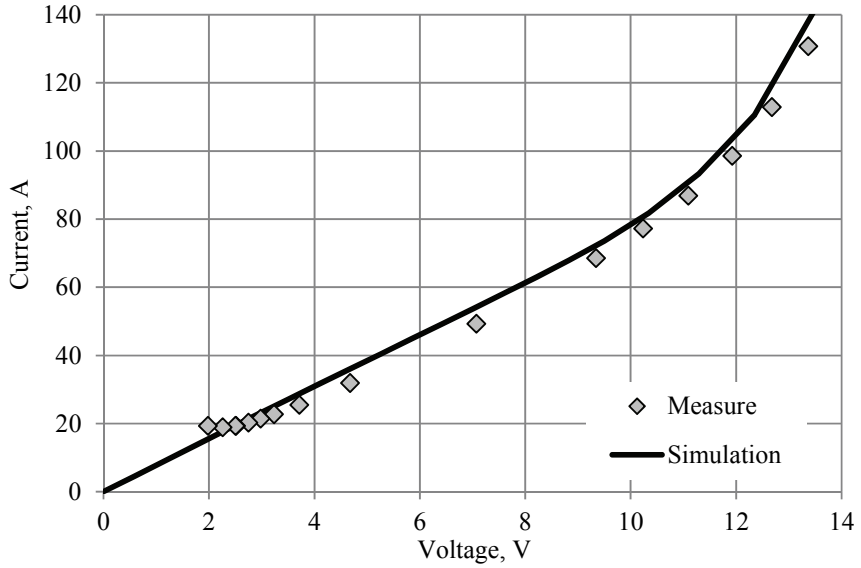

Fig. 5.3.1 Predicted and measured no-load test for closed rotor slot geometry at 200 Hz.

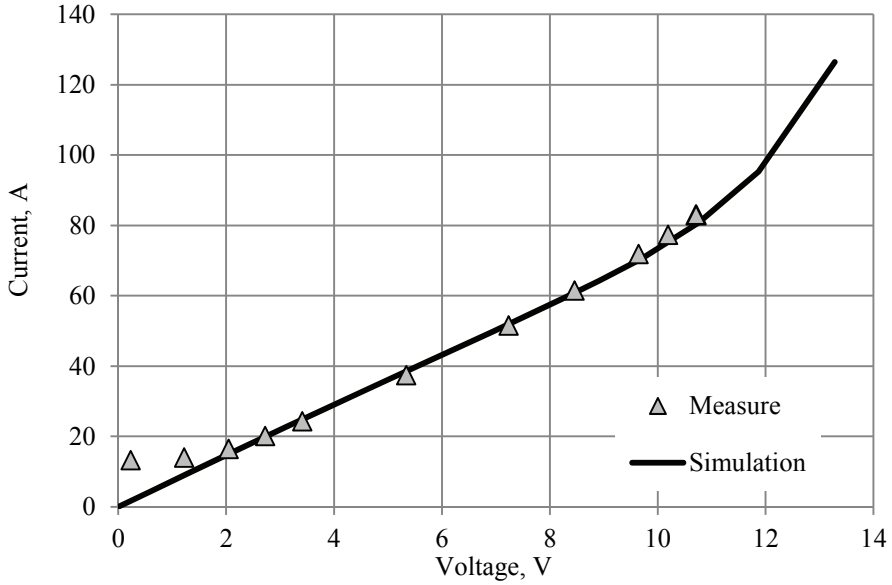

Fig. 5.3.2 Predicted and measured no-load test for open rotor slot geometry at 200 Hz.

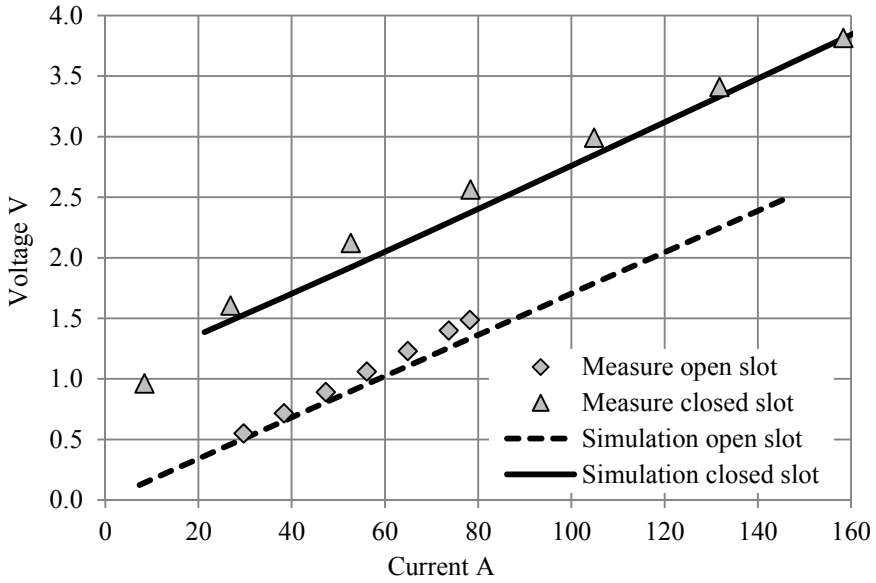

Fig. 5.3.3. Predicted and measured locked rotor test for the two prototypes at 200 Hz.

5.4. Steady-state motor prototype performance

Using the single-phase nonlinear equivalent circuit opportunely scaled up for accounting the winding configuration, the predicted steady-state performance has been computed and experimentally validated. During the load tests, all performed with water-cooling, the thermal protection of the power source limited the phase current to about 200 A. In addition, considering the frequency limitation of the power supply, it was not possible to experimentally map all the required operation points shown in Fig. 3.2.2. For these reasons, the open-loop load tests were performed in the 50–300 Hz frequency range only, respecting the voltage-to frequency ratio. Fig. 5.4.1 and Fig. 5.4.2 show the steady-state performances of the closed slot prototype at 200 and 300 Hz, respectively; once again, a good agreement between predicted and measured performance can be observed. These steady-state thermal tests allowed for verifying the water-cooling capability also in continuous service. In fact, the thermal behavior of the machine was monitored through 20 thermocouples embedded in the magnetic circuit, end winding, housing, and water duct. Focusing the attention on the 200 Hz thermal test with a load torque equal to 21 Nm and 5 l/min of water volume flow, it was possible to obtain 5.8 kW of mechanical power and 1 kW of total losses. In this condition, the stable temperature difference between winding and water was of 80 °C.

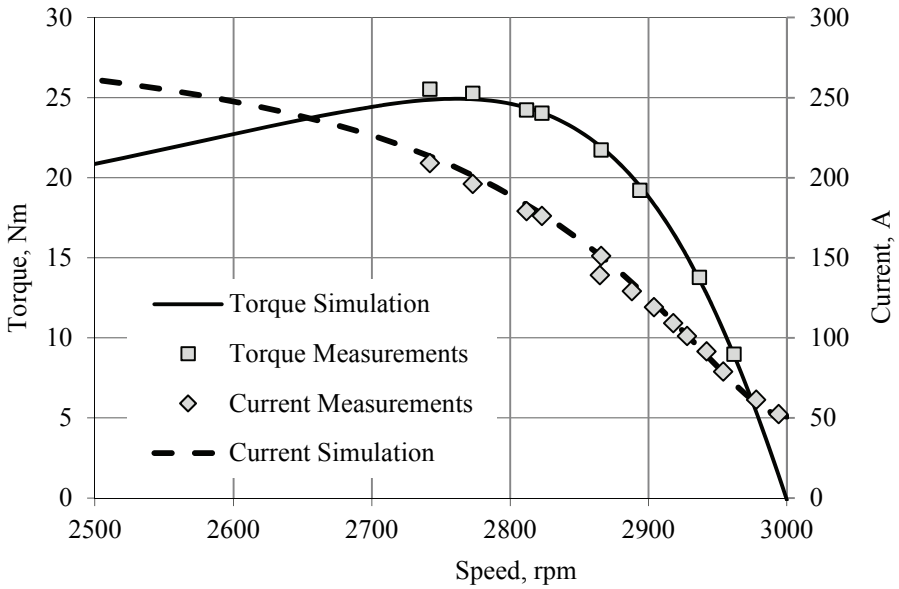

Fig. 5.4.1. Predicted and measured performance: torque and current versus speed at 200 Hz, measured stator temperature 80 °C.

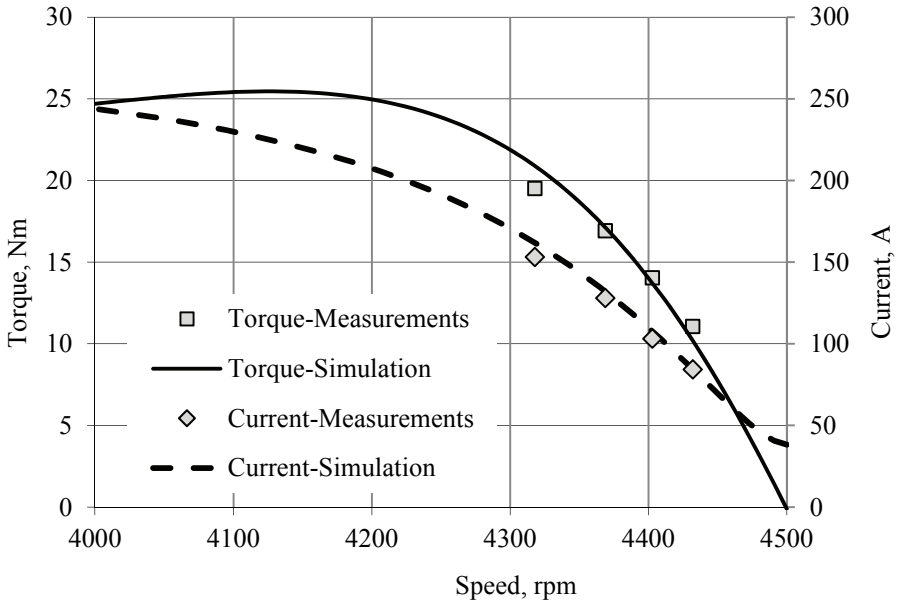

Fig. 5.4.2. Predicted and measured performance: torque and current versus speed at 300 Hz, measured stator temperature 8 °C.

5.5. Overall performance prediction

The overall performance predictions of the two prototypes have been finally computed through the single-phase equivalent circuit opportunely scaled up to account for the double three-phase winding configuration, both in motoring and generator modes. In particular, the measured parameters have been used for the prediction of the performance for frequency up to 300 Hz, whereas for higher frequency, the computed parameters have been adopted. It is important to remark that the parameters have been recomputed at the wanted frequency and winding temperature (for the stator resistance, the measured *ac* resistance factor has been still applied). This approach represents a fast solution to obtain accurate motor performance avoiding intensive FEM analysis.

Fig. 5.5.1 and Fig. 5.5.2 report the simulated performances of the two prototypes in motor mode at 150 °C winding temperature (assumed as typical working temperature); it can be noticed that the requirements are fully satisfied in the overall operating speed range. As expected, the prototype with open rotor slots has higher pullout torque due to lower rotor leakage reactance.

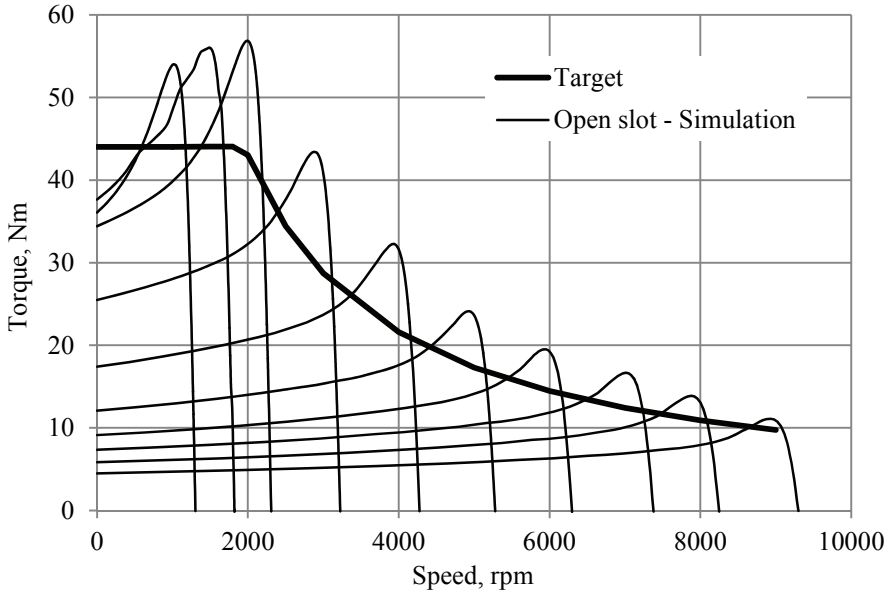

Fig. 5.5.1. Open slot prototype: predicted motor performance (stator temperature equal to 150 °C).

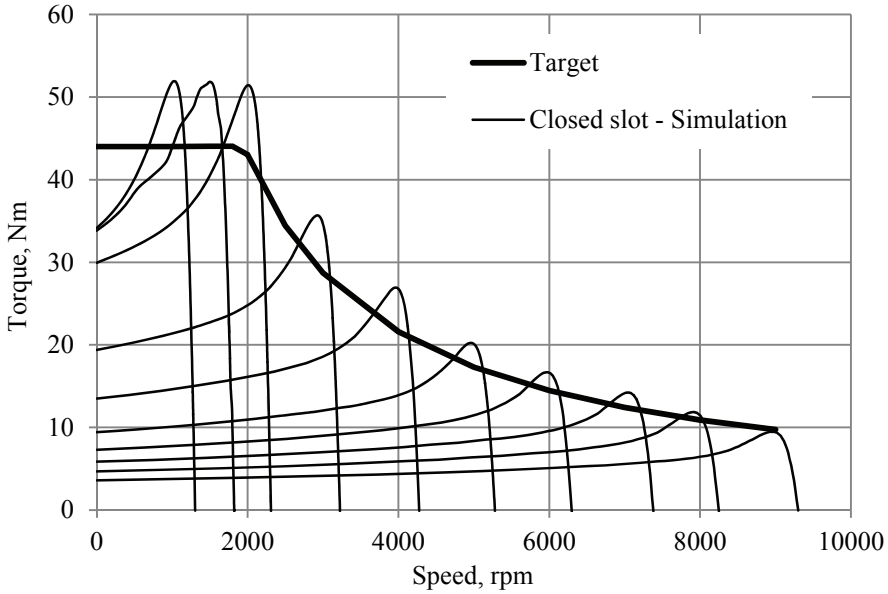

Fig. 5.5.2. Closed slot prototype: predicted motor performance (stator temperature equal to 150 °C).

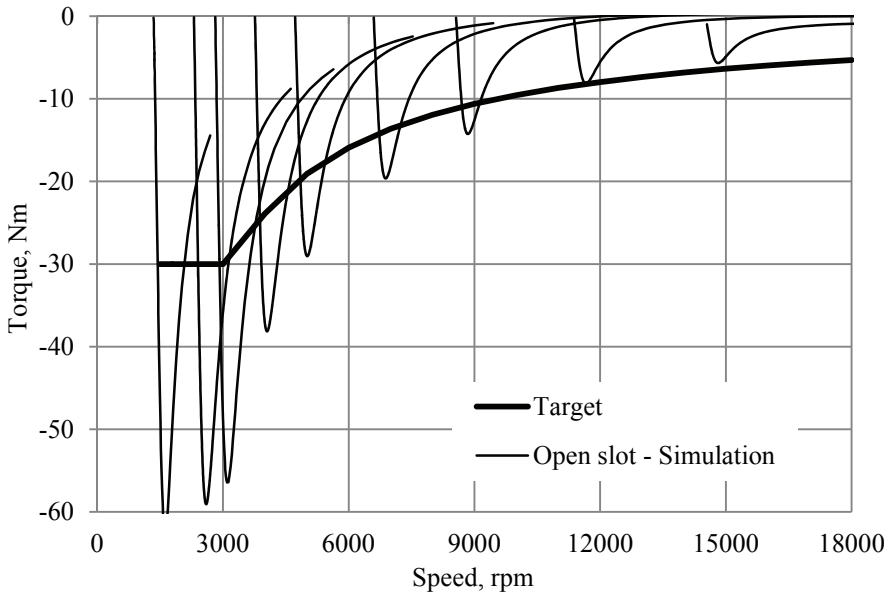

Fig. 5.5.3. Open slot prototype: predicted generator performance (stator temperature equal to 150 °C).

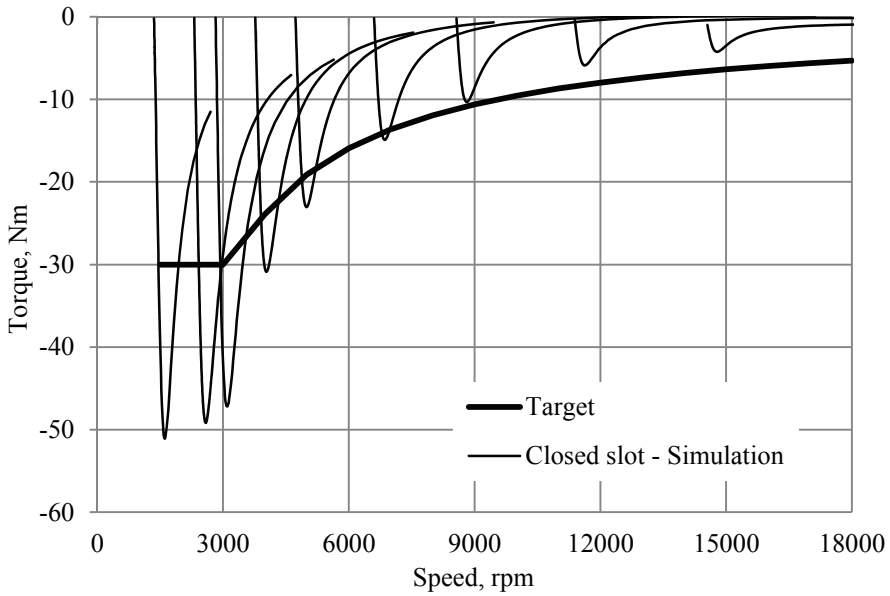

Fig. 5.5.4. Closed slot prototype: predicted generator performance (stator temperature equal to 150 °C).

Fig. 5.5.3 and Fig. 5.5.4 show similar results in the generation mode up to 9000 r/min; above this speed, due to the severe voltage limitation, a small discrepancy with respect to the expected performance has been observed for closed rotor prototype. However, considering the torque-versus-speed profile required during the urban driving cycle (see Fig. 3.3.2), these discrepancies can be acceptable in the real use of the vehicle

5.6. Conclusion

In this section, the design and testing of an electrical machine for mild-hybrid powertrain applications has been presented. Complete design aspects of a multiphase IM prototype respecting the system requirements have been presented and discussed. In particular, it was found that a multilayer bar conductor topology for the stator winding production is an interesting candidate for high-current and high frequency applications, even in the case of small-size machines. In addition, the open rotor slot configuration was proven to be the candidate for the fully achievement of the required performance in the whole speed range without compromising the mechanical robustness. Test results are presented, and it is shown a good agreement between predicted and measured data. The achievable performance, computed using the measured machine parameters, demonstrated the feasibility of the proposed design solution.

6. Thermal management

6.1. Stator winding thermal models for short-time thermal transient

The continuous request for more efficient and ever more compact electrical machines have lead towards the necessity to support electromagnetic designs with detailed thermal assessments. As well known, the performance of an electrical machine, both in steady state and in transient operations, are directly related to its thermal behavior and cooling capabilities. The thermal overload of the machine can cause severe damages to those components that are sensitive to the temperature, in particular the winding insulation system. Whenever the winding temperature exceeds the maximum values allowed by the insulation class, the insulation lifetime is heavily reduced by the thermal aging degradation effect. For this reason, the thermal analysis assumes an even more important role for those electrical machines that are used in applications with short-time load and overload operations, such as automotive and aerospace.

To cope with the thermal analysis of electrical machines, in the last decade different methods and software have been proposed by the scientific community as well as by industry [60]-[63]. Looking through the technical literature, the methods to face up the electric motor thermal analysis can be divided in two main categories: numerical and analytical methods.

The numerical methods, such as Finite Element Analysis (FEA) and Computational Fluid Dynamics (CFD), allow a detailed model of any device geometry and the prediction of thermal flow in complex regions [64]-[66]. However, both FEA and CFD simulation tools are very demanding in terms of model setup and computational time. For this reason, these tools can be considered a valuable support for offline computations only, typically during the machine design stage. To match a fast solution with results accuracy, analytical methods are mostly used [67]. These approaches are mainly based on lumped parameters thermal networks composed of thermal resistances, capacitances and heat sources representing the machine losses.

Both the numerical methods and the analytical ones are based on many thermal and mechanical parameters, which depend on the manufacturing process and that are not analytically computable. As a consequence, using thermal models, several

issues arise into the designers' mind. For a correct selection of these parameters, a valuable benefit may come from an empirical design experience on similar machines having a comparable manufacturing process. However, there are unquestionable difficulties for the users facing for the first time electrical machine thermal analysis. As a first attempt, in particular working on conventional industrial machines, it is possible to refer to the data reported in the technical literature, but in this case, particular attention has to be paid to focus on papers dealing with machines having similar features. In this perspective, in the last decade many efforts have been made by the researchers to find out the most critical thermal parameters. For instance, in [68] and in [69] some values for the thermal resistivity of the winding insulation, or the heat transfer coefficients for natural and forced convection of complex geometries (finned frames, end-caps air volume, etc.), have been discussed and reported. It is important to highlight that the aforementioned difficulties on the thermal parameters selection affect whatever thermal analysis approach. However, from the practical point of view, the main advantage of analytical methods relies on the reduced computational efforts necessary to predict the temperature in different machine parts.

Electrical machine thermal analysis can be requested for defining its behavior both in steady state or transient conditions. Several thermal models able to predict the temperatures in presence of load variations have been proposed in the technical literature, as well as implemented in commercial software. The typical use of these models is the machine temperature prediction in applications where the load variations follow a defined duty cycle or the load is imposed by a specific Service Factor (SF) [63], [70]. During the electrical machine design stage, the implementation of analytical models into state-of-the-art simulation tools like Matlab® is straightforward and it is not expected to result in numerical or computational issues. Their simplicity can be beneficial for multi-physics analyses, for instance interfacing the analytical thermal model with more complicated systems like electromagnetic transient simulations.

Another field where the transient thermal models find applications is the real time temperature prediction in machines used in variable speed drives. Depending on the thermal network complexity, analytical models can be used for the online and real time temperature evaluation in several parts of the machine during its working operations. This allows undertaking real-time actions on the control strategies to prevent the machine overheating [71], [72]. The online monitoring techniques present higher accuracy and reliability with respect to the temperature measurement through thermal sensors embedded in the machine. In fact, these latter are an additional cost and suffer of detachment risk during the machine

lifetime (uncertainties due to the contact resistance and on the exact sensor position) [73], [74].

Nevertheless, despite the reduced computational efforts requested by analytical models, complex thermal networks might not be suitable for online applications in a drive. In fact, high order models lead to a larger number of differential equations to be solved, thus requiring higher computational resources. In this perspective, previous research activities on comprehensive thermal model reduction can be found in literature [70], [73], [75]-[78].

In [79], an interesting analysis of the electrical machine thermal behavior in short-time transient is reported. In particular, the sub-transient, transition and transient thermal regimes (after which the machine is considered close to its thermal steady state conditions) are discussed separately to explain the involved physical phenomena in each of the three regimes. The comparison between predicted and experimental results confirms the validity of the proposed approach. As well known, and analytically discussed in [79], when an electrical machine operates in overload conditions, the fastest as well as the maximum temperature rise occurs in the stator windings. As a consequence, an accurate and reliable stator winding thermal model is mandatory when a real time prediction of the machine winding temperature is requested.

In this section are proposed, analyzed and validated different stator winding thermal models for short-time thermal transients. The proposed thermal networks are based on a physical representation approach for all the thermal network components. In this way, the lumped parameters physical meaning can be matched with the geometrical dimensions and material characteristics of the stator winding and lamination. In particular, starting from a fourth order thermal system, composed of four RC cells in cascade, the model complexity has been progressively reduced down to a third, a second and then to a first order model. In particular, as demonstrated in the following, the proposed models are a reasonable compromise between network complexity and results accuracy.

The stator winding short-time temperature evolutions predicted by the four proposed models are compared with the measured temperatures on an industrial Total Enclosed Fan Cooled (TEFC) induction motor. For this experimental activity the industrial machine has been used in the place of the designed BSG since the prototype was under construction. Once the thermal models have been evaluated on TEFC machines, the stator-winding region of the BSG prototype has been modeled according to the proposed first order thermal network. Then, it is used to predict the stator winding temperature during operative load conditions.

6.1.1. Short-time thermal transient modeling

The first lumped parameter thermal model considered in this section is depicted in Fig. 6.1.1;

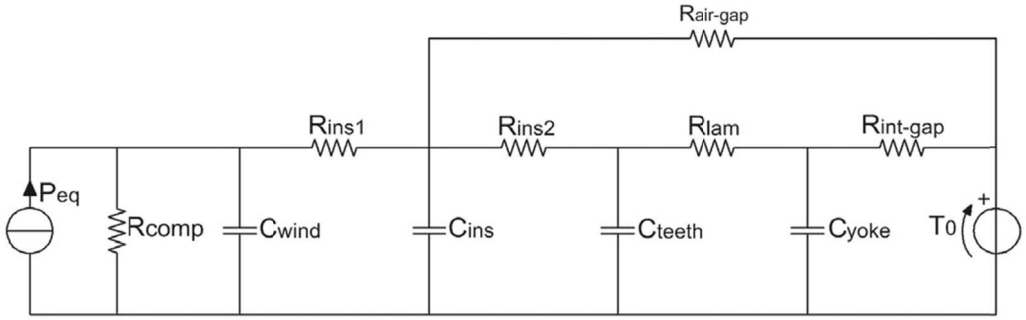

Fig. 6.1.1. Fourth-order starting thermal model

As well evident, the thermal network is a fourth order system composed of four RC cells in cascade. For the model order definition, the hypothesis of isothermal rotor and frame is considered during the thermal transient. On the base of this simplifying assumption, the rotor surface and the machine frame are individually assumed to be isothermal. Therefore, the rotor temperature, the frame temperature and the ambient one are all being considered equal to T_0. On the contrary, the winding (copper and insulation) can be considered an adiabatic system. It has also to be pointed out that, since the thermal resistance between the machine frame and the ambient is a complex quantity to be computed, the isothermal condition between frame and ambient allows neglecting this term improving the simplicity of the model. The thermal resistances R_{lam} and $R_{air\text{-}gap}$ can be computed by (6.1.1) and (6.1.2), respectively.

$$R_{lam} = \frac{1}{2\pi k_{ir} L_s} \ln\left(\frac{r_{oy}}{r_{iy}}\right) \tag{6.1.1}$$

$$R_{air-gap} = \frac{1}{2\pi k_{air} L_s} \ln\left(\frac{r_{o-airgap}}{r_{i-airgap}}\right) \tag{6.1.2}$$

In particular, since the rotor speed is zero, the air-gap thermal resistance can be computed considering an air cylinder having a constant thickness determined by the inner and outer radii of the air-gap.

The thermal resistance of the interface gap, $R_{int\text{-}gap}$, cannot be evaluated analytically [68] and it can be obtained by the calibration of the model after the steady state thermal test [61].

TABLE VII.

THERMAL RESISTANCE VALUES

$R_{cu\text{-}ir}$ (°C/W)	R_{ins1} (°C/W)	R_{ins2} (°C/W)	R_{lam} (°C/W)	$R_{int\text{-}gap}$ (°C/W)	$R_{air\text{-}gap}$ (°C/W)	R_{comp} (°C/W)
0.0445	0.0045	0.0400	0.0031	0.0300	0.2000	-0.537

TABLE VIII.

THERMAL CAPACITANCE VALUES

C_{wind} (J/°C)	C_{ins} (J/°C)	C_{teeth} (J/°C)	C_{yoke} (J/°C)
1910	680	2194	5623

The conduction thermal resistance of the frame is neglected because always lowers than $R_{int\text{-}gap}$ [61]. Even the thermal resistance copper-iron, $R_{cu\text{-}ir}$, is obtained by tuning the model after the steady state test; from its value it is possible to get the two thermal resistances R_{ins1} and R_{ins2} according to (6.1.3) and (6.1.4).

$$R_{ins1} \approx 0.1\ R_{cu\text{-}ir} \tag{6.1.3}$$

$$R_{ins2} \approx 0.9\ R_{cu\text{-}ir} \tag{6.1.4}$$

It is important to remark that equations (6.1.3) and (6.1.4) have been empirically determined through a test campaign conducted on several TEFC industrial induction machines of different manufacturers. Equations (6.1.3) and (6.1.4) reflect the physical reality of the winding system. In fact, R_{ins1} takes into account the wire insulation (enamel etc.), while R_{ins2} takes into account the slot insulations materials (slot liners, impregnation etc.). The thermal capacitances of the winding, including slot and end-winding (C_{wind}), the yoke (C_{yoke}) and the teeth (C_{teeth}) can be computed using (6.1.5), (6.1.6) and (6.1.7).

$$C_{wind} = V_{wind}\ \delta_{cu}\ c_{cu} \tag{6.1.5}$$

$$C_{yoke} = V_{yoke}\ \delta_{lam}\ c_{lam} \tag{6.1.6}$$

$$C_{teeth} = V_{teeth}\ \delta_{lam}\ c_{lam} \tag{6.1.7}$$

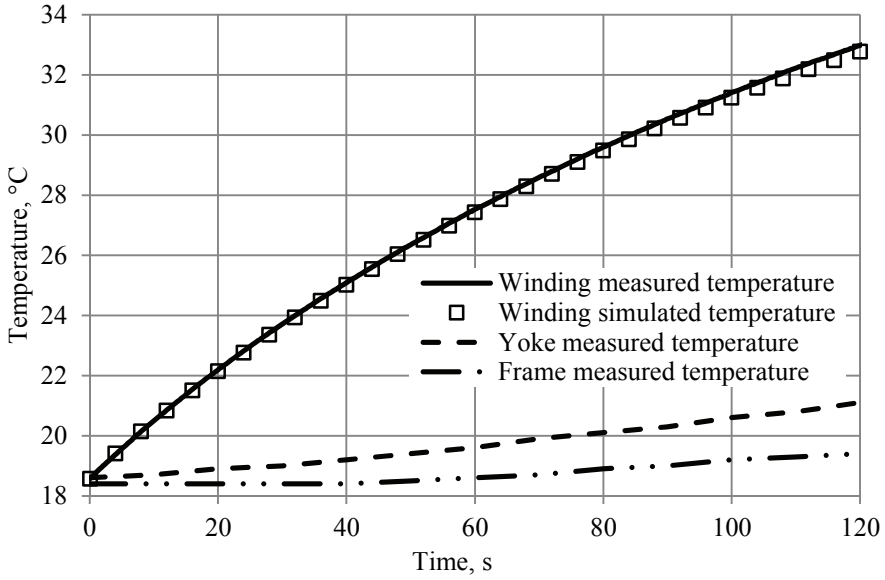

Fig. 6.1.3: Comparison between predicted and measured over-temperatures for the fourth order thermal model.

The thermal capacitance of the insulation material C_{ins} can be evaluated by (6.1.8).

$$C_{ins} = V_{slot}\,(1-k_{ff})\,\delta_{ins}\,c_{ins} \tag{6.1.8}$$

The values of the thermal resistances and those of the thermal capacitances for the DUT are reported in Tables VII and VIII, respectively. The thermal network shown in Fig. 6.1.2 has been solved using the multi-domain solver of the multi-physic software *Portunus* [84]. The comparison between predicted and measured over-temperatures is shown in Fig. 6.1.3. Obviously, both the simulation and the measurement have been referred to the same ambient temperature T_0, which is the initial temperature of the test. In Fig. 6.1.3 it is well evident the excellent agreement between the measured and the predicted winding over-temperatures. The maximum discrepancy on the over-temperatures after 60 s and 120 s are equal to -1.2% and -1.7 %, respectively. Looking at Fig. 6.1.3, the hypothesis of an isothermal frame can be considered valid up to 60 seconds; after that time, the frame temperature increases reaching, at the end of the test, an over-temperature of 1 °C with respect to the initial temperature. For the size of the DUT, 60 seconds can be considered a short-time thermal transient. Under this hypothesis, the stator winding temperature predicted by the thermal model follows very well the measured one. Nevertheless, neglecting the small increase of the frame temperature, the goodness of the model can be extended up to 120 seconds.

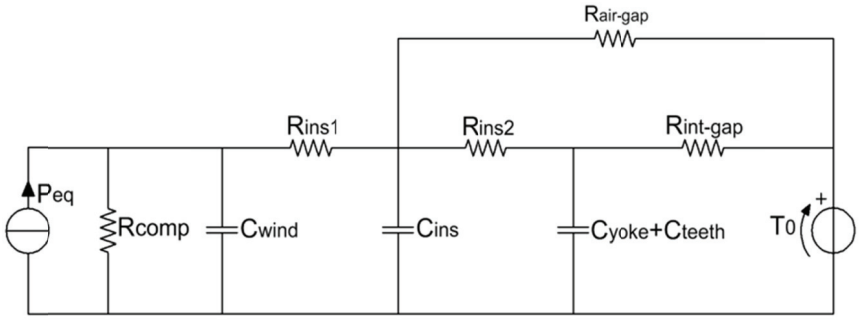

Fig. 6.1.4: Proposed third order thermal model.

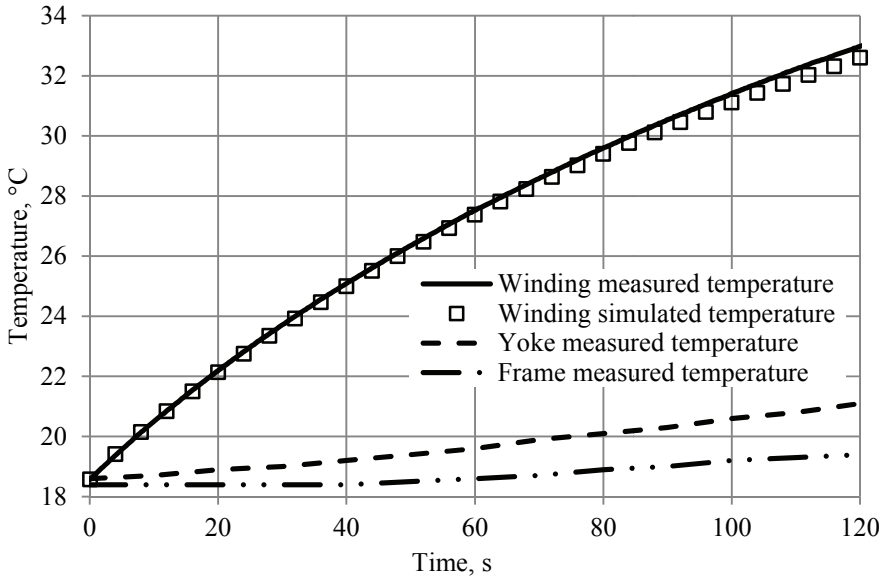

Fig. 6.1.5: Comparison between predicted and measured over-temperatures for the third order thermal model.

6.1.2. Thermal model order reduction

As previously discussed, the fourth order thermal network proposed in Fig. 6.1.2 represents with a good accuracy the physical phenomena in the stator system. Looking at the values of thermal resistances listed in Table VII, it is evident that R_{ins1} and R_{lam} have different order of magnitude compared to the other thermal resistances. For this reason, the proposed thermal model has been modified introducing an order reduction, moving toward a third order system composed of three RC cells in cascade. The order reduction of the model is practicable since the thermal resistance R_{lam} is one order of magnitude lower than $R_{int\text{-}gap;}$ as a consequence, it can be moved in series with $R_{int\text{-}gap}$ and the thermal capacitances will results connected in parallel. The obtained third order thermal

network is reported in Fig. 6.1.4, while Fig. 6.1.5 shows the comparison between predicted and measured stator winding temperatures. Even if the third order model presents a worse response with respect to the fourth order one, the accuracy of the model can still be considered satisfying having a winding over-temperature errors equal to -1.8% and -2.8% after 60 s and 120 s, respectively. On the base of the previous result the third order model has been further reduced to a second order one. Since the thermal resistance R_{ins1} is one order of magnitude lower than R_{ins2} , the reduction to the second order has been done connecting in series R_{ins1} and R_{ins2}. The addition of the two thermal resistances, R_{ins} , represents the total thermal resistance of the winding (enamel, impregnation, liner, etc.).

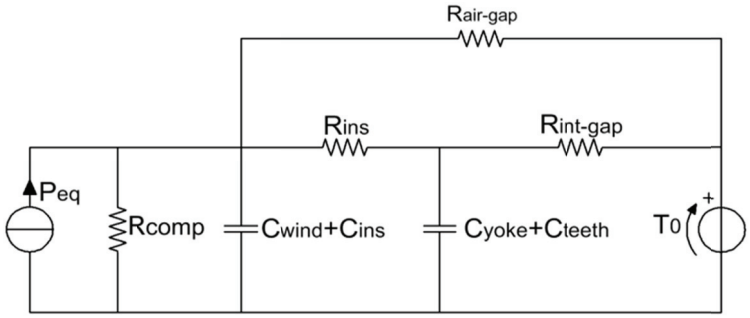

Fig. 6.1.6: Proposed second order thermal model.

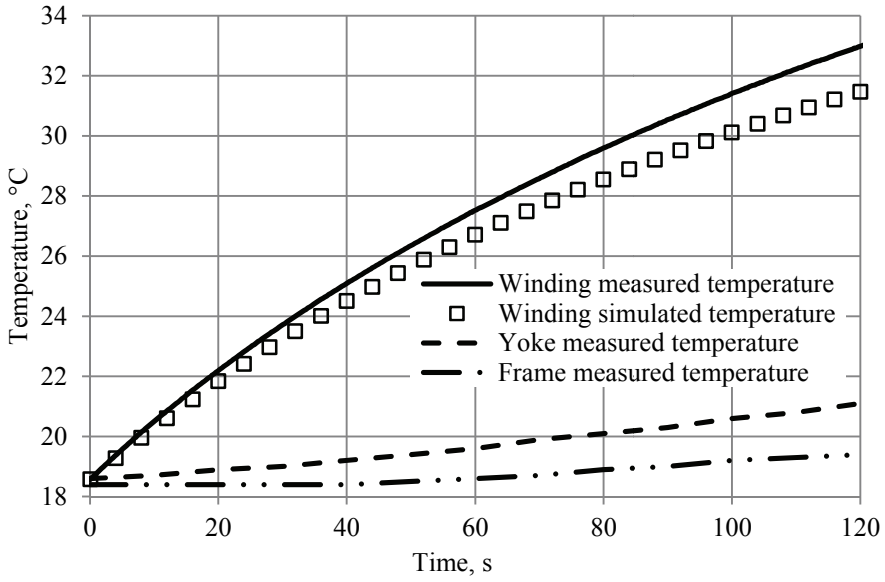

Fig. 6.1.7: Comparison between predicted and measured over-temperatures for the second order thermal model.

Due to this modification the thermal capacitances C_{wind} and C_{ins} will result in parallel. The thermal network and the comparison between predicted and measured temperatures are shown in Fig. 6.1.6 and in Fig. 6.1.7, respectively. As can be seen, the second order model leads to a discrepancy increase between the predicted and the measured values, with a winding over-temperature error of -9.3% and -8.7% after 60 s and 120 s respectively. Considering the evident simplification of the thermal network, the second order model still continues to represent the thermal phenomena and it could be acceptable in several applications.

6.1.3. Thermal model analytical solution

In addition to the thermal network solutions by *Portunus*, the three thermal models previously proposed have been solved using a fully analytical approach. As well know, the solution of the differential equations system representing the proposed thermal networks can be expressed as a sum of exponential terms as in 6.1.9).

$$T_w = T_0 + \sum_{k=1}^{n} A_k \left(1 - e^{-\frac{t}{\tau_k}} \right) \tag{6.1.9}$$

where:

n is the order of the differential equation system; A is the amplitude of the response k, τ is the time constant of the response k.

The aim of the analytical solution is to investigate the time constant τ_k, and amplitudes A_k, of (11) for each of the proposed thermal models. Their values, obtained using Matlab®, are listed in Table IX and Table X, respectively.

It is well evident that, in the fourth order model the first term has small amplitude A_1 and it decays in the first 10 seconds of the transient. The second term has negligible amplitude A_2. In the third order model, the second time constant τ_2 is missing, while the third and the fourth time constants and amplitudes are comparable to those of the fourth order model. Since the amplitude A_2 is negligible, the behavior of the two models is practically the same. Although in the second order model the first two time constants are missing, the deterioration of the estimation is mainly due to the reduced amplitudes of A_3 and A_4 as shown in Fig. 6.1.7.

TABLE IX.
TIME CONSTANTS

	τ_1 (s)	τ_2 (s)	τ_3 (s)	τ_4 (s)
Fourth order	2.09	4.68	73.5	315
Third order	2.10	---	71.8	310
Second order	---	---	67.0	306

TABLE X.
AMPLITUDES

	A_1 (°C)	A_2 (°C)	A_3 (°C)	A_4 (°C)
Fourth order	0.116	0.005	8.86	22.0
Third order	0.117	0	8.85	21.0
Second order	0	0	7.94	19.4

6.1.4. First order thermal model

As discussed in the previous sections, in order to evaluate the short-term current overloads in an electrical machine, it is acceptable to make the assumption that the stator copper heats up in an adiabatic way. This means to neglect its head exchange with any other parts of the machine. In this contest, the stator winding thermal model can be simplified to a first order model as shown in Fig. 6.1.8, where only the winding equivalent thermal resistance and the winding equivalent thermal capacitance are involved. In the first order thermal model, only the winding parameter are taken into account, while all the other parts of the machine are neglected because they are considered isothermal during the short time thermal transient.

The resulting first order thermal network is reported in Fig. 6.1.8. The winding equivalent thermal resistance R_{eq} is obtained by the addition of R_{ins1} and R_{ins2}, while the winding equivalent thermal capacitance C_{eq} is obtained by the addition of C_{wind} and C_{ins} as in (6.1.10) and in (6.1.11), respectively.

$$R_{eq} = R_{ins1} + R_{ins2} \tag{6.1.10}$$

$$C_{eq} = C_{wind} + C_{ins} \tag{6.1.11}$$

In Fig. 6.1.9 is shown the comparison between the stator winding temperature predicted using the proposed first order thermal model and that measured on the DUT.

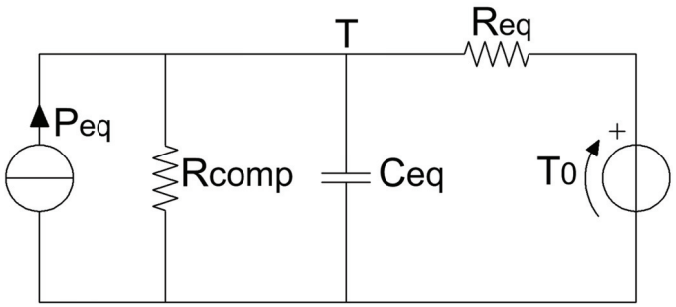

Fig. 6.1.8: First order thermal model.

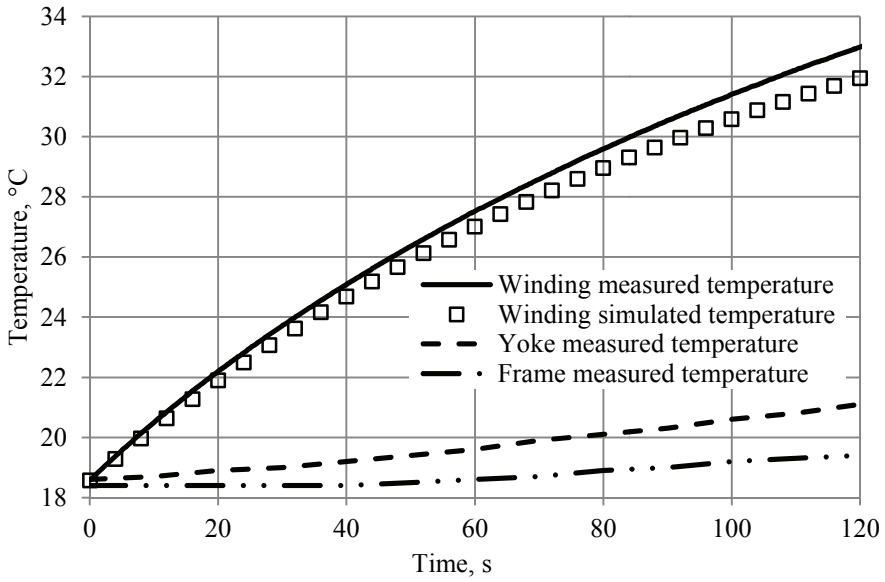

Fig. 6.1.9: Comparison between predicted and measured over-temperatures for the first order thermal model.

As can be seen, a good agreement between the predicted and the measured temperature has been obtained. The error is -4.5% and -3.5% at 60 s and 120 s, respectively.

As discussed in detail in the next section, the values of the equivalent thermal resistance R_{eq} and capacitance C_{eq}, can also be measured directly by means of the short-time thermal test. The computed values (using (6.1.10) and (6.1.11)) and the measured ones (through the short-time thermal test) of R_{eq} and C_{eq} for the DUT are listed in Table XI. Taking into account the complexity of the winding thermal insulation system, the comparison between the measured and the computed values is more than reasonable. As a consequence, the temperature predicted using both the computed and the measured parameters are practically overlapped.

TABLE XI.
MEASURED AND COMPUTED WINDING EQUIVALENT THERMAL PARAMETERS

	Computed value	Measured value
R_{eq} (°C/W)	0.0445	0.040
C_{eq} (J/°C)	2590	2366

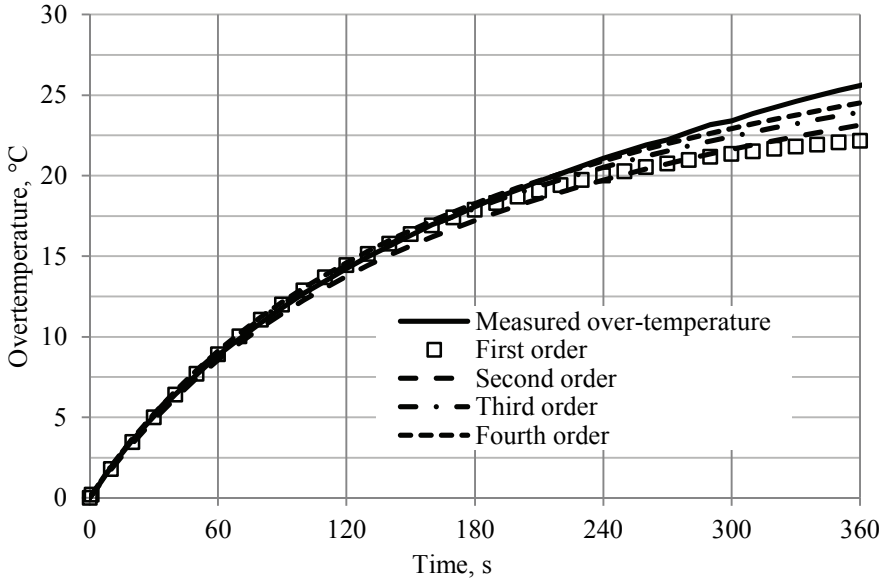

Fig. 6.1.10. Comparisons among the measured and the predicted over-temperatures for the four thermal models (longer time thermal transient).

In order to evaluate the behavior of the four models in longer thermal transient, a test with duration of 360 s has been performed. In Fig. 6.1.10, the comparisons among the measured and the predicted over-temperatures for the four thermal models are reported. It is well evident, as expected, that a reduction of the model order leads a reduction of the accuracy. However, it is important to highlight, that the first order thermal model, provides results comparable to higher order model in short time thermal transient (both for 60 s and 120 s).

6.1.4.1. Thermal Parameters Determination of First-order Model

In order to evaluate the thermal parameters of the stator windings, the experimental approach proposed in [XIX] has been adopted. The winding system is modeled as a first-order thermal network illustrated in Fig. 6.1.11, where R_{eq} and C_{eq} are the winding equivalent thermal resistance and the equivalent thermal capacitance, respectively.

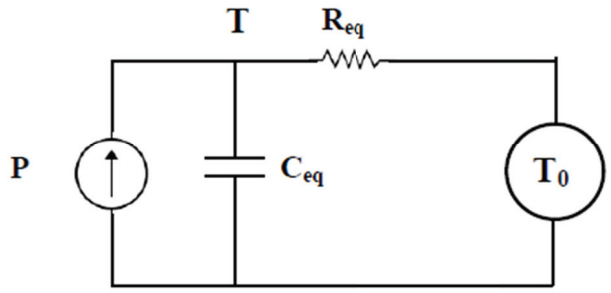

Fig. 6.1.11. First-order winding thermal network.

The simplified thermal model is based on the assumption of an isothermal back iron during the short-time thermal transient. The experimental procedure to evaluate the thermal parameters is hereafter reported. The method consists on warming the stator windings of the machine by the injection of a *dc* current. In this way the heat source is localized in the windings, while iron and mechanical losses are not generated. In order to avoid damage to the winding insulation during the test, the current in each phase must not exceed the rated one. At the beginning of the test, the machine has to be at the room temperature while the test terminates when the stator lamination temperature is 1 °C higher with respect to the initial one. During the *dc* test voltage and current at the phase machine terminals have to be acquired with a sampling frequency in the range of 1-5 Hz. Finally, the winding temperature is assessed from the winding resistance variation, following the well-known relationship:

$$T = \frac{R_T}{R_0}(B + T_0) - B \qquad (6.1.12)$$

where R_T is the winding electrical resistance ($R_T = v_{dc}/i_{dc}$) and B is the material thermal coefficient, whose value is equal to 234.5 K for copper. Though it is not explicit in equation (6.1.12), T is a function of time since R depends on v_{dc} and this electrical quantity changes with time. The reference value for the winding electrical resistance, R_0, is evaluated at T_0 = 25 °C. Once the time evolution of the winding temperature has been deducted, the thermal capacitance of the winding system can be computed by means of the electrical energy provided during the test ($W = v_{dc}(t) \cdot i_{dc}(t) \cdot t$). In particular, fitting the energy in function of the winding temperature variation with a linear regression, the value of the thermal capacitance C_{eq} can be directly obtained by (6.1.13).

$$C_{eq} = \frac{dW}{dT} \qquad (6.1.13)$$

Since all the variables are known, the equivalent thermal resistance R_{eq} can be determined from the mathematical representation of the first-order thermal network (6.1.14). Where P is the power loss and the indices k and 0 refer to time instant and initial condition, respectively. The procedure for finding the optimal value of R_{eq} is based on minimizing the squared deviation between the measured temperature and the one obtained by means of the mathematical model (6.1.14).

$$T_k = T_{k-1} + \left(T_0 + R_{eq}P_{k-1} - T_{k-1}\right)\left(1 - e^{-\frac{t_k - t_{k-1}}{R_{eq}C_{eq}}}\right) \qquad (6.1.14)$$

The procedure described above reports the general rules for the thermal parameters assessment; however, some practical remarks are necessary. The first point to be clarified concerns the connection of the stator phases during the *dc* test; if all the phase terminals are available, they can be connected in series or in parallel. Series connection is suggested because it guarantees the same current in each phase. In case of Y connection with inaccessible neutral point, the test can be performed supplying two phases. The obtained results have to be opportunely scaled, as only two phases are used. In particular, the thermal capacitance and thermal resistance must be multiplied by 3/2 and 2/3, respectively. The second point regards the duration of the test to ensure the isothermal condition of the back iron. As described above, this assumption is mandatory for modeling the windings system with a first-order thermal network, neglecting the other parts of the machine. The back iron can be considered isothermal if its temperature do not increase more than 1 °C in relation to the initial temperature. However, this value is not critical and it is conservative for a good parameters determination. In electrical machines where the back iron temperature cannot be measured, a long thermal transient test (range of minutes depending on the machine size) can be performed. Nevertheless, only the initial values are useful for the thermal parameters assessment. In particular, the very initial samples (where the energy vs temperature is a straight line) must be considered for the thermal capacitance evaluation. While the time range to be used for fitting the measured temperature is in the range of the winding thermal time constant.

6.1.4.2. Validation in motor operative condition

From an industrial application point of view, the main advantage of a first order thermal model relies on the very limited computational resources that are required to predict the stator winding temperature in case of short-time overload. Due to its simplicity, a first order thermal model can be easily inserted in the fastest motor control routine implemented in a Digital Signal Processor (DSP).

Therefore, the stator winding temperature can be obtained during short-time overload torque transients with the same dynamic of the current/torque control scheme. Consequently, the motor current will be limited in case of stator over-temperature.

More complex thermal models are usually included in control tasks that are executed with very slow sampling periods with respect to the fastest motor control routine. For this reason, while the more complex comprehensive thermal models can be used to evaluate temperatures in many parts of the machine in long time evolution, the first order thermal model can be used as a support to predict the stator winding temperature in case of severe short-time overloads. From the practical point of view, reduced models of the whole machine [75]-[78] can be used as monitoring of the winding temperature (Machine Thermal Image), while the proposed first order model can be used for the prediction of the short-time thermal transient during the overloading conditions. It has to be pointed out that, the proposed first order thermal model allows the prediction of an average temperature of the stator winding, neglecting the presence of hot spots. However, as reported in [78], it is widely accepted that the hot spot temperature can be assumed 10 °C higher than the average temperature of the winding. Therefore, in a perspective of winding insulation protection, this margin can be a reasonable thermal overload protection for the motor overheating [78].

In this section, the proposed first order thermal model for short-time thermal transient is used to predict the stator winding temperature during short time transient of the prototype properly designed for severe overload operations. The implementation of the thermal model inside a drive is not the scope of this research activity. Thus, the model validation is performed offline and the predicted temperatures are compared with those measured on the prototype.

For monitoring purpose, several thermal sensors have been positioned in different parts of the machine, such as in the magnetic circuit, end-windings, stator housing and water jacket cooling channels. For the thermal assessments reported in this section, only the thermal sensors embedded in the stator end-windings have been used. Fig. 6.1.12 shows a sketch of the sensor positions on the end-windings. The colors code (blue, red, grey and green) used in Fig. 6.1.12 for the circles that represent the sensor positions has been adopted in the graphs throughout the section to identify the respective measured temperatures. Fig. 6.1.13 shows a detailed view of the prototype end-winding; the thermocouples, fixed by Kapton, are positioned between two adjacent bars.

Calibration

During the *dc* test, together with voltage and current, also the temperatures measured by the four thermal sensors placed in the end-winding (see Fig. 6.1.12) have been acquired. In Fig. 6.1.14 the temperature evolution during the performed *dc* test is shown. As can be seen, the temperature evaluated with the resistance variation method (hereafter identified as V-I method), is lower with respect to the winding temperatures measured by the thermal sensors. This result is reasonable because the resistance variation method considers the average temperature of the winding, while the sensors measure the end-winding temperature that usually is one of the hottest parts of the machine [79]. Among the four available sensors, since sensor 4 is the one that better fit the average winding temperature, it has been selected as the reference sensor for the comparison with the predicted temperatures. Fig. 6.1.15 compares the temperature measured by the sensor, the temperature evaluated with the V-I method, and the temperature predicted by the first order thermal model. With the aim to match the sensor measure with the average winding temperature resulting by V-I method, a constant correction factor is applied to the sensor 4. This correction factor is equal to the previously mentioned standard deviation. Fig. 6.1.16 shows the calibration of the sensor with respect to the average winding temperature resulting from the V-I method. It is evident that with the use of the correction factor, the temperature measured by sensor 4 can be used to represent the winding average temperature with an acceptable accuracy.

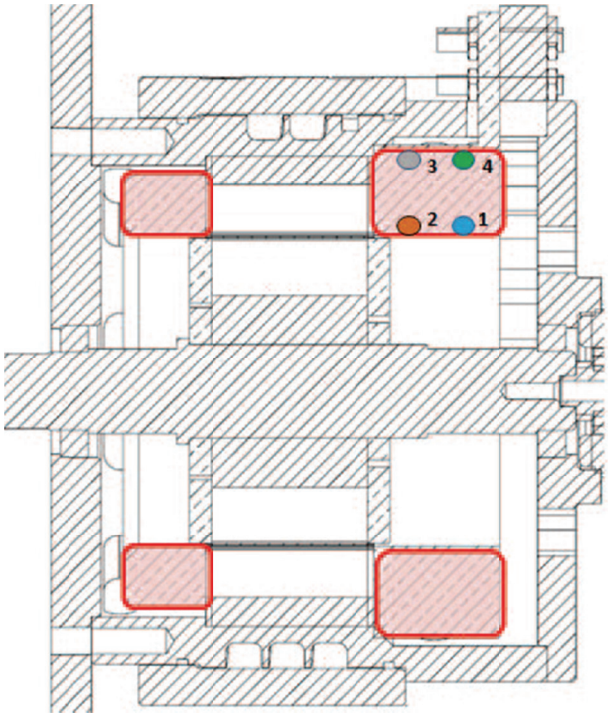

Fig. 6.1.12. Position of the thermocouples on the stator end-winding.

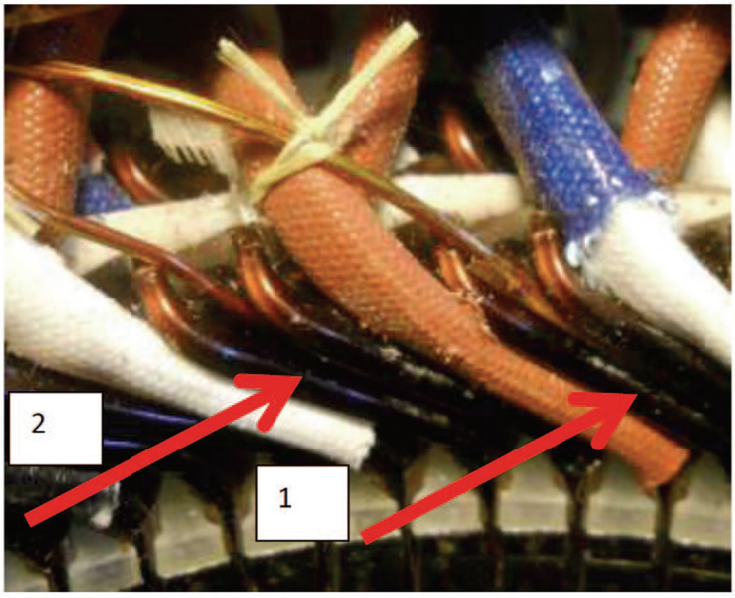

Fig. 6.1.13 Position of the thermocouples 1 and 2 on the stator end-winding.

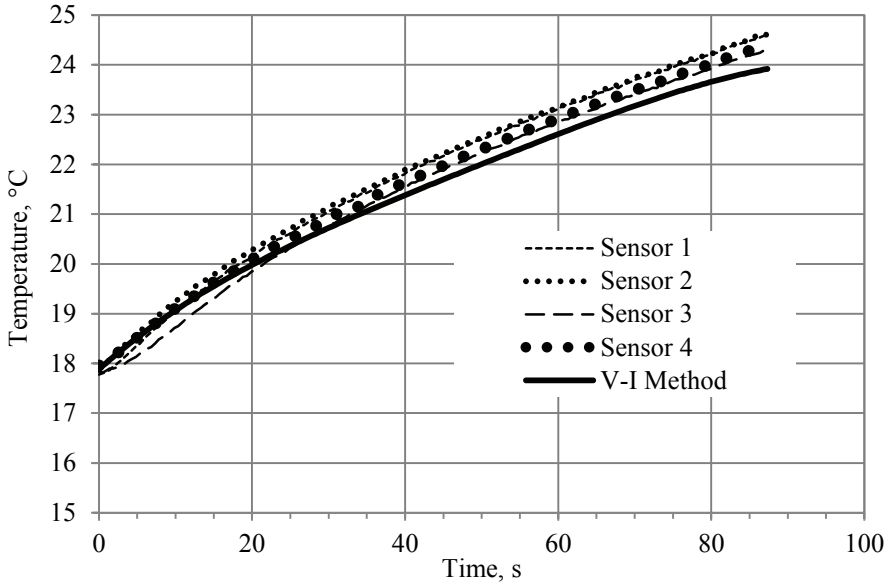

Fig. 6.1.14. Winding temperature variation during *dc* test.

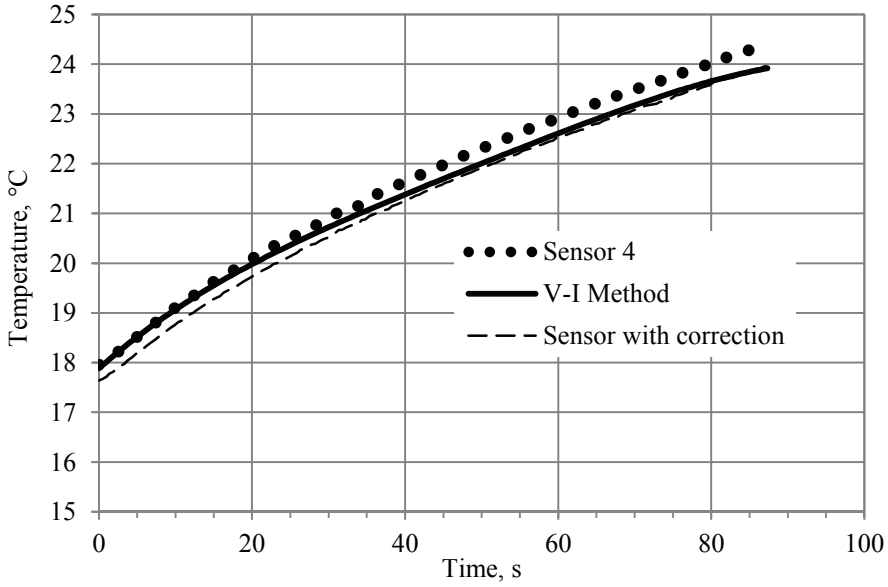

Fig. 6.1.15. Measured and estimated temperature during *dc* test.

Experimental measurement and model validation

As previously discussed, the method for evaluating the parameters of the first-order thermal network consists on supplying the stator winding of the investigated machines with a dc current. In this supply condition, only the stator Joule losses are present as heat source in the machines. Nevertheless, during normal operations

all the losses are active in the machine. Thus, the proposed first-order thermal model has to be validated in load conditions to understand the limit of its use. For this reason, the prototype has been tested at different torque and speed, where all the loss sources are active as well as the windage effect of the rotor. With reference to the double cooling system (forced air and water cooling) that equips the machine under test, it has to be pointed out that all the tests hereafter reported have been conducted using only the forced air cooling system.

The test campaign for a fully evaluation of the model performance has been done applying torque step variations at different rotational speeds. The machine under test has been supplied using a 40 kVA, three-phase sinusoidal static power source having a voltage range of 0 to 450 V with total harmonic voltage distortion lower than 0.1 % and a frequency range of 20 to 300 Hz.

The motor has been mechanically loaded using a high dynamic synchronous variable speed drive properly controlled to impose the required torque values. The electrical and thermal measurements have been done using a high precision power meter and a data-logger, respectively. As previously mentioned, the measured and predicted temperatures have been compared offline with a post processing analysis.

For the thermal model validation presented hereafter, the initial temperature has been considered equal to that measured at beginning of the test by the reference thermal sensor positioned in the end-winding connections; then, the winding temperature evolution has been predicted using (6.1.14). For each computational step (k), the Joule losses used as heat source in the thermal model have been computed considering the measured phase current and the phase resistance evaluated at the previous step ($k-1$).

In addition, since the prototype is affected by additional winding losses due to skin and proximity effects, a correction factor has also been applied to the phase resistance. The winding can be considered at steady-state in a time range equal to five times the thermal time constant of the winding.

The performed tests consist in loading the machine with a constant torque until the winding thermal steady-state condition is established, and then the motor is overloaded with a torque step. It is worth to note that, once the winding thermal steady-state condition has been reached, the Joule losses to consider as input for the thermal model in overload transient operation are those related to the additional step current. In other words, during overload operations, the Joule losses to consider are the difference between the winding Joule losses during the overload and those at steady-state.

Experimental results

In order to investigate the behavior of the first-order thermal model with different losses distribution inside the machine, the prototype has been tested at 750 rpm, 1500 rpm and 3000 rpm with different load torque levels. In particular, starting from the no-load condition, at 750 rpm the machine has been loaded at 12 Nm, while at 1500 rpm and 3000 rpm it has been loaded at 18 Nm. The comparison between the model response and the measured winding temperature during the tests are shown in Figs. 6.1.16 –Fig. 6.1.18. In all the conducted torque transient tests, the results show a good agreement between predicted and measured winding temperatures, with a maximum percentage error of 2%. It is important to remark that the accuracy of the proposed thermal model is valid for short-time thermal transient only, which for the machine under test is about 2 minutes long. Obviously, motors with different size will have different winding thermal time constant.

An important outcome of these tests is that the first-order thermal model has a complete validity in all the load conditions despite the model parameters are computed using a dc supply test. This means that other machine losses, such as iron and rotor Joule losses, as well as airgap and end-winding cooling effects due to the fan mounted in the rotor, do not influence the model response.

As the service factor of the starter-generator is known, a duty cycle test has also been performed in order to validate the model during intermittent load conditions. In this specific case study, starting from a no-load condition and a rotational speed of 1500 rpm, a load torque step equal to 18 Nm has been imposed with a 5s ON - 30s OFF duty cycle operation. The comparison between predicted and measured temperature is shown in Fig. 6.1.19. Also in this case, although the over-temperature and the time duration are small, a good match has been obtained between predicted and measured temperature with a percentage error lower than 2% at the end of the transient.

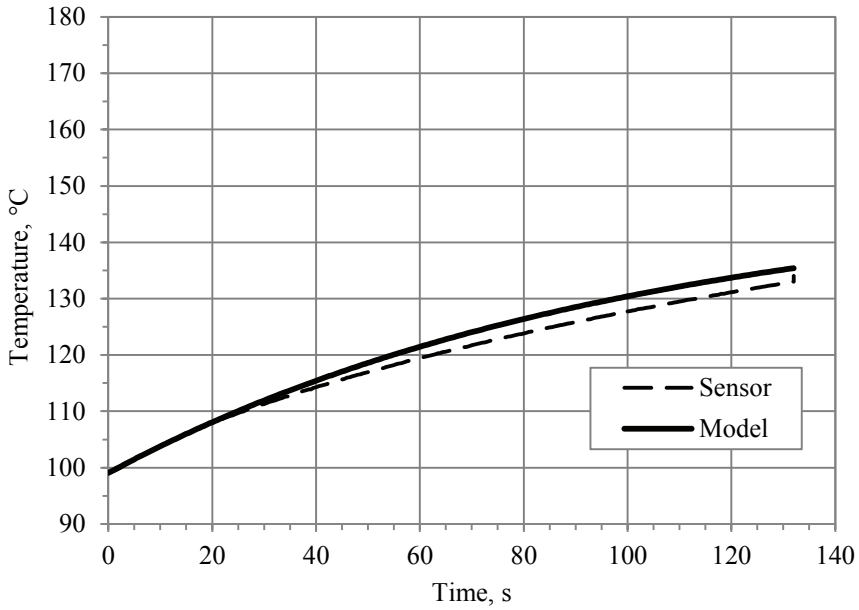

Fig. 6.1.16. Load torque step test at 750 rpm from 0 to 12 Nm, I=130 A, Pjstator=720 W.

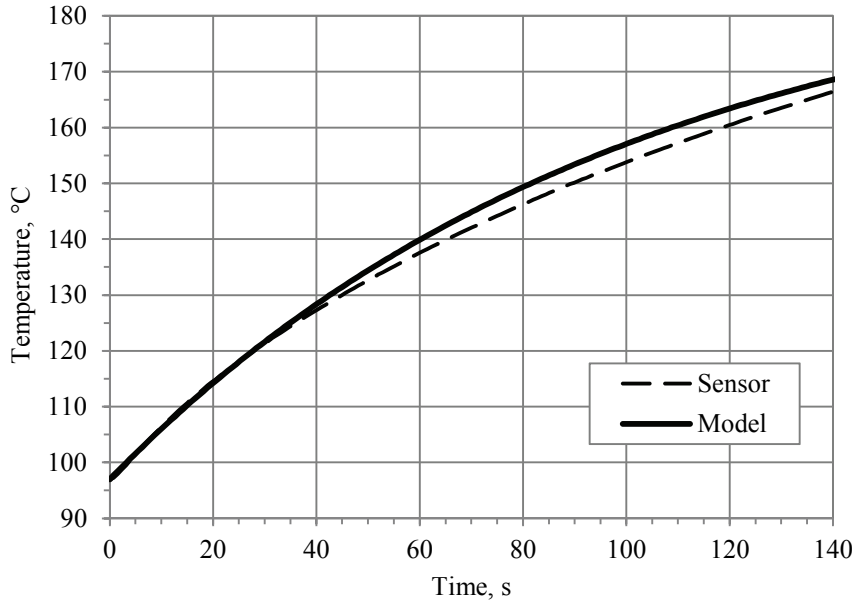

Fig. 6.1.17. Load torque step test at 1500 rpm from 0 to 18 Nm, I=180 A, Pjstator=1300 W.

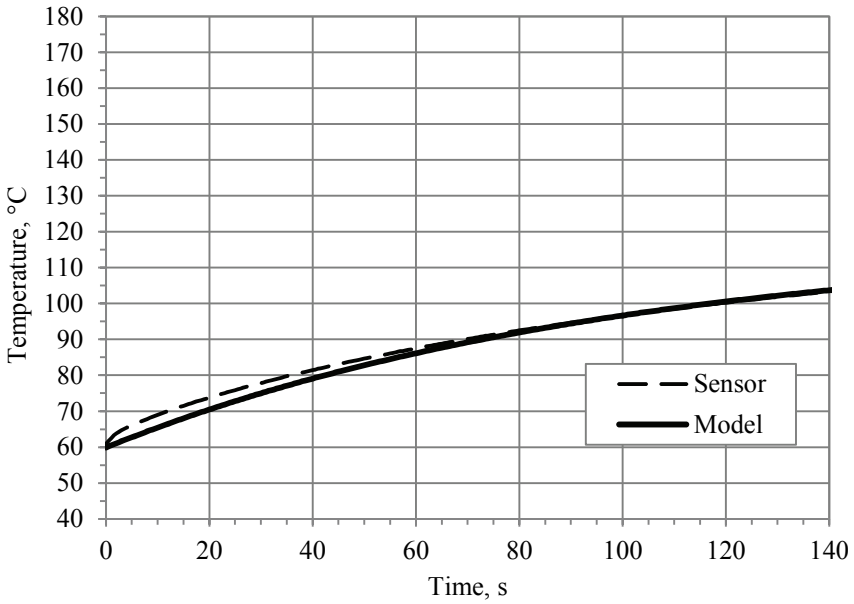

Fig. 6.1.18. Load torque step test at 3000 rpm from 0 to 18 Nm, I=150 A, Pjstator=840 W.

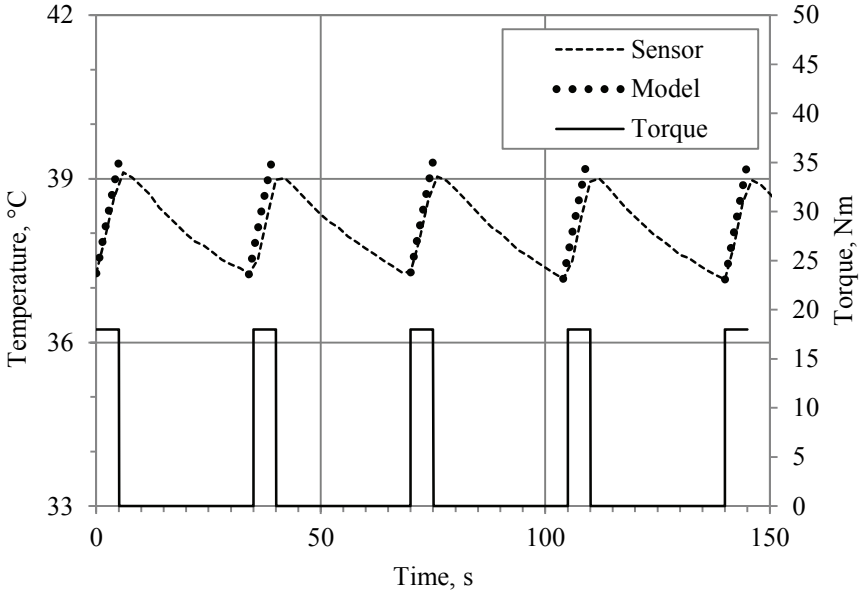

Fig. 6.1.19 Load torque test at 1500 rpm with 5s ON - 30s OFF duty cycle with a torque variation from 0 to 18 Nm.

6.1.5. Conclusion

On the base of the discussions and the experimental validations previously reported, it is reasonable to consider all the four proposed thermal models suitable for the short-time thermal prediction of the stator winding temperature. The choice of the most suitable one is delegated to the final user in function of the specific application as well as of the goal for which the model is implemented. As a general remark, due to their higher complexity, it is possible to consider the fourth and the third order thermal networks more suitable for theoretical analyses and thermal simulations during the motor design stage.

On the other hand, for their simplicity the second order and first order thermal models are particularly suitable for the implementation in electrical drives for the on-line and real time prediction of the ratio over-current/time duration. In particular, the first order model seems to be the best solution for its simple digital implementation in a control drive and the easiness in the thermal parameter determination using a *dc* voltage supply test.

As well known, to predict the actual temperature of the motor, many modern electrical drives already include a thermal model for long-time transient (also known as 'thermal image' of the machine). In this case, starting from the actual temperature evaluated through the long-time transient thermal model, the short-time transient thermal model allows determining the maximum over-current value when the transient duration is known or imposed, or vice versa. It is important to keep in mind that the proposed thermal models allow predicting an average temperature of the stator winding, neglecting the presence of hot spot.

The proposed first order model has been experimentally validated in operative conditions. The results confirm the validity of the simplified thermal model for the prediction of the winding temperature in short-time thermal transient, both for torque step response and intermittent services. The model accuracy, experimentally evaluated through the tests presented in the chapter, confirms the suitability of the proposed model for its implementation in a drive system for real-time evaluation of the winding temperature in overload conditions.

6.2. Analysis of different forced convection cooling system

The design of the BSG can be considered as a challenging task due to the severe constraints imposed by the automotive applications. These requirements, combined with the harsh environment of the engine compartment, inevitably lead to high temperatures of the electric machine, and an effective cooling system must be mandatorily adopted together with high temperature class insulation material. In addition, the BSG cooling system selection must account for the driving cycle that is characterized by very time-variable loss distributions.

Even if some non-conventional cooling systems have been recently presented (e.g. the oil-spray cooling solution [80], or the cooled rotor shaft reported in [81]), in automotive applications the typical cooling methods are based on air or liquid [12], [17].

In this section, the potentialities of heat extraction through forced convection are experimentally investigated on the BSG prototype. The prototype is equipped both with two centrifugal fans fixed on the rotor sides and a water jacket inside the external frame. In this way, it is possible to evaluate the air-based cooling without providing the liquid flow in the jacket, and the liquid-based cooling can be tested removing the fans from the rotor.

The design of cooling system of electrical machines operating with duty cycle is a critical issue because of variable torque and speed that means variable losses distribution with respect to the speed and time.

As reported in the previous section, the equivalent circuit parameters of the BSG prototype have been computed for several supply frequencies. These parameters have been used to estimate the total losses in the whole speed range. With respect to motoring operations, the total losses in continuative service for a temperature of 200 °C are shown in Fig. 6.2.1.

It can be see that the maximum total losses on the machine are about 6000 W at 2000 rpm. In this condition the copper losses are the predominant components: around 4500 W in the stator winding and 1400 W in the rotor cage, while the iron losses are around 85 W. At high speed, the flux weakening is used to regulate the machine in the constant power speed range and the total losses decrease in all their components. For example, at 9000 rpm the total losses are 1300 W, the stator Joule losses are 900 W, the rotor Joule losses are 200 W, and the iron losses are around 50 W. Considering the maximum performance and the aforementioned loss distributions, the most critical working point for the heat extraction is in the low speed region.

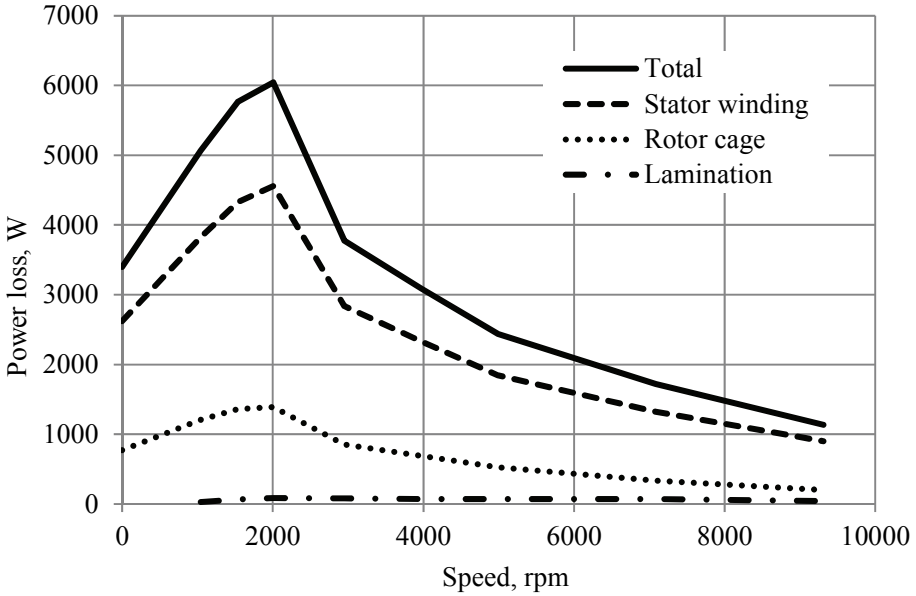

Fig. 6.2.1. Estimated electromagnetic losses for the motoring maximum torque-speed performance (shown in Fig. 1), continuative service at 200 °C.

For this reason, the maximum continuative dissipation at 2000 rpm is assumed as the reference for the cooling system definition together the specified duty cycle. Based on these considerations, the BSG thermal behavior depends both on its equivalent thermal capacity to cope with transient conditions (instantaneous dissipation during the duty cycle on time interval or during the driving cycle) and on its equivalent thermal resistance for the heat extraction in steady state conditions (average dissipation during the duty cycle period). The former could be analyzed through more or less sophisticated transient thermal model [79]-[78]).

The cooling system for the steady state heat extraction has to be designed according to the average dissipated power over the duty cycle. In the specific case study, the reference duty cycle is 14% and the maximum losses are 6000 W, resulting in 850 W of equivalent continuative losses. In order to experimentally investigate the possibility to extract through air or liquid this amount of average heat flux, respecting the insulation class of the machine, a special prototype equipped with both the two cooling systems has been built. Hereafter, the implemented cooling systems are briefly described.

6.2.1. Air cooling system

As for the conventional car alternators, two normal production centrifugal fans have been fixed by screws on the rotor end rings of the BSG prototype, one for

each side, as shown in Fig. 6.2.2. These fans radially blow air in the end-winding regions under the end caps using the holes shown in Fig. 6.2.3, on the left side. The dimensions of the holes for the air flow have been reasonably defined in order to limit the pressure drops in the air path, but they have not been subject of dedicated studies, typically performed using CFD analysis. Unfortunately, due to cost reasons, for the prototype was not possible to produce end caps having geometry similar to the one used for conventional alternators (see Fig. 6.2.3, right side). As a consequence, it is an author's opinion that some improvements from the fluid dynamics point of view could be possible. For sake of completeness, the readers can find interesting hints for an accurate fan design in [82], and [83].

To test the forced air-cooling system the holes in the frame must be obviously open and no liquid coolant must be supplied in the water jacket.

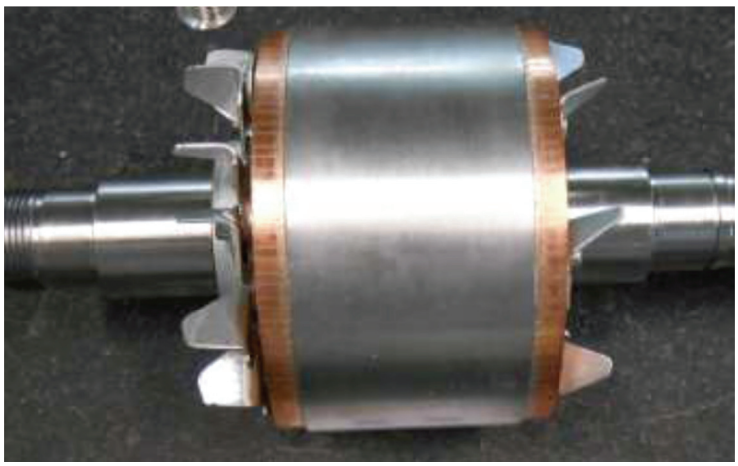

Fig. 6.2.2. Rotor of the prototype with centrifugal fans.

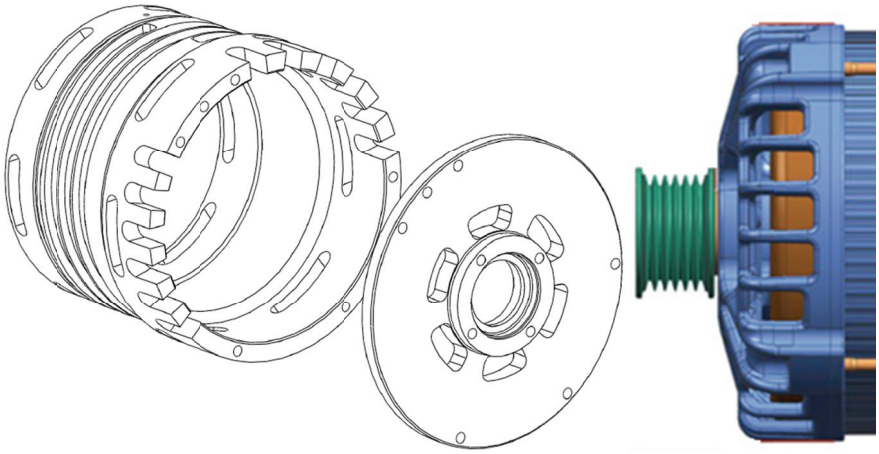

Fig. 6.2.3. Holes for the air flow in the end caps and in the external frame: BSG prototype (left) and conventional alternators (right).

6.2.2. Liquid cooling system

Since the major loss component is localized on the stator, a water jacket in the stator housing can be adopted to effectively remove the generated heat. In particular, for the BSG prototype, a helical water path has been produced in the frame zone in contact with the stator magnetic core, as shown in detail in Fig. 6.2.4.

In order to design the helical duct, the required flow rate is calculated according to (6.2.1):

$$Q = \frac{P_{Total\_loss}}{\rho C_p \Delta T} \tag{6.2.1}$$

where P_{total_loss} are the total losses to be removed by the liquid, ρ and C_p are the mass density and specific heat capacity of the liquid, respectively. ΔT is the maximum thermal gradient between inlet and outlet temperature of the liquid; in the specific case study ΔT is assumed to be 5 °C. Thus results in a minimum flow rate of 5 l/m.

$$A = \frac{Q}{v} \tag{6.2.2}$$

The duct cross-section area A is calculated by (6.2.2). Since the liquid speed v in pipes and tubes should not exceed 1.5-2.5 m/s, the area A has been defined equal to 92 mm^2 (8 mm height, and 11.5 mm width).

During all the thermal tests devoted to the investigation of the liquid cooling system, the holes in the external frame have been closed by means of a plastic tape, in order to nullify the external ventilation effects due to the rotor rotation.

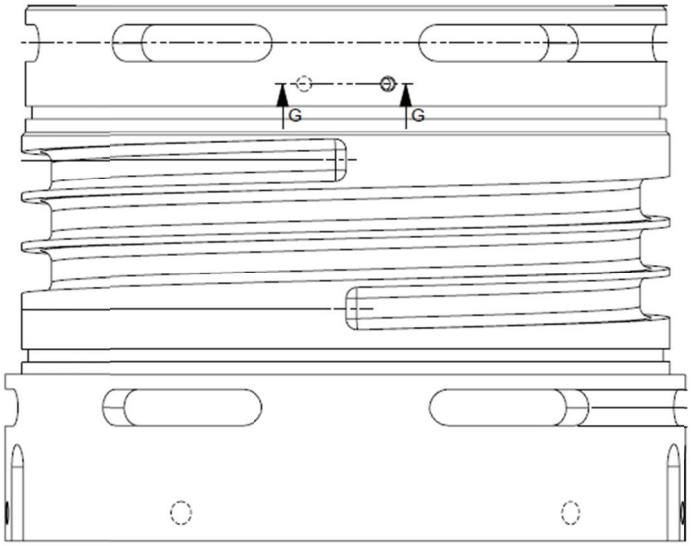

Fig. 6.2.4. External housing with helical path for water cooling.

6.2.3. Experimental results

In order to validate the thermal performance of the two cooling system, the prototype has been tested in steady-state thermal conditions; a view of the prototype mounted on the test bench is reported in Fig. 6.2.5. In order to provide the low-voltage high-current supply, a transformer has been interposed between the power source and the BSG. The used supply is a programmable sinusoidal power source rated power 40 kVA, with a total harmonic voltage distortion lower than 0.1%, and frequency range equal to 20-300 Hz. The thermal behavior of the machine was monitored through 20 thermocouples embedded in the magnetic circuit, end-winding, housing and water duct.

During the test, the prototype is mechanically loaded by means of the brake that imposes the speed of the system according to the desired total losses. The total losses dissipated inside the prototype have been measured as the difference of the input electrical power (measured with a high precision power-meter) and the shaft power (computed by the measured torque and speed).

The tests have been conducted for two constant values of dissipated losses, 500 W and 700 W, in the speed range of 750-4500 rpm. It is important to remark that due to current limitation of the used power supply, it was not possible to perform the thermal test with continuative losses of 850 W in the whole speed range.

Air cooling characterization

The measured stator winding-to-ambient over-temperatures versus the rotational speed are reported in Fig. 6.2.6, for the two considered loss values. As expected, the cooling capability improves with the speed, due to the increase of the airflow provided by the fans.

Looking at Fig. 6.2.6, it is possible to observe that in the speed range 2000-4500 rpm the point-to-point ratio between the two measured over-temperatures trends are practically equal to the ratio between the two considered total losses (700 W/500 W = 1.4) values. This means that, for a fixed rotational speed, the 'equivalent' thermal resistance between the stator winding and the ambient can be considered constant.

On the basis of this consideration, it is possible to estimate the over-temperature for a dissipated power equal to 850 W (the red curve reported in Fig. 6.2.6).

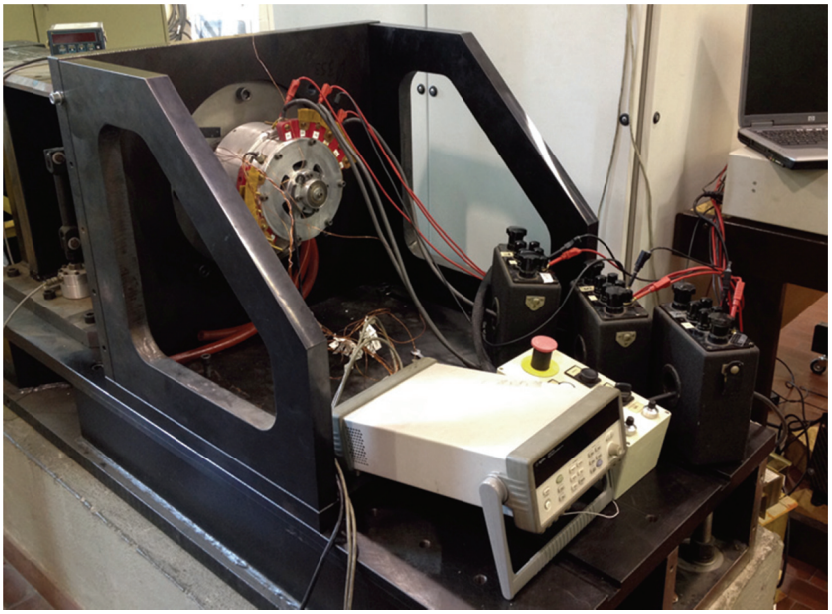

Fig. 6.2.5. Prototype mounted on the test bench for the thermal tests.

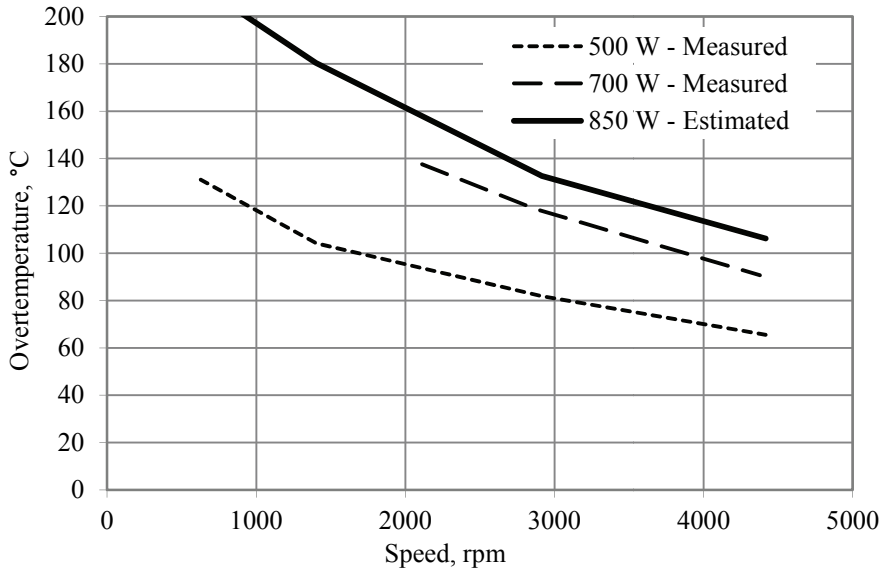

Fig. 6.2.6. Forced air cooling system performance: stator winding over-temperature.

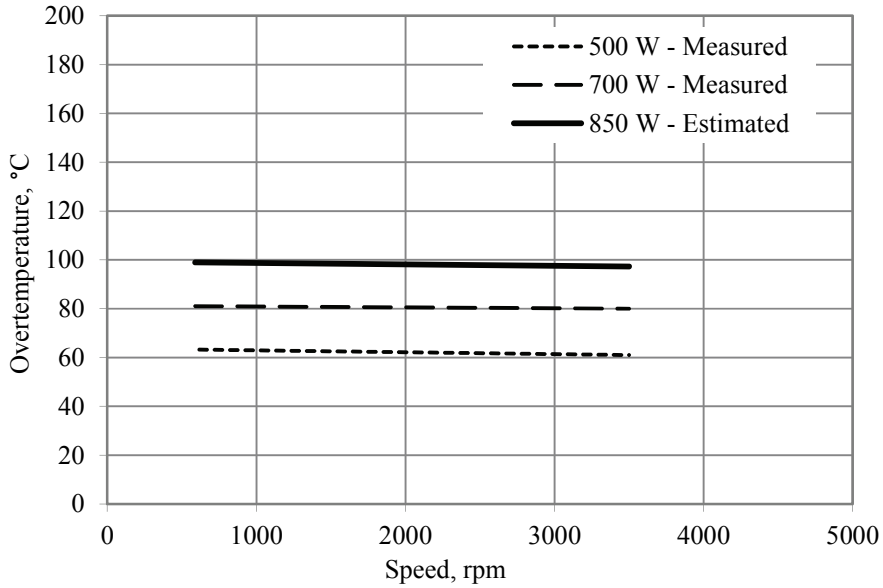

Fig. 6.2.7. Liquid cooling performance: stator winding overt-temperature.

Still considering Fig. 6.2.6, the results show that the air cooling system is not able to remove the dissipated losses in the worst case presented in Fig. 6.2.1 (6 kW at 2000 rpm, with the specified duty cycle) respecting the insulation class limit. Considering the very high temperature observed in the range 1000-2000 rpm, it is an author's opinion that an optimization of the fans and the air flow path is not enough to retrieve safe thermal operations.

Liquid cooling characterization

The water-cooling capability in continuative service is evaluated with the same procedure adopted for the air-cooling.

The tests have been conducted with the nominal flow rate equal to 5 l/min. During the tests the fans were removed from the rotor and all the holes in the external frames were closed with a plastic tape. Unfortunately, the fan removal leads to vibrations at high speed because the manufacturer executed the rotor balancing in presence of the two fans. For this reason, during these tests the maximum speed has been limited to 3000 rpm.

In this case, the point-to-point ratio of the measured temperature trends is still very close to the ratio of the two injected losses, and, as expected, is substantially constant in the whole explored speed range, as shown in Fig. 6.2.7. In other words, the windage effect of rotor speed without fans is negligible, and the 'equivalent' thermal resistance between the stator winding and the average temperature of the liquid coolant can be assumed constant with the speed.

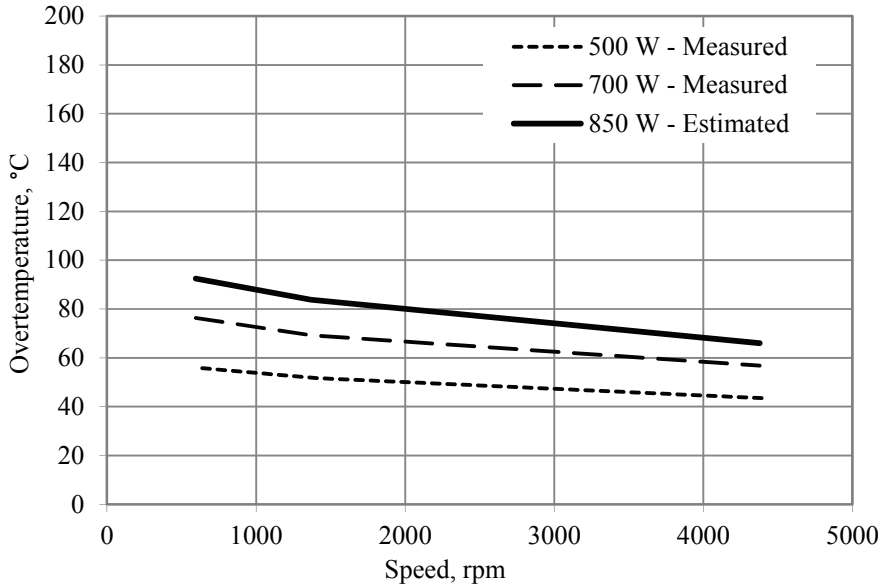

Fig. 6.2.8. Liquid cooling system performance with fans mounted on the rotor: stator winding over-temperature.

On the basis of this equivalent thermal resistance, an over temperature close to 100 °C has been computed for a constant dissipation of 850 W. As a consequence, the designed liquid cooling system is able to withstand with the aforementioned worst case.

In fact, assuming a temperature of the engine coolant temperature of 100 °C, a maximum average temperature of 200 °C of the stator winding can be predicted, leading to a margin of 20 °C with respect to the insulation class limit.

This temperature margin is very important to withstand to the temperature ripple due to intermittent operations.

However, the results shown that in the considered worst case the peak-to-peak value of the temperature ripple is in around 15-20 °C, leading to a safety margin for the winding insulation of around 10 °C [XV].

Liquid cooling characterization with fans

For the sake of completeness, the steady-state thermal tests of the liquid cooling system have been repeated with the two fans mounted on the rotor sides. During these tests, the holes in the external frame where still closed with the plastic tape and, thanks to the rotor balancing, the maximum speed was 4500 rpm.

The obtained trends for the stator winding over-temperatures versus the rotor speed are reported in Fig. 6.2.8. Even if the frame holes are closed, it is possible to observe that there is a non-negligible drop of the winding average over-

temperature when the speed increases. This is due to a better forced convection heat exchange in the end winding region due to the movement of the internal air produced by the fans, confirming the findings already articulated by the authors in [69] for industrial induction motors.

The windage losses due to the fans shown in Fig. 6.2.1 will obviously impact on the efficiency of the BSG. So, if the target is to keep the internal air motion, the adoption of smaller fins on the end rings surface is suggested.

6.2.4. Conclusion

The challenging requirements for belt-driven starter-generator, both in terms of specific electromagnetic performance and the critical positioning of the electrical machine inside the engine compartment, mandatory need a careful analysis of the adopted cooling system. The problem has been approached with a full experimental methodology using a special BSG prototype equipped with both force air and liquid cooling systems.

Contrary to the conventional belt-driven alternators, the experimental findings prove that the forced air cooling system is not suitable for the application, and that the adoption of the more complicated liquid cooling system cannot be avoided for the designed BSG induction machine. Anyway, a dedicated liquid cooling circuit seems to be not necessary, and the engine coolant can directly cool the BSG prototype.

7. Conclusions

This manuscript presents the design and testing of an electrical machine for mild-hybrid powertrain applications; complete design aspects of a multiphase IM prototype respecting the system requirements has been presented and discussed.

Among the electrical machine topologies, IM is considered the best candidate for the application under consideration for its low cost, high overload capabilities, good flux-weakening characteristics and robust mechanical design.

For what it concerns the winding topology, the multi three-phase configuration with two independent three-phase sets represents a good solution in terms of current splitting and system complexity.

The details of the machine are presented with the focus on multilayer bar stator winding, pole count and on rotor slot design. In particular, it was found that multilayer bar conductor topology for the stator winding production is an interesting candidate for high-current and high-frequency applications, even in the case of small size machines. In addition, it was proved that the open rotor slot configuration is the viable solution for the fully achievement of the required performance in the whole speed range without compromising the mechanical robustness. Test results are presented, and it is shown a good agreement between predicted and measured data. The achievable performance, computed using the measured machine parameters, demonstrated the feasibility of the proposed design solution.

The thermal management of electrical machines operating with duty cycle is a critical issue because of variable torque and speed that means variable losses distribution with respect to speed and time. Based on these considerations, a simplified winding thermal model was presented. Furthermore, experimental investigation of cooling systems has been carried out in this thesis.

A first-order stator winding thermal model was developed for the temperature prediction during transient overload condition. The simplified thermal network is particularly suitable for the implementation in electrical drives for the on-line and real time prediction of the maximum over-current value when the transient duration is known, or vice versa. It is noteworthy to keep in mind that the proposed thermal model allows predicting an average temperature of the stator winding, neglecting the presence of hot spot.

The proposed first order model was experimentally validated in operative conditions and the results confirm the validity of the simplified thermal model for

the prediction of the winding temperature in short-time thermal transient, both for torque step response and intermittent services.

As it concerns the steady state heat extraction, the forced convection cooling systems were investigated by means of a fully experimental methodology using a special prototype equipped with both force air and liquid cooling systems. Contrary to the conventional belt-driven alternators, the experimental findings proved that the forced air cooling system is not suitable for the application, and that the adoption of the more complicated liquid cooling system cannot be avoided for the designed BSG induction machine. Anyway, a dedicated liquid cooling circuit seems not to be necessary, and the engine coolant can directly cool the BSG prototype.

On the bases of this research experience it is possible to outline the future prospects:

- Extended test campaign of the prototypes fed by inverter and development of control strategies
- Performance and thermal assessment under fault operations of multiphase machines
- Efficiency mapping during driving cycles
- Implementation of the thermal model on the control strategy

References

[1]. European Commission Regulation no. 443/2009.

[2]. European Commission Regulation no. 715/2007.

[3]. Cornetti, G., Millo F. : ”Macchine Termiche", Ed. Il Capitello, 2007.

[4]. B. Lequesne, “Automotive Electrification: The Non-Hybrid Story”, IEEE Trans. on Transp. Electr., Vol. 1, no. 1, pp. 40-53, June, 2015.

[5]. A. Emadi, “Transportation 2.0”, IEEE Power and Energy Magazine, pp.18-29, July/August, 2011.

[6]. C.C. Chan, "The state of the art of electric, hybrid, and fuel cell vehicles". Proc. of the IEEE, Vol. 95, No.4, pp. 704 - 718, April 2007.

[7]. http://www.toyota-global.com/innovation/environmental_technology /hybrid/

[8]. Ganji B., Kouzani A.Z., Trinh H.M.: “Drive cycle analysis of the performance of hybrid electric vehicles”, Life system modeling and intelligent computing, 2010, 434-444.

[9]. http://www.mazda.com/en/innovation/technology/env/i-eloop/.

[10]. http://www.buick.com/fuel-efficiency-without-sacrifice.html.

[11]. W. Cai, “Comparison and Review of Electric Machines for Integrated Starter Alternator Applications”, Conference rec. IAS Annual Meeting, 2004.

[12]. A. Bruyere, E. Semail, A. Bouscayrol, F. Locment, J. M. Dubus, J. C. Mipo, “Modeling and Control of a Seven-phase Claw-Pole Integrated Starter Alternator for Micro-Hybrid Automotive Applications”, in IEEE Vehicle Power and Propulsion Conference, pp. 1-6, 2008.

[13]. M. Sattler, T. Smetana, T. Meyerhofer, L. Kuhlkamp, “48V Minihybrid - A New Solution for the Minimale Hybridization of Vehicles”, in 22nd Aachen Colloquium Automobile and Engine Technology 2013, pp. 995-1008, 2013.

[14]. Y. Burkhardt, A. Spagnolo, P. Lucas, M. Zavesky, P. Brockerhoff, “Design and analysis of a highly integrated 9-phase drivetrain for EV applications”, International Conference on Electrical Machine, pp. 450-456, 2014.

[15]. R. Henry, B. Lequesne, S. Chen, J. Ronning, "Belt-Driven Starter-Generator for Future 42-Volt Systems", SAE 2001 World Congress, SAE Technical Paper, 2001.

[16]. W. Hackmann, B. Klein, C. Gotte, R. Schmid, F. X. Pujol, “48V – The Way to a High Volume Electrification”, in 22nd Aachen Colloquium Automobile and Engine Technology 2013, pp. 1009-1030, 2013.
[17]. S. Jurkovic, K. M. Rahman, J. C. Morgante, P. J. Savagian, " Induction Machine Design and Analysis for General Motors e-Assist Electrification Technology," IEEE Trans. Ind. Applicat., Vol. 51, pp. 631-639, 2015.
[18]. S. Chen, B. Lequesne, R. R. Henry, Y. Xue, J. J. Ronning, “Design and Testing of a Belt Driven Induction Starter Generator”, IEEE IEMDC’01, pp. 252-260, 2001.
[19]. http://media.gm.com/.
[20]. J. G. Kassakian; H. -C. Wolf; J. M. Miller; C. J. Hurton, “Automotive electrical systems circa 2005”, IEEE Spectrum, 1996.
[21]. J. G. Kassakian; D. J. Perreault, “The future of electronics in automobiles”, Conference Proceedings on Power Semiconductor Devices and ICs, 2001.
[22]. NDE_VW82148-1_LV148.pdf LV 148 here: internal VW standard.
[23]. J. Walters, R. Krefta, G. Gallegos-Lopez, G. Fattic, "Technology Considerations for Belt Alternator Starter Systems", SAE World Congress, SAE Technical Paper 2004-01-0566, 2004.
[24]. P. Zhang, S. S. Williamson, “Recent Status and Future Prospects of Integrated Starter-Generator Based Hybrid Electric Vehicles”, IEEE Vehicle Power and Propulsion Conference, pp. 1-8, 2008.
[25]. D. Richard, Y. Dubel, “Valeo StARS Technology: A Competitive Solution for Hybridization”, Conf. Proc. Power Conversion Conference, pp. 1601-1605, 2007.
[26]. K. Kamiev, J. Montonen, M. P. Ragavendra, J. Pyronen, J. A. Tapia, M. Niemela, “Design Principles of Permanent Magnet Synchronous Machine for Parallel Hybrid or Traction Application”, IEEE Trans. Ind. Electron., vol. 60, n. 11, pp. 4881-4890, 2013.
[27]. G. Pellegrino, A. Vagati, B. Boazzo, P. Guglielmi, “Comparison of Induction and PM Synchronous Motor Drives for EV Application Including Design Examples”, IEEE Trans, Ind. Appl. Vol. 48, no. 6, pp. 2322-2332, November/December, 2012.
[28]. S. Scridon, I. Boldea, L. Tutelea, F. Blaabjerg, A. E. Ritchie, “BEGA—A Biaxial Excitation Generator for Automobiles: Comprehensive Characterization and Test Results”, IEEE Trans. on Ind. Appl. Vol. 41, no. 4, pp.935-944 2005.

[29]. L. Alberti, M. Barcaro, M. Dai Pré, A. Faggion, L. Sgarbossa, N. Bianchi, S. Bolognani, “IPM Machine Drive Design and Tests for an Integrated Starter–Alternator Application”, IEEE Trans. on Ind. Appl. Vol. 46 No. 3, pp.993-1001, 2010.

[30]. R. F. Wall, H. L. Hess, “Induction machines as an alternative for automotive electrical generation and starting systems”, Conf. Proc. International conference in Electric Machine and Drives, pp. 499-501, 1999.

[31]. S. Chen, B. Lequesne, R. R. Henry, Y. Xue, J. J. Ronning, “Design and testing of a belt-driven induction starter-generator”, IEEE Trans. Ind. Appl., Vol 36 np. 6, pp. 1525-1533, 2002.

[32]. S. Jurkovic; K. M. Rahman; J. C. Morgante; P. J. Savagian, “Induction Machine Design and Analysis for General Motors e-Assist Electrification Technology”, IEEE Trans. Ind. Appl., Vol 51, no. 1, pp. 631-639, 2015.

[33]. A. Boglietti, A. Cavagnino, L. Ferraris, M. Lazzari, “Energetic Considerations about the Use of Cast Copper Squirrel Cage Induction Motor”, Conf. Proc. IECON 2007, pp. 157-162. 2007.

[34]. http://www.porsche.com/usa/models/panamera/panamera-s-e-hybrid/drive/technology/

[35]. R. Bojoi, S. Rubino, A. Tenconi, S. Vaschetto, “Multiphase electrical machines and drives: A viable solution for energy generation and transportation electrification”, International Conference and Exposition on electrical and Power Engineering, pp.632-369, 2016.

[36]. E. Levi, “Multiphase Electric Machine for Variable Speed Applications”, IEEE Trans. On Ind. Appl., Vol. 55no. 5, 2008.

[37]. E. Levi, R. Bojoi, F. Profumo, H.A. Toliyat, S. Williamson, “Multiphase induction motor drive – a technology status review”, IET Electr. Power Appl. Vol.1, no. 4, pp.489-516, 2007.

[38]. R. Bojoi, A. Cavagnino, A. Tenconi, A. Tessarolo, S. Vaschetto, “Multiphase Electrical Machine and Drives in the Transportation Electrification”, IEEE RTSI, pp. 205-212. 2015.

[39]. E. E. Ward and H. Härer, “Preliminary investigation of an inverter-fed 5-phase induction motor,” Proc. Inst. Electr. Eng., vol. 116, no. 6, pp. 980–984, Jun. 1969.

[40]. J.S. Tongam, M. Tarbouchi, A.F. Okou, D. Bouchard, R. Beguenane, “Trends in Naval Ship Propulsion Drive Motor technology”, IEEE EPEC, 2013.

[41]. S. Manter, E. De Paola, G. Marina, "An Optimized Control Strategy for double star motors configuration in redundancy operation mode", EPE 99, 1999.
[42]. A. Boglietti, A. Cavagnino, A. Tenconi, S. Vaschetto, "The Safety Electric Machine and Drives in the more Electric Aircraft: a survey", IEEE IECON, 2009.
[43]. P. Wheeler, S. Bozhko, "The More Electric Aircraft – Technology and Challenges", IEEE Electrification Magazine, vol. 2, no. 4, pp. 6-12, 2014.
[44]. M. G. Simoes, P. Vieira, "A–High Torque Low Speed Multiphase Brushless Machine a Perspective Application for Electric Vehicles", IEEE Trans. Ind. Electron, Vol. 49. no. 5, pp.1154-1164, 2002.
[45]. N. Bianchi, M. Dai Prè, S. Bolognani, "Design of Fault-Tolerant IPM Motor for Electric Power Steering", IEEE Trans. Vehicular Tech., Vol. 55. No. 4, 2006.
[46]. A. Boglietti, A. Cavagnino, M. Lazzari, S. Vaschetto, "Preliminary induction motor electromagnetic sizing based on a geometrical approach", IET Electric Power Applications, Vol.6, no.9, pp.583-592, 2012.
[47]. I. Boldea, S.A. Nasar, 'The induction machines design handbook, second edition', CRC Press, 2009.
[48]. A. Boglietti, A. Cavagnino, M. Lazzari, "Computational Algorithms for Induction-Motor Equivalent Circuit Parameter Determination - Part I: Resistance and Leakage Reactances", IEEE Trans. Ind. Electron., vol. 58, n. 9, pp. 3723-3733, 2011.
[49]. A. Boglietti, A. Cavagnino, M. Lazzari, "Computational Algorithms for Induction Motor Equivalent Circuit Parameter Determination - Part II: Skin Effect and Magnetizing Characteristics", IEEE Trans. Ind. Electron., vol. 58, n. 9, pp. 3734-3740, 2011.
[50]. S. Sprague, "Lamination Steels Third edition CD-ROM", EMERF.
[51]. F. Liang, D. Novotny, R. W. Fei, X. Xu, "Selection of the Pole Number of Induction Machine for Variable Speed Applications, IEEE Trans. Ind. Applicat, Vol. 31, n. 2, pp. 304-309, March/April, 1995.
[52]. E. Agamloh, A. Cavagnino, S. Vaschetto, "Impact of Number of Poles on the Steady-State Performance of Induction Motors", IEEE Trans. Ind. Applicat. Early Access, 2015.
[53]. A. Boglietti, R. Bojoi, A. Cavagnino, P. Guglielmi, A. Miotto, "Analysis and Modelling of Rotor Slot Enclosure Effects in High-Speed Induction Motors", IEEE Trans. Ind. Applicat., vol. 48, n. 4, pp. 1279-1287, 2012.

[54]. W. Zhang, T. M. Jahns, "Analytical 2-D Slot Model for Predicting AC Losses in Bar-Wound Machine Windings due to Armature Reaction", IEEE Transportation Electrification conference and EXPO (ITEC), pp. 1-6, 2014.

[55]. A. Boglietti, A. Cavagnino, M. Lazzari, "Computational Algorithms for Induction Motor Equivalent Circuit Parameter Determination – Part I: Resistances and Leakage Reactance", IEEE Trans. Ind. Elect. Vol 58. No.9, pp. 3723-3733, September 2011.

[56]. A. Boglietti, A. Cavagnino, M. Lazzari, "Computational Algorithms for Induction Motor Equivalent Circuit Parameter Determination – Part II: Skin Effect and Magnetizing Characteristics", IEEE Trans. Ind. Elect. Vol 58. No.9, pp. 3734-3740, September 2011.

[57]. H. Hamalainen, J. Pyronen, and J. Nerg, "AC resistance factor in one-layer form-wound winding used in rotating electrical machines," IEEE Trans. Magn., vol. 42, no. 6, pp. 1–8, Jun. 2013.

[58]. Test Procedure for Polyphase Induction Motors and Generators, IEEE Std. 112-2004, Nov. 2004.

[59]. A. Boglietti, A. Cavagnino, L. Ferraris, and M. Lazzari, "Skin effect experimental validations of induction motor squirrel cage parameters," Int. J. Comput. Math. Electr. Electron. Eng., vol. 29, no. 5, pp.1257–1265, 2010.

[60]. P. Mellor, D. Roberts, and D. Turner, "Lumped parameter thermal model for electrical machines of TEFC design," IEE Elect. Power Appl., vol. 138, no. 5, pp. 205–218, 1991.

[61]. A. Boglietti, A. Cavagnino, M. Lazzari, and M. Pastorelli, "A simplified thermal model for variable-speed self-cooled industrial induction motor," IEEE Trans. Ind. Appl., vol. 39, no. 4, pp. 945–952, Jul./Aug. 2003.

[62]. C. Kral, A. Haumer, and T. Bauml, "Thermal model and behavior of a totally-enclosed-water-cooled squirrel-cage induction machine for traction applications," IEEE Trans. Ind. Electron., vol. 55, no. 10, pp. 3555–3564, Oct. 2008.

[63]. Motor Design Ltd. Motor-CAD Thermal, Ellesmere, U.K. [Online]. Available: http://www.motor-design.com.

[64]. A. Boglietti, A. Cavagnino, D. Staton, M. Shanel, M. Mueller, and C. Mejuto, "Evolution and modern approaches for thermal analysis of electrical machines," IEEE Trans. Ind. Electron., vol. 56, no. 3, pp. 871–882, Mar. 2009.

[65]. M. Tosetti, P. Maggiore, A. Cavagnino, and S. Vaschetto, “Conjugate heat transfer analysis of integrated brushless generators for more electric engines,” IEEE Trans. Ind. Appl., vol. 50, no. 4 pp. 2467–2475, Jul./Aug. 2014.

[66]. J. L. Baker, R. Wrobel, D. Drury, and P. H. Mellor, “A methodology for predicting the thermal behaviour of modular-wound electrical machines,” in Proc. IEEE Energy Convers. Congr. Expo. (ECCE), 2014, pp. 5176–5183.

[67]. A. Boglietti, A. Cavagnino, and D. Staton, “Determination of critical parameters in electrical machine thermal models,” IEEE Trans Ind. Appl., vol. 44, no. 4, pp. 1150–1159, Jul./Aug. 2008.

[68]. D. Staton, A. Boglietti, and A. Cavagnino, “Solving the more difficult aspects of electric motor thermal analysis,” IEEE Trans. Energy Convers., vol. 20, no. 3, pp. 620–628, Sep. 2005.

[69]. A. Boglietti, A. Cavagnino, D. Staton, M. Popescu, C. Cossar, and M. McGilp, “End space heat transfer coefficient determination for different induction motor enclosure types,” IEEE Trans. Ind. Appl., vol. 45, no. 3, pp. 929–937, May/Jun. 2009.

[70]. N. Jaljal, J. F. Trigeol, and P. Lagonotte, “Reduced thermal model of an induction machine for real-time thermal monitoring,” IEEE Trans. Ind. Electron., vol. 55, no. 10, pp. 3535–3542, Oct. 2008.

[71]. E. Foulon, C. Forgez, and L. Loron, “Resistance estimation with an extended Kalman filter in the objective of real-time thermal monitoring of the induction machine,” IET Elect. Power Appl., vol. 1, no. 4, pp. 549–556, 2007.

[72]. P. Zhang, B. Lu, and T. G. Habetler, “An active stator temperature estimation technique for thermal protection of inverter-fed induction motors with considerations of impaired cooling detection,” IEEE Trans. Ind. Appl., vol. 46, no. 5, pp. 1873–1881, Sep./Oct. 2010.

[73]. G. D. Demetriades, H. Zelaya de la Parra, E. Andersson, and H. Olsson, “A real-time thermal model of a permanent-magnet synchronous motor,” IEEE Trans. Power Electron., vol. 25, no. 2, pp. 463–474, Feb. 2010.

[74]. C. Kral, A. Haumer, and S. B. Lee, “A practical thermal model for the estimation of permanent magnet and stator winding temperatures,” IEEE Trans. Power Electron., vol. 29, no. 1, pp. 455–464, Jan. 2014.

[75]. Y. Bertin, E. Videcoq, S. Thieblin, and D. Petit, “Thermal behavior of an electrical motor through a reduced model,” IEEE Trans. Energy Convers., vol. 15, no. 2, pp. 129–134, Jun. 2000.

[76]. Z. Gao, T. G. Hebetler, and R. G. Harley, “An online adaptive stator winding temperature estimator based on a hybrid thermal model for induction machines,” in Proc. IEEE Int. Conf. Elect. Mach. Drives (IEMDC), 2005, pp. 754–761.

[77]. Z. Gao, R. S. Colby, T. G. Hebetler, and R. G. Harley, “A model reduction perspective on thermal models for induction machine overload relays,” IEEE Trans. Ind. Electron., vol. 55, no. 10, pp. 3525–3534, Oct. 2008.

[78]. C. Kral, A. Haumer, and S. B. Lee, “Robust thermal model for the estimation of rotor cage and stator winding temperatures of induction machines,” in Proc. Int. Conf. Elect. Mach. (ICEM’12), Marseille, France, Sep. 2–5, 2012, pp. 1810–1816.

[79]. V. T. Buyukdegirmenci and P. T. Krein, “Induction machine characterization for short-term or momentary stall torque,” IEEE Trans. Ind. Appl., vol. 51, no. 3, pp. 2237–2245, May/Jun. 2015.

[80]. C. Paar, A. Muetze, H. Kolbe, “Influence of Machine Integration on the Thermal Behavior of a PM Drive for Hybrid Electric Traction”, IEEE Trans. on Ind. Appl., Early access 2015.

[81]. L. Fedoseyev and E.M. Pearce Jr.“Rotor assembly with heat pipe cooling system”, US patent application # 2014/0368064 A1.

[82]. J. C. H. Bone, “Cooling and cooling circuits for electric motors”, IEEE Trans. Electr. Power Appl., Vol. 1, no. 2, May, 1978.

[83]. W. Kim, W.H. Jeon, N. Hur, J.J. Hyun, C.K.Lim, S.H. Lee, “Development of a Low-noise Cooling Fan for an Alternator Using Numerical and DOE Methods”, International Journal of Automotive Technology, Vol. 12, no. 2, pp. 307-314, 2011.

[84]. Cedrat, Design Solutions for Electrical Engineering. Portunus Multiphysics System Simulator, Meylan, France [Online]. Available: http://www.cedrat.com/en/software/portunus.html.

[85]. D. Caruso, G. Scelba, N. Bianchi, L. Alberti, G. Scarcella, “Parameters Identification of Multi-Windings Induction Machines”, International Conference on Electrical Machine (ICEM), pp. 519-525, Lausanne, 2016.

[86]. A. Cavagnino, A. Tenconi, G. Rizzoli, M. Mengoni, G. Serra, “Multiphase Induction Machine for Aero-Engine Shaft-Line Embedded Starter/Generator: Scaled Prototypes Testing” International Conference on Electrical Machine (ICEM), pp. 2107-2113, Berlin, 2014.

[87]. H. Seng Che, A. Abdel-Khalik, O. Dordevic, E. Levi, “Parameter Estimation of Asymmetrical Six-phase Induction Machine using Modified Standard Test” IEEE Trans. Ind. Electr., 2017 Early Access.